論文 / 著書情報
Article / Book Information

題目(和文)	
Title(English)	Study of Amorphous Silicon Based Thin-Film Solar Cells with Full Spectrum Splitting Technique
著者(和文)	KimSinae
Author(English)	Sinae Kim
出典(和文)	学位:博士(工学), 学位授与機関:東京工業大学, 報告番号:甲第9650号, 授与年月日:2014年9月25日, 学位の種別:課程博士, 審査員:小長井　誠,半那　純一,筒井　一生,山田　明,渡辺　正裕 ,Koeng Su Lim
Citation(English)	Degree:Doctor (Engineering), Conferring organization: Tokyo Institute of Technology, Report number:甲第9650号, Conferred date:2014/9/25, Degree Type:Course doctor, Examiner:,,,,,
学位種別(和文)	博士論文
Type(English)	Doctoral Thesis

Chapter 1

Over View and Objective of This Research

1-1 Overview

Mankind needs energy for a living. Besides the energy in our food necessary to sustain our body and its function, 30 times more energy is used on average to make our life more comfortable.

This thesis describes the results of research on the numerical analysis and the elemental technology for amorphous silicon based solar cells and full spectrum splitting technique. In this chapter, motivations of the research are mainly presented. Here, after a brief discussion on needs of sustainable energy, the solar energy and the photovoltaic (PV) technology as a candidate for the sustainable energy are discussed. Subsequently, the thin-film silicon, i.e., hydrogenated amorphous silicon (a-Si:H), as a low-cost material for photovoltaic applications, is briefly described. Finally, the objective of this study and the outline of the rest of this thesis are given.

1-1-1 Renewable Energy Source- Solar Cells

The world energy demand is growing explosively. In the year 2000, the total energy consumption on earth was around 400 EJ[1-3]. In the year 2050, the total world energy consumption is estimated to be around 1200 EJ, three times the consumption in the year 2000 [1,2]. A still growing world population, 6 billion people in 2000 and approximately 9 billion people in the year 2050 [4], as well as rapid economic growth in countries like China and India are mainly responsible for this increase in energy demand. At the same time, the amount of fossil fuels on earth is limited. Extrapolating our actual energy consumption and only regarding already known resources, our oil reserves are sufficient for approximately the next 40 years, our natural gas reserves for the next 60 years and our coal reserves for the next 225 years [2,5]. In the year 2003, 7.4% of the world energy consumption was based on coal, 42.6% on oil and 16.4% on natural gas in Fig.1 [6]. This clearly indicates that the upcoming problems regarding energy supply are enormous. Regarding the diminishing amount of available fossil fuels, our actual dependence on them and the growing world energy demand, there will be an increasing amount of energy that has to be generated by new resources as biomass, nuclear, wind and solar energy. Problematic is not only the energy demand, but also the environmental damage produced by fossil fuels. Amongst other forms of environmental damage, fossil fuels produce greenhouse gases, such as CO_2. Other greenhouse gases are methane (CH_4), nitrous oxide (N_2O), hydrofluorocarbons (HFCs), perfluorocarbons (PFCs) and sulphur hexafluoride (SF_6) [7]. Greenhouse gases are generally seen as the main cause for global warming Fig.2. A shift from using fossil fuels to renewable forms of energy, and also to nuclear energy, can play a huge role in controlling global warming. Worldwide, solar energy is probably the most promising form of renewable energy. There are several forms of use of solar energy, i.e. where solar irradiation is directly or indirectly converted into electricity. The most direct form of solar energy conversion is so called photovoltaic (PV) energy. The incoming radiation from sunlight is directly converted into DC electricity using the photovoltaic effect. With this technology, commercial conversion efficiencies of typically 10-15% can be obtained. These efficiencies are expected to increase to more than 20% in the future [3]. Other forms of solar energy conversion are for instance heat production through solar collectors and electricity production by so called concentrated solar thermal plants that employ parabolic mirrors or other concentration techniques. In this thesis however, only PV will be taken into consideration. Photovoltaic solar energy conversion is a very direct, elegant and clean way of producing energy. Sunlight is directly converted into energy and the environmental impact and risks are reduced to a minimum. The amount of energy that enters the earth per year in the form of incident sunlight is more than ten thousand times the actual annual energy consumption and more than a hundred thousand times the yearly electricity consumption on earth [8]. Assuming an average module efficiency of 10%, an area of 800 x 800 km_2 in the Sahara desert covered with solar cells would be sufficient to produce the amount of yearly consumed energy in the year 2000 [9]. An area of about 1400 x 1400 km2 would be enough to cover the world energy demand in the year 2050. The costs of photovoltaic solar energy are substantially higher than the costs of energy from fossil fuels nowadays, but this is about to change. The costs of fossil fuels will keep on rising, albeit slowly, due to an increasing demand and a decreasing supply. Solar energy technology will keep on improving, so the prices of solar energy will go down fast. Worldwide, the price per unit of energy for solar cells is expected to be compatible with market prices for other energy technologies between 2020 and 2030 [9,10]. Large-scale PV plants, or many decentralized PV plants installed in the built environment will allow for a substantial amount of generated electricity in Fig.2. In other applications, such as small devices as watches and calculators, PV cells are especially useful; also for applications in remote areas because there is a direct conversion from sunlight into electricity and no long distance transport is needed [8]. For applications employing a very high energy density, for instance cars or planes, solar energy is not powerful enough and other types of energy need to be found and improved to compensate for our future lack of fossil fuels. However, we can say that there is a strong need for new energy technologies and solar energy is one of the most promising ones for the future.

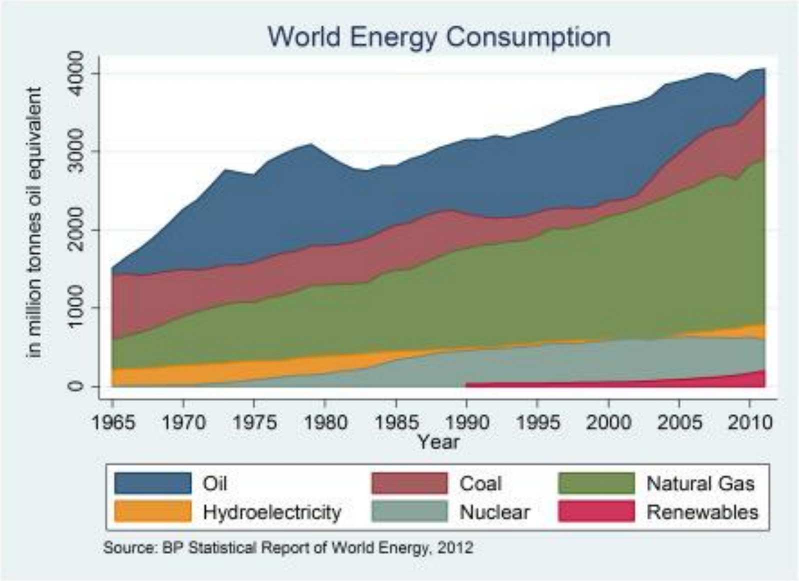

Source: BP Statistical Report of World Energy, 2012

Figure 1.1 World energy consumption divided by energy sources from 1965 to 2010[11]

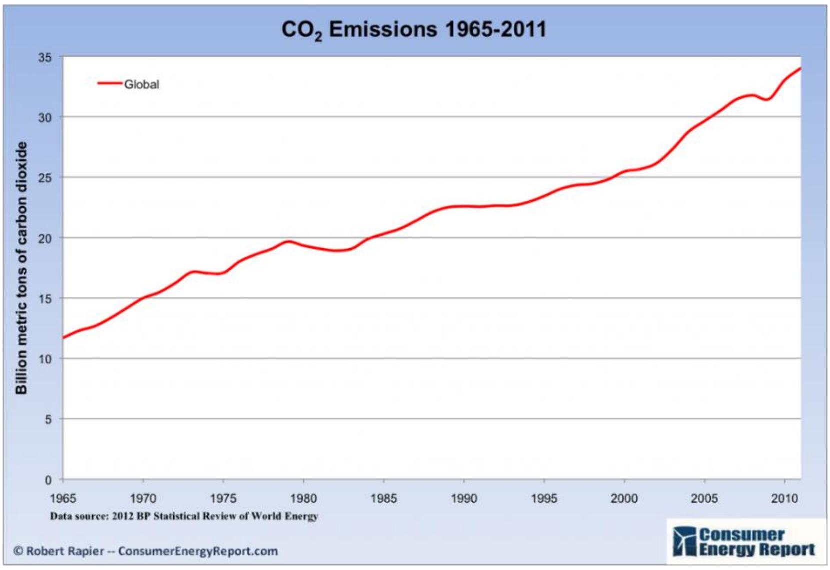

Data source: 2012 BP Statistical Review of World Energy

© Robert Rapier -- ConsumerEnergyReport.com

Figure1.2 Global Carbon Dioxide emission in atmosphere from 1965 to 2010[12]

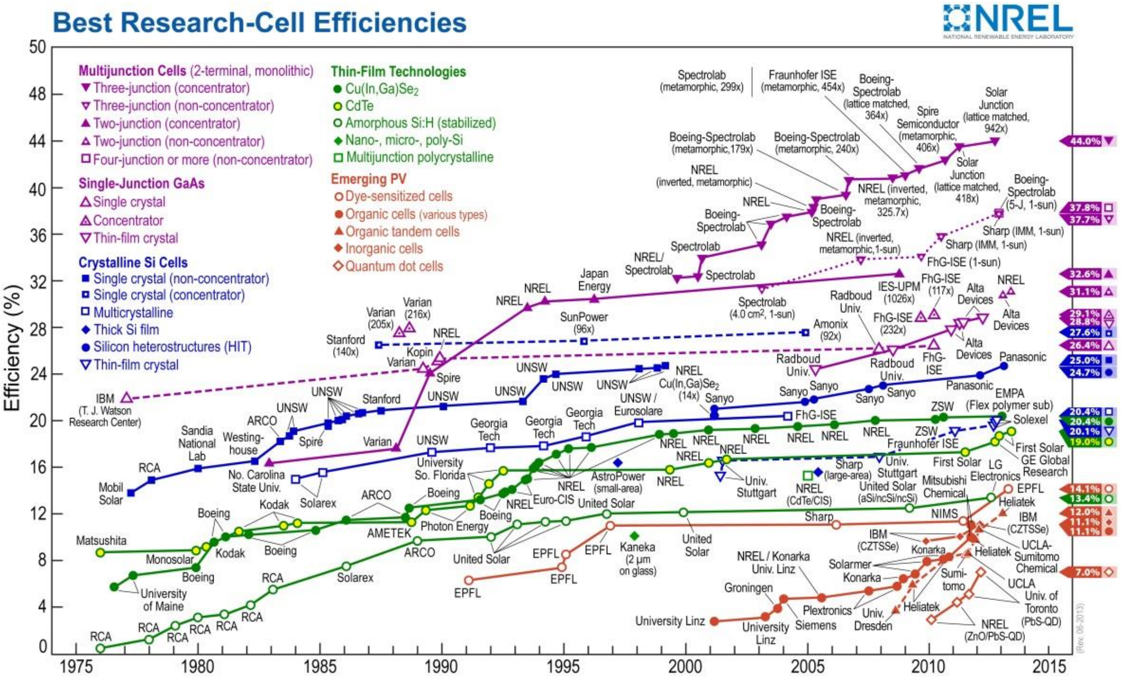

Figure 1.3 World record efficiencies of various PV technologies (Source: NREL)

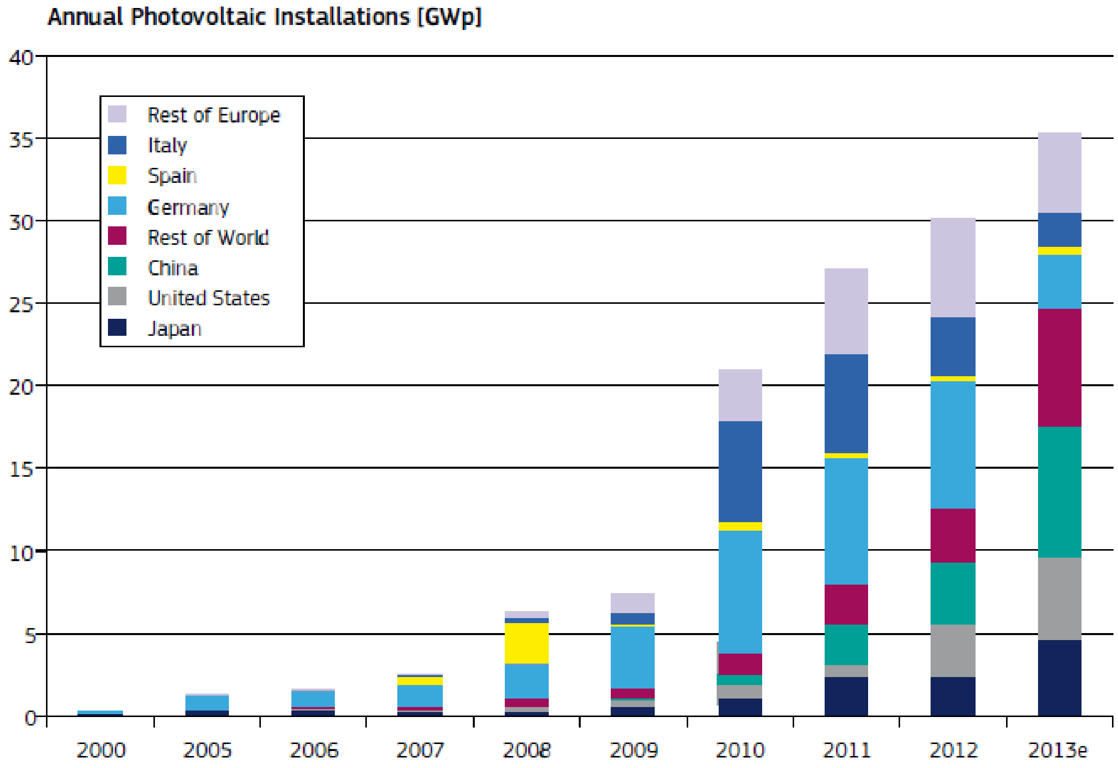

Figure 1.4 Annual PV installations from 2000 and 2013 ([*Epi* 2013, *NEA* 2013, *Sys* 2013])

1-1-2 Current Challenges

While crystalline and polycrystalline silicon solar cells dominate today's solar cell industry, the rapid rise in efficiency of the multi-junction thin-film cells makes this a particularly attractive technology path. Under concentrated sunlight, three multi-junction solar cells have demonstrated to achieve efficiencies 44% which twice higher than that of most silicon cells, which achieved at efficiency of 27.6%. This means that, in photovoltaic areas, a multi-junction concentrator system can generate electricity almost twice as much as a silicon panel with the same cell area. The concentrator solar cells focus the light onto a small area of cells, reducing the area of the solar cells by a factor of, typically, 500-1000 times. The reduced cell area overcomes the increased cell cost. The cell cost is diminished in importance and is replaced by the cost of optics. If the cost of the optics is comparable to the cost of the glass and support structure needed for silicon flat-plate modules, then the cost per unit area can remain fixed while the electricity production is essentially doubled. Thus, in high direct insolation locations, multi-junction concentrator technology has the potential to reduce the cost of solar electricity by about a factor of two. The efficiency is a moving target; today's triple-junction cell efficiency is over 40%. Thus it may be reasonably extrapolated that multi-junction cells may reach 50% efficiency in the future. The use of solar cell is increasing dramatically, but in the context of the global energy consumption solar cell only account for an insignificant part of the amount of energy that is produced (~0.036%). Most of the established solar cell technologies are stable and exhibit a relatively high power-conversion efficiency in the range of 10-20%, qualifying for electrical energy production for on-grid or local use provided that the land mass is available. However, they all suffer from a very high cost, giving energy prices of a few yen per watt in 2013 terms. This is believed to be one of the reasons that the use is mainly limited to niche products and applications at remote locations. The general view is that solar cell technology has to fulfill three criteria to reach large market and provide on-grid electricity production [13, 14]. The solar cell technology has to be stable, efficient, and of low cost. Crystalline silicon solar cells are very stable, with estimated operational lifetimes in excess of 25 years and module power conversion efficiencies as high as 20%. The cost, however, is too high and this is seen as the main reason for the scarcity of solar cell technologies on the energy scene. Thin film solar cells are holding some promise in this respect because it is a technology that in many ways is complementary such as low cost, low thermal budget, solution processing and very fast methods for fabrication. Seen in light of the recent advances within the field of thin film solar cell with respect to stability and power-conversion efficiency, the current challenge is the industrial demonstration of a low cost module with moderates stability and efficiency. The secondary challenges are a higher stability of more than 10 years and efficiencies above 40%. Most notably, the demonstrations of moderate efficiency, high stability, and large-scale processing have not been demonstrated for the same materials and the technology used so far. However, the fact that isolated studies can reach any of the three goals does hold promise for the possibility of combining all three goals in the material and this is the overall current challenge known as the unification challenges as illustrated in Fig.1.5.

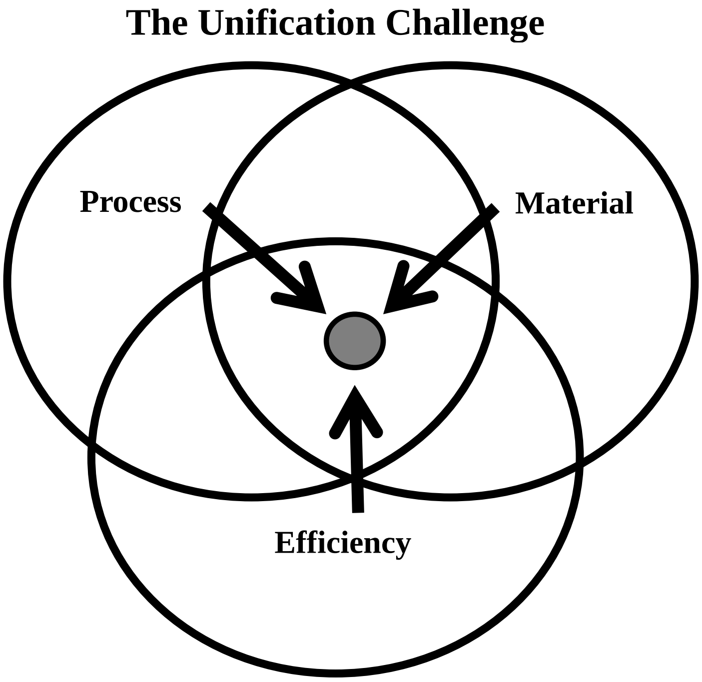

Figure 1.5 The Unification challenge of combining efficiency, material, and large scale processing for advanced solar cell technology. The properties have been demonstrated individually and the combination of some stability and some efficiency has been achieved with some development.

1-2 Objective of This Research

Since the solar spectrum is broad, containing photons with energies in the range of about 0 to 4 eV, single-junction solar cell efficiencies are thus inherently limited to significantly less than the efficiency with which monochromatic light can be converted. The solution to this problem is (in principle) simple: rather than trying to convert all the photon energies with one cell with one band gap, divide the spectrum into several spectral regions and convert each with a cell whose band gap is tuned for that region. The greater the number of spectral regions allowed, the higher the potential overall efficiency. The main purpose of this dissertation is to develop a a-Si:H based thin film solar cell for Full spectrum splitting method, which is able to achieve high conversion efficiency solar cell at broad spectrum range. This spectrum splitting method has re-considered and developed for thin film based solar cells. So here, two types of thin film based solar cells have used in this thesis amorphous and Ⅲ-Ⅴ based solar cells because it has own advantage at certain range of wavelength.

Mainly, for top cell application which is a-Si:H solar cell has studied with low substrate temperature , high hydrogen dilution and new transparent conductive oxide substrate. More detail of this thesis will be introduced right after this section.

1-3 Outline of this thesis

The structure of this thesis is summarized as shown in Figure 1.6. From the schematic diagram, the thesis consists of eight chapters. A brief description of each chapter is described as the following.

Chapter 1: General overview and introduction of global trends of solar cell and current challenge of solar cell technology. Also the motivation of this study is described. Then the objective of this thesis is proposed.

Chapter 2: The fundamental property of amorphous silicon-based materials in terms of its structure, electrical, optical properties. The introduction of amorphous silicon-based solar cells is explained with single junction as well.

Chapter 3: The numerical analysis of thin film solar cells which are amorphous based solar cell and CIGS solar cell with different of absorber thickness and optical band gap. Then under the each certain of spectrum, those two thin film solar cells are demonstrated for finding perfect match of condition. This simulation was performed by simulator called AMPS-1D (Analysis of Microelectronic and Photonic Structures) in order to explore the preferred solar cells' properties corresponding to application purposes are explained. Additionally, the investigation of effect of these solar cell detailed parameter on the performance of silicon-based thin film solar cells and compound CIGS solar cell as well.

Chapter 4: The characterization and optimization of amorphous based silicon solar cell by using very-high - frequency plasma-enhanced chemical vapor deposition (VHF-PECVD) technique for application into amorphous silicon-based thin film solar cells are presented. The fabrication of the novel a-Si:H single-junction solar cells applying low substrate temperature and high hydrogen dilution regime for application of spectrum splitting top cell.

Chapter 5: The fabrication of the optimized a-Si:H solar cells and CIGS solar cell mused by spectrum splitting technique. As follow the simulation result, first we use conventional optical filter to find best spectrum splitting wavelength. Five different splitting wavelength has been prepared (600, 650, 700, 750, and 800nm) then we find best spectrum splitting results at splitting wavelength 614nm exactly same splitting wavelength from our simulation result, then the optical filter has been optimized in order to has best performance under the spectrum splitting configuration. Using this optimized optical filter when the splitting wavelength 614nm, both of solar cell measured. Then we got almost 23% of solar cell efficiency

Chapter 6: the results obtained from this thesis are summarized. Even more, suggestions for further improvement are also offered.

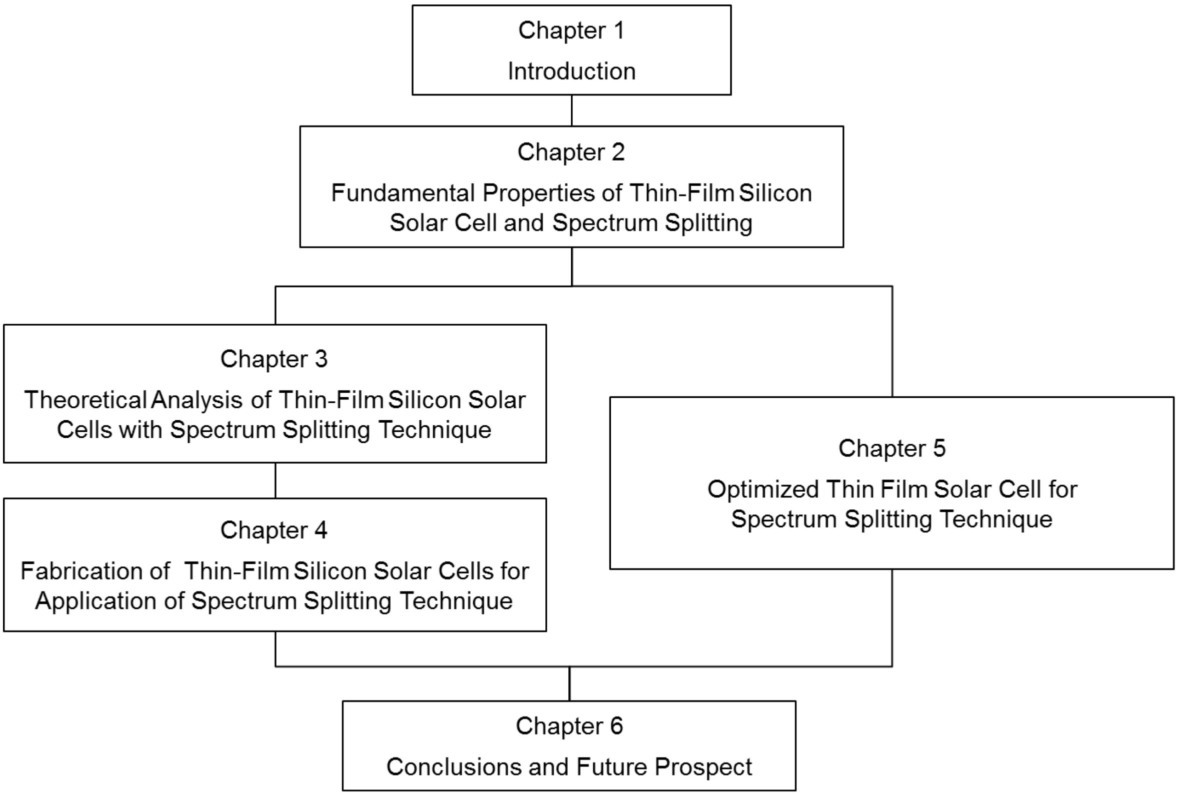
Chapter 1
Introduction
Chapter 2
Fundamental Properties of Thin-Film Silicon Solar Cell and Spectrum Splitting
Chapter 3
Theoretical Analysis of Thin-Film Silicon Solar Cells with Spectrum Splitting Technique
Chapter 4
Fabrication of Thin-Film Silicon Solar Cells for Application of Spectrum Splitting Technique
Chapter 5
Optimized Thin Film Solar Cell for Spectrum Splitting Technique
Chapter 6
Conclusions and Future Prospect

REFERENCES

[1] German Advisory Council on Global Change (WBGU), World in Transition – Towards Sustainable Energy Systems (2004)

[2] R.E.I. Schropp, Introduction to Solar Cell Research – College MEF, Universiteit Utrecht (2005)

[3] K. Blok, Introduction to Energy Analysis, Purdue University Press (2007)

[4] United Nations Population Information Network (POPIN), World Population Prospects: The 2004 Revision Population Database (2004)

[5] H.H. Rogner, An Assessment of World Hydrocarbon Resources, Annual Review of Energy and Environment, 22 (1997) 217-262

[6] International Energy Agency, Key World Energy Statistics (2005)

[7] UNFCCC, Caring for Climate, A guide to the Climate Change Convention at the Kyoto Protocol (2003)

[8] R.H.J. Franken, Ph.D. Thesis, Universiteit Utrecht (2006)

[9] W.C. Sinke, Presentation at the 'Chemische Kring Groningen' (16 March 2006)

[10] W. Hoffmann, PV Solar Electricity Industry: Market Growth and Perspective, Solar Energy Materials and Solar Cells, **90** (2006) 3285-3311

[11] BP Statistical Review of World Energy report 2013: http://www.bp.com/en/global/corporate/about-bp/statistical-review-of-world-energy-2013.html.

[12] PB Statistical Review of World Energy report 2012: http://www.energytrendsinsider.com/2012/07/02/global-carbon-dioxide-emissions-facts-and-figures/

[13] Brabec, C.J., “Photovoltaic:Technology and market,” *Sol. Energy Mater. Sol. Cells*,83,pp. 273-292 (2004)

[14] Krebs, F.C., “Alternative PV,” *Refocus,* 6, pp.38-39 (2005)

Chapter 2

Fundamental Aspect of a-Si:H Material and a-Si:H Based Thin Film Solar Cell

2. 1 Fundamental Characteristics of Amorphous Silicon Material

Amorphous solids refer to materials at a higher level of disorder, implying that it is by no means easy to describe the degree of structural regularity. That is, amorphous solids do not have a periodic, regular and repetitive structure and they cannot be defined by diatomic unit cells with a lattice constant while only localized short-range order is adequately maintained. These amorphous solids can processes various states thermodynamically and structurally at fixed temperatures and pressures, while crystalline materials has fundamental and uniquely well-defined structure at given set of temperatures and pressures.

2-1-1 Semiconductors

Solids can be divided into three different types, insulators, conductors and semiconductors. Solar cells are built up of semiconductors. To get an understanding of semiconductors, it is necessary to study the main properties of solids. Let us start by considering a single electron interacting with a positively charged atomic nucleus. We know that the interaction can be described by a Coulomb potential and that the electron can only occupy distinct energy levels [1]. The energy of the electron, compared to a reference taken as E=0 where the electron is ‘just unbonded’, is given by [2]:

$$E_n = -\frac{m}{2h^2}\left(\frac{-Ze^2}{2\varepsilon_0}\right)^2 \frac{1}{n^2}\,, \qquad n \in \mathbb{N} \setminus \{0\} \qquad (2.1)$$

In this equation, E_n is the nth discrete energy level, m the free electron mass, Z the number of protons in the atomic core, e the elementary charge, h Planck's constant and ε_0 stands for the permittivity of free space. The energy level for which $n=1$ is called the ground level. When more electrons are in the same atom, at most two electrons (with opposite spin) can be in the same energy level due to Pauli's exclusion principle. At very low temperatures ($T \approx 0K$), the electrons fill up the energy levels until the so-called *Fermi level* (E_F). Thus, the Fermi level is the highest occupied level for temperatures close to the absolute zero point. As already discussed, for systems containing only one atomic nucleus we have discrete sharply defined energy levels. In a crystal however, where more nuclei and electrons are present, the energy levels of all electrons shift somewhat due to the surrounding electrons and nuclei. Due to this, the energy levels will spread out to a so-called *energy* band, see Figure 2.1.

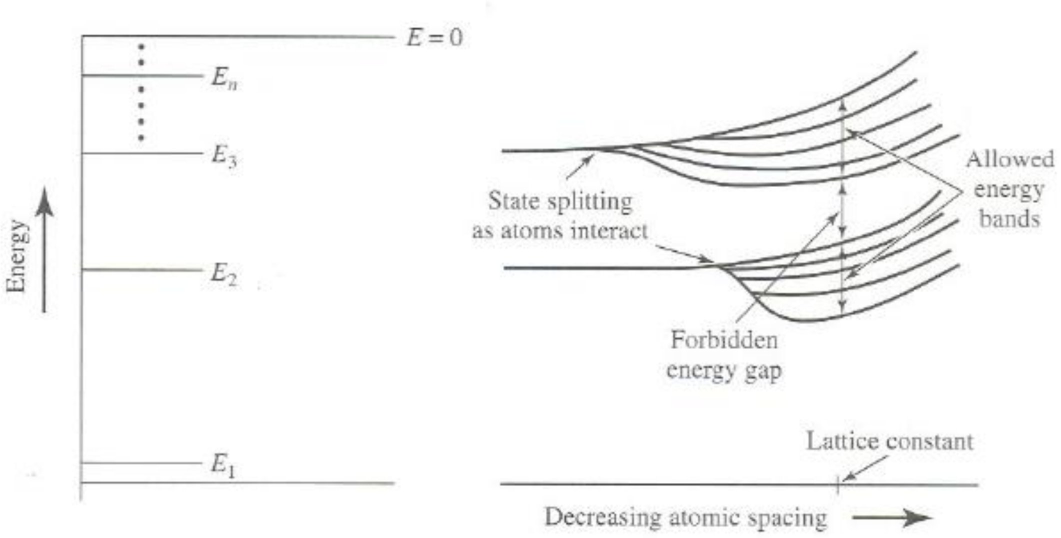

Figure 2.1 Energy levels in a crystal splitting up due to overlapping wave functions [1]

In lower energy bands, the electrons are attached to specific nuclei and cannot move freely through the solid. In higher energy bands however, electrons have enough energy to move freely through the solid and are no longer attached to fixed nuclei and can thus generate a current. The highest energy band in which electrons are still bonded to specific nuclei is called the valence band. The lowest energy band in which electrons have enough energy to freely move through the solid is called the conduction band. The highest energy level within the valence band is called *HOMO* (Highest Occupied Molecular Orbital), whereas the lowest energy level within the conduction band is called *LUMO* (Lowest Unoccupied Molecular Orbital). The difference between the LUMO and the HOMO is called the band gap (E_g). In this band gap are no energy states (in the case of an ideal semiconductor) and this region can be considered as a forbidden energy gap. The differences in properties between insulators, conductors and semiconductors originate from the differences in the location of the Fermi level and the band gap. In conductors, the Fermi level lies either within the conduction band, which ensures that at all temperatures some electrons can freely move through the solid, or the band gap is so small that the thermal energy electrons possess at room temperature is enough to excite them into the conduction band. Another possibility is the existence of an overlap between valence and conduction band. In insulators, the band gap is too large for electrons to cross at room temperature, so practically all electrons will be in the valence band and cannot generate a current through the material. Typical band gap values for insulators are around 3-10eV [3]. In semiconductors, the band gap is usually around 1-2eV [3]. Photons in the visible regime typically have energies within that range and can thus excite electrons from the valence band into the conduction band.

When an electron is excited into the conduction band, it leaves an open place in the valence band, called a hole. This hole acts as a positive mobile charge carrier in the semiconductor material. At room temperature, always some of the electrons will be in the conduction band in semiconductors due to statistical thermal fluctuations in electron energy within the material. To increase the number of free electrons or holes, the semiconductor material can be doped. In pure (undoped) semiconductors, the number of electrons will always be equal to the number of holes. An energy band diagram of an undoped semiconductor is shown in Figure 2.2. The Fermi level is in the middle of the conduction band edge (E_C) and the valence band edge (E_V).

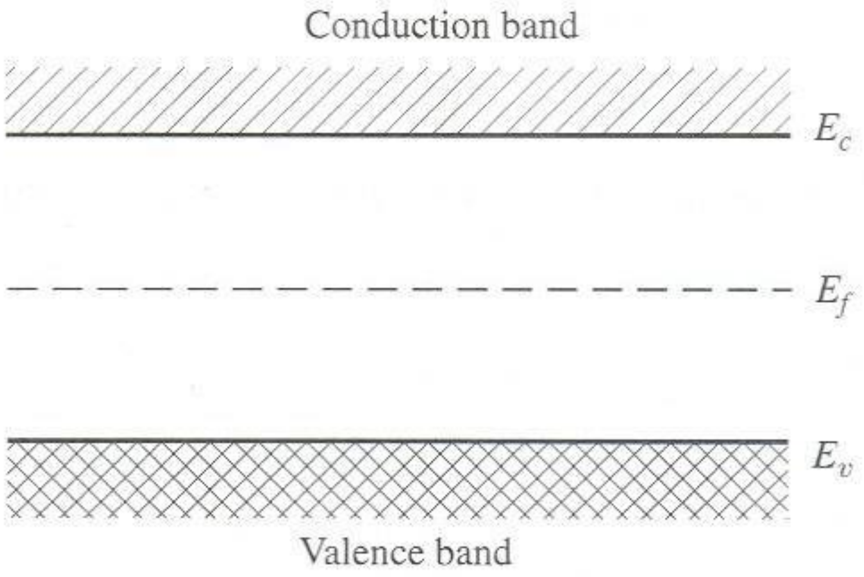

Figure 2.2 Bond Edges and Fermi lever in an undoped semiconductor [1]

2-1-2 *n-type* Semiconductors

Suppose we add some atoms containing five valence electrons to a group IV semiconductor, for instance phosphorous atoms (group V). Compared to silicon atoms, phosphorous atoms have one extra valence electron and the charge of the nucleus will be +15e instead of +14e. In the crystal structure, the fifth electron will be very loosely bound and can easily be excited to the conduction band, see Figure 2.3.

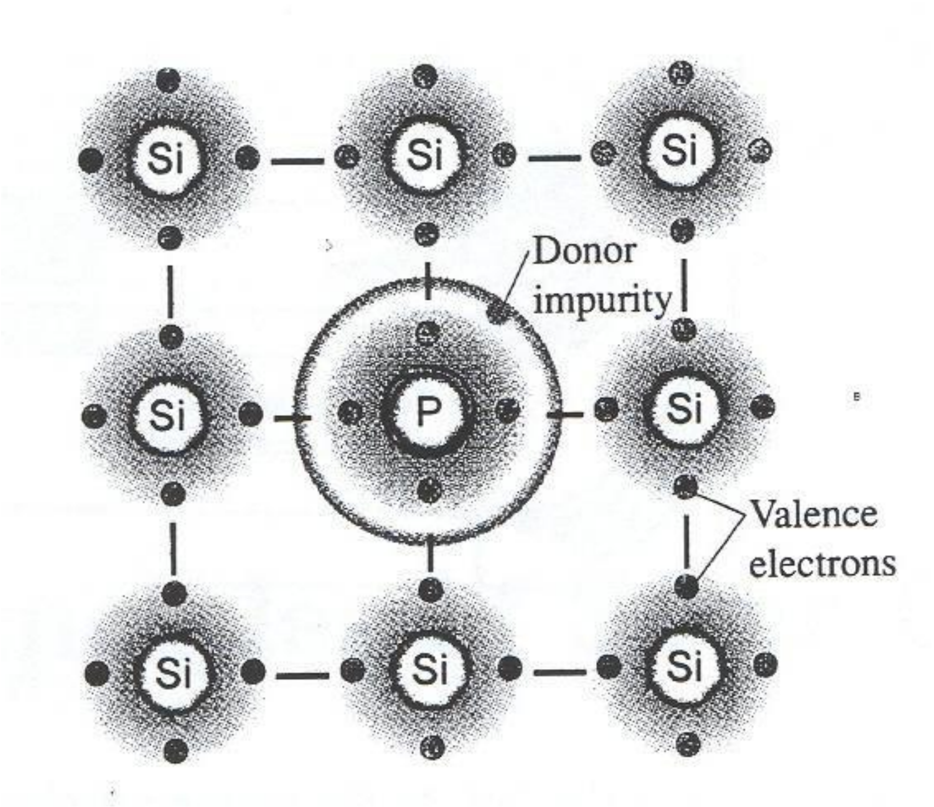

Figure 2.3 Example of n-type doping in Silicon [4]

In the case of phosphorous doping in silicon, the energy needed to excite the dopant electrons into the conduction band is in the order of the thermal energy (kT) at room temperature [5,6,7]. Because of this, a considerable fraction of the phosphorous atoms will add a conduction electron to the crystal under regular operating conditions. The extra electrons coming from the phosphorous impurities, called *donor electrons*, have so-called *donor levels* that are very close to the conduction band, as is schematically shown in Figure 2.4. The Fermi level of the material will shift upwards due to these donor levels. For typical donor densities of 10^{16}-10^{18}cm^{-3}, the Fermi level increase with respect to the intrinsic Fermi level will be proportional to the logarithm of the donor density [1]. In the case of n-type doping, there is just an electron and no hole, so the conductivity of the material is dominated by the electrons, the negative charge carriers. For this reason, semiconductors that are doped with atoms containing more electrons in the outermost electron shell than the material itself are called *n-type semiconductors*.

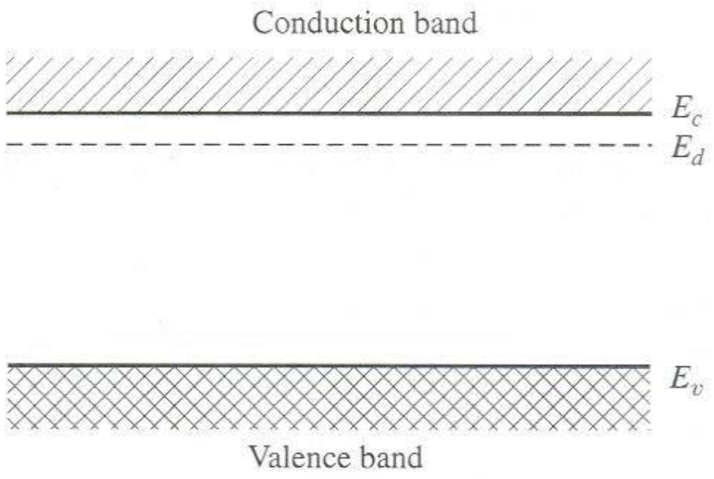

Figure 2.4 Donor lever in an n-type semiconductor. This level lies just below the conduction band

2-1-3 *p-type* Semiconductors

Similarly, atoms containing three valence electrons can be added to a group IV semiconductor. An example could be boron (group III). Boron atoms have only three valence electrons in the outermost electronic shell. In a silicon crystal that is doped with boron atoms, the boron atoms will have four neighboring atoms and just three valence electrons, so there will be a vacant electron position, see Figure 2.5. Electrons from surrounding (silicon) atoms can move to this position, leaving a vacancy in another atom in the crystal. This way, the vacant electron position, which is a hole, can freely travel through the material. At room temperature, the electrons have enough thermal energy to 'jump' from atom to atom, so practically for every boron atom in the crystal, a hole will contribute to the conduction.

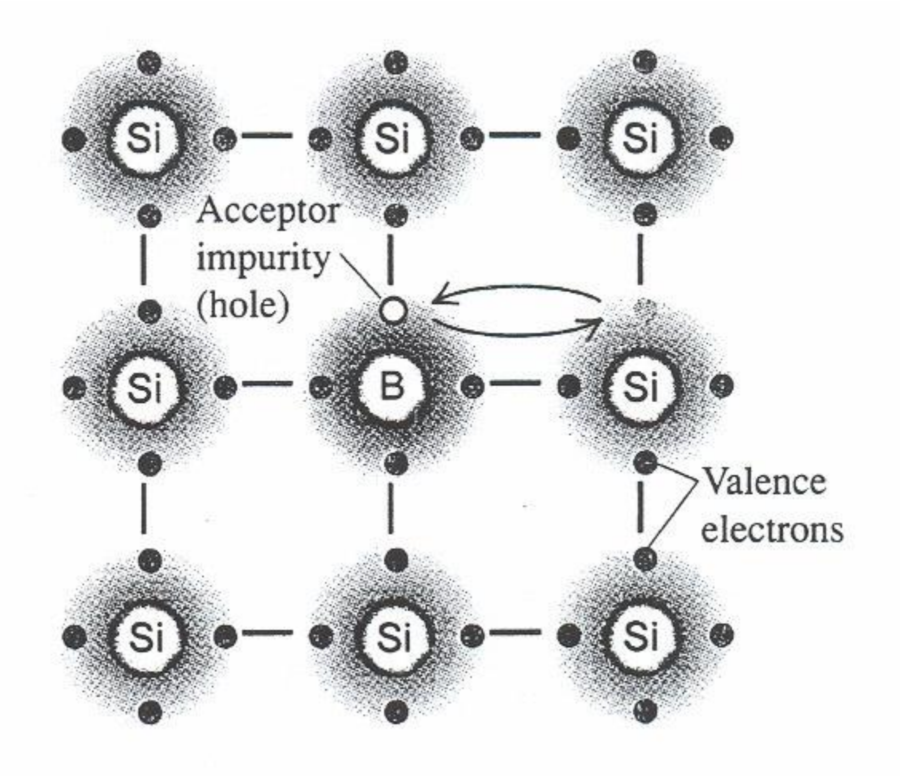

Figure 2,5 Example of p-type doping in silicon [6]

Because the conductivity in materials that are doped with atoms containing less valence electrons is dominated by positive carrier conduction (hole conduction), these materials denoted as *p-type semiconductors*. Please remark that in this case still the electrons are moving, but that a concept has been created in which a net positive charge (electron vacancy) moves through the material. As is the case in n-type material with donor levels, the same happens in p-type material with so-called *acceptor levels*, as can be seen in Figure 2.6. The Fermi level will shift downwards due to the added impurities. This shift, compared to the intrinsic Fermi level, is proportional to the logarithm of the acceptor density in the material for impurity levels of 10^{16}-10^{18}cm^{-3} [1].

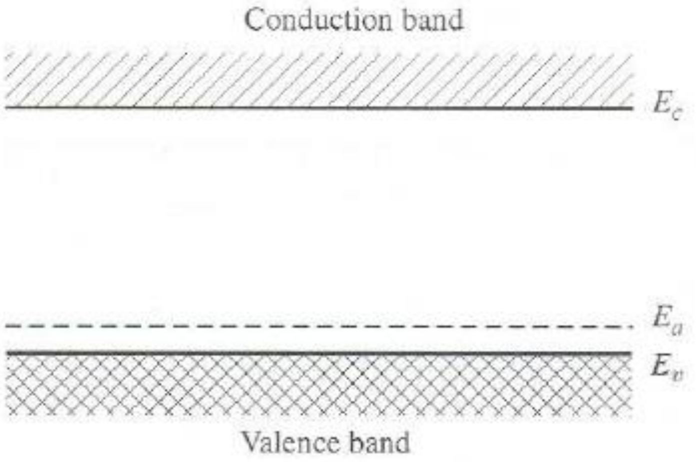

Figure 2.6 Acceptor level in a p-type semiconductor. This level lies just above the valence band. [1]

2-2 General properties of a-Si:H based films

Silicon atoms in amorphous silicon largely retain the same basic structure as that of crystal silicon: each silicon atom is connected by covalent bonds to four other silicon atoms arranged as a tetrahedron. This understanding emerges from measurements of the scattering (“diffraction”) of X rays by the two materials [6] as well as from theoretical and computational studies of the two materials. If you build a noncrystalline silicon structure with wooden sticks (to represent covalent bonds) and wooden balls drilled with four small holes for the sticks (to represent the silicon atoms), you will have some trouble in making a noncrystalline structure. To avoid a crystalline structure, you will need to bend the sticks. Quite soon, you will have to give up on the fourth stick on some atom, and you will have created an imperfect noncrystalline structure with a “dangling bond.” Your problem is related to tetrahedral bonding: there are too many constraints on the positions of atoms to keep all bond lengths and angles reasonably close to the values demanded by silicon’s chemistry in any noncrystalline structure. The same conclusion is reached by mathematical and computational methods [7, 8]. Alloys such as As_2Se_3, which easily form noncrystalline glasses by cooling from a liquid, have an average number of bonds per atom of about 2.7 or less. For hydrogenated amorphous silicon (a-Si:H), silicon–hydrogen bonds resolve this structural problem. Several percent of the silicon atoms make covalent bonds with only three silicon neighbors; the fourth valence electron of the silicon bonds to a hydrogen atom. This crucial hydrogen is essentially invisible to X rays, but is quite evident in nondestructive measurements (proton magnetic resonance [9] and infrared spectroscopy [10]) as well as destructive testing (secondary ion mass spectroscopy [11] and hydrogen evolution during annealing [12]).

There are quite a few distinct atomic configurations for the hydrogen in a-Si:H. The two principal “phases” of hydrogen evidenced by proton magnetic resonance are termed the dilute and clustered phases [9]. In the dilute phase a particular hydrogen atom is about 1 nm away from any other hydrogen atom; in the clustered phase there are two or more hydrogen atoms in close proximity. A computer calculation of a particular instance of this structure [13] is presented in Figure 12.7(a). The densities of hydrogen in each of the individual phases, as well as the total density of hydrogen, depend upon the conditions under which the material is made.

2-2-1 Structure Property

In amorphous silicon, the silicon atoms do not form an ordered matrix, as they do in crystalline silicon, see Figure 2.7. In a-Si, there are slight variations in bond angle, bond length and thereby bond strength, which make the structure non-crystalline. Some valence electrons of silicon atoms in a-Si are unbonded, thereby forming socalled *dangling bonds*. During deposition of a-Si, hydrogen is incorporated, which will *passivate* most dangling bonds. Amorphous silicon in which hydrogen is used to passivate the dangling bonds; hydrogenated amorphous silicon, is usually denoted as a-Si:H.

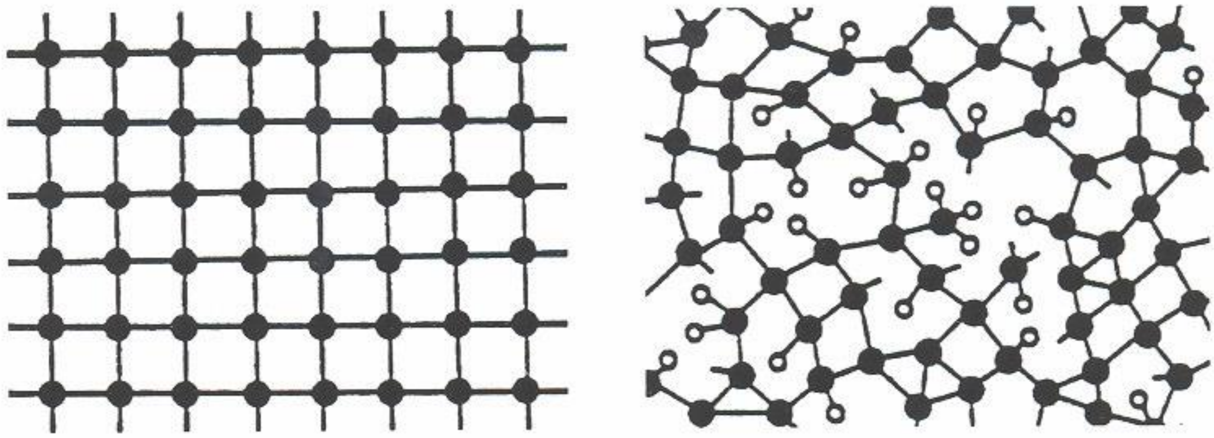

Figure 2.7 Schematic 2D representation of crystalline (left) and amorphous (right) silicon. The closed circles represent silicon atoms; the open circle hydrogen [6]

Because of hydrogen incorporation and the presence of dangling bonds in amorphous silicon, the electronic properties are much poorer compared to c-Si. When an electron-hole pair is created in a-Si, the recombination rate will be much larger than in c-Si, mainly due to the existing dangling bonds. In order to decrease the electronic losses in a-Si based solar cells, pin junctions are most widely used, in which the generated current in the solar cell is not diffusion-based, but drift-based. An undoped intrinsic layer is used to absorb the light, whereas a p- and an n-layer are used to create an electric field in the i-layer. The electric field causes the electrons and the holes to generate a current through the cell and should prevent them to recombine. Because the charge carriers in pin junction based solar cells are separated and drifted by the electric field, pin junction solar cells are said to be drift-based. The main advantage of a-Si compared to c-Si is that a-Si based solar cells can be made much thinner than c-Si based solar cells. Crystalline silicon has an indirect band gap, which means that the highest energy state in the valence band and the lowest energy state in the conduction band have a different momentum. To excite an electron from the valence band into the conduction band, not only a photon is needed to cross the band gap, but also a phonon is needed for momentum conservation. Because both a photon and a phonon are needed simultaneously to excite a valence electron in c-Si into the conduction band, the transition probability for this process to occur is rather small. In amorphous silicon, the band edges are much less sharp than in crystalline silicon and flatten out because of the less ordered structure. Figure 2.8 shows examples of both a direct and an indirect band gap.

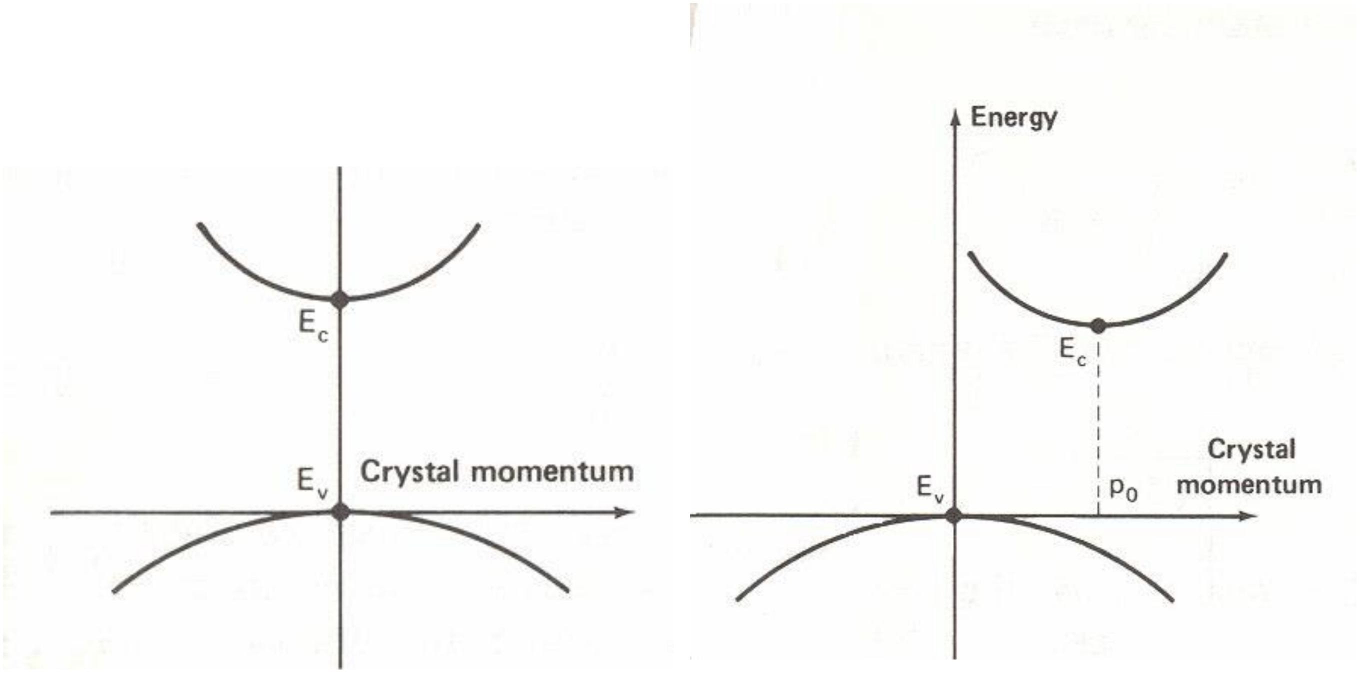

Figure 2.8 Example of direct band gap (left) and an indirect band gap (right) [3]

Due to the direct band gap of a-Si, the absorption probability for photons highly increases compared to c-Si. Because the absorption probability is much higher in a-Si than in c-Si, much thinner layers (about a factor 1000 thinner [1,13]) can be used in solar cell applications. This leads to an increased flexibility and lower production costs. A disadvantage of a-Si is that the quality of the material decreases when being exposed to light. The light exposure causes an increase of the electronic defect density, which somewhat deteriorates the solar cell performance. This effect is called the Staebler Wronski effect (SWE), after its discoverers Staebler and Wronski [12].

2-2-2 Defects and Metastability

While the underlying structure illustrated in Figure 2.9 is noncrystalline, it is a chemically ideal structure: each atom forms the normal number of chemical bonds (four for silicon, one for hydrogen). This noncrystalline atomic structure largely determines the overall electronic and optical properties of the material, as we will discuss shortly. However, many electronic properties in a-Si:H are also strongly affected by the gross defects of chemical bonding. The atomic structure of the bonding defects in a-Si:H has been extensively studied using electron spin resonance. A single type of defect, the D-center, dominates most measurements in undoped a-Si:H [14]. The D-center is generally identified as a silicon dangling bond [15]. A dangling bond may be envisioned using Figure 2.9: just imagine that the hydrogen atom is removed from the dilute-phase site in the lower right-hand corner of the figure, leaving behind a single unbonded electron (the “dangling bond”).

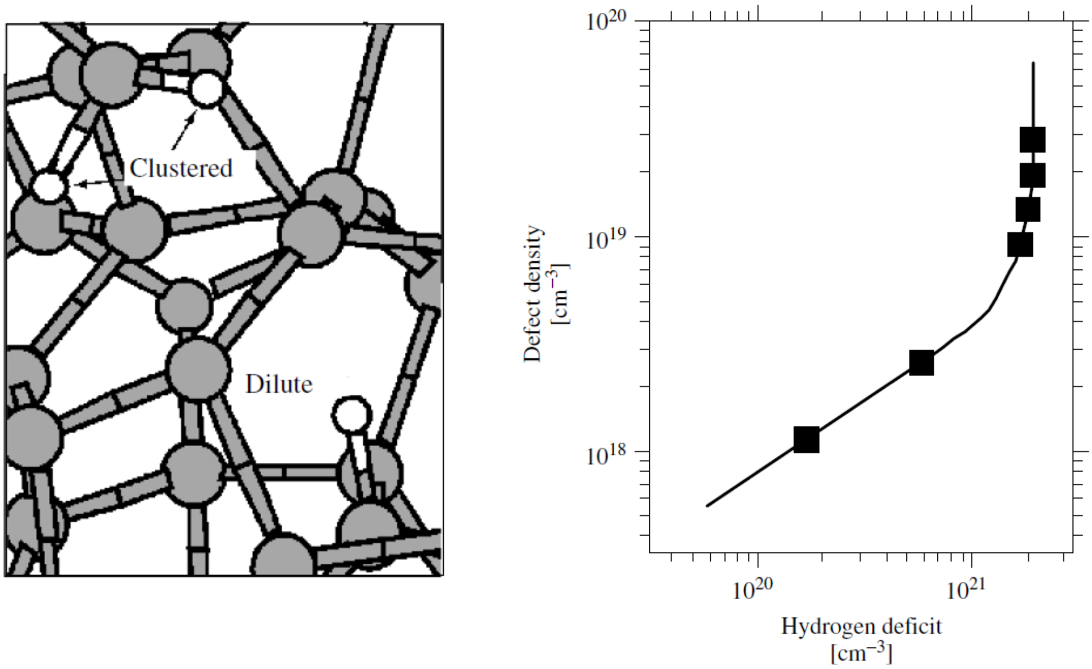

Figure 2.9 (a) Computer model of the chemical bonding of hydrogenated amorphous silicon. The larger, gray spheres indicate Si atoms; the smaller, white spheres indicate hydrogen atoms, which are found in clustered and relatively isolated, dilute-phase configurations as indicated. (b) Correlation of the defect (dangling bond) density in a-Si:H with the density of hydrogen removed from the material by heating (the hydrogen deficit). The data points are derived from deuterium and defect profiles by Jackson et al. [16] (350◦C deuteration). The curve is a fit to a model proposed by Zafar and Schiff [17]

This simple picture is consistent with the following observation: the density of dangling bonds increases when hydrogen is removed from a-Si:H by heating. We present a comparison of a model for this relationship together with measurements illustrating the effect in Figure 2.9 [16,17]. Note that the density of dangling bonds is generally much lower than the density of hydrogen lost from the structure; this effect has been attributed to the evolution of hydrogen from clustered-phase sites, which presumably does not create dangling bonds. The most intense defect research in a-Si:H has not been focused on the direct hydrogen-defect relation, but rather on the light-soaking effects. We illustrated how light soaking degrades the solar conversion efficiency in Figure 2.10 we illustrate how it increases the defect density. For the high intensity illumination, the defect density reaches a steady state at about 10^{17}/cm3. For purposes of engineering and commercial applications, it is very important that a-Si:H reaches such a “stabilized” condition after extended light soaking. Although the defect density is not the only property of a-Si:H modified following light soaking [18], most workers believe that the principal cause of the Staebler–Wronski effect is this increase in dangling bond density after light soaking. The close connection between hydrogen and defects in a-Si:H has led to several efforts to understand the defect creation in terms of metastable configurations of hydrogen atoms [18,19]. The idea is that illumination provides the energy required to shift hydrogen atoms away from their dilutephase sites, thus creating dangling bonds. The technological importance of establishing the atomic mechanism underlying the Staebler–Wronski effect lies in the possibility that this effect can be mitigated in a-Si:H by changing its preparation conditions. An essential feature of the light-soaking effects on a-Si:H cells and films is that most of the effects are “metastable” and can be removed nearly completely by annealing of a light-soaked sample at a temperature above 150◦C. More generally, the stabilized condition of a-Si:H cells and films is quite temperature-dependent. The measurement may be understood by considering that the stabilized condition is due to competition between two rates: the creation of metastable defects by light and a thermally activated process that anneals them away.

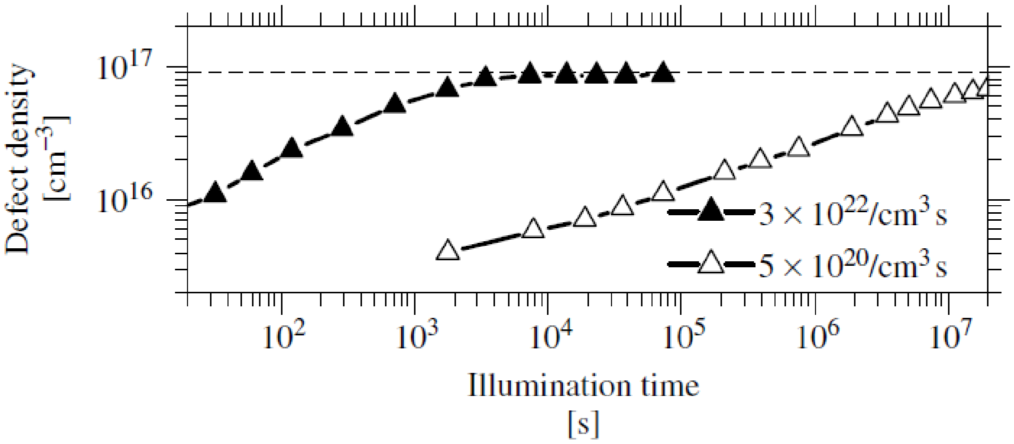

Figure 2.10 Plot of the defect (dangling bond) density during extended illumination of an a-Si:H film as measured by Park, Liu, and Wagner [20]. Data are given for high- and low-intensity illumination; the legend indicates the photo carrier generation rate of each intensity

2-2-3 Electronic Density of States

The most important concept used in understanding the optical and electronic properties of semiconductors is the electronic density-of-states, $g(E)$. The idea is a simple approximation: if a single electron is added to a solid, it may be viewed as occupying a well-defined state (or molecular "orbital") at a particular energy level E. In a range of energies ΔE, the number of such states per unit volume of the solid is $g(E)\ \Delta E$. In Figure 12.9 we have illustrated the density-of-states for hydrogenated amorphous silicon as it has emerged primarily from measurements of electron photoemission [21, 22], optical absorption [23], and electron and hole drift mobilities [24]. In the dark at low temperatures, the states with energies below the Fermi energy E_F are filled by electrons; above the Fermi energy the states are empty. There are two strong bands of states illustrated: an occupied valence band ($E < E_V$), originating with the Si–Si and Si–H bonding orbitals and an unoccupied conduction band ($E > E_C$), originating with "antibonding" orbitals. Between the conduction and valence bands lies an "energy gap" where the density-ofstates is very low. Any functional semiconductor, crystalline or noncrystalline, must have such an energy gap. For perfect crystals, the valence and conduction bandedge energies E_V and E_C are well defined, as is the band gap $E_G = E_C - E_V$. Interestingly, in disordered semiconductors there are exponential distributions of bandtail states near these bandedges.

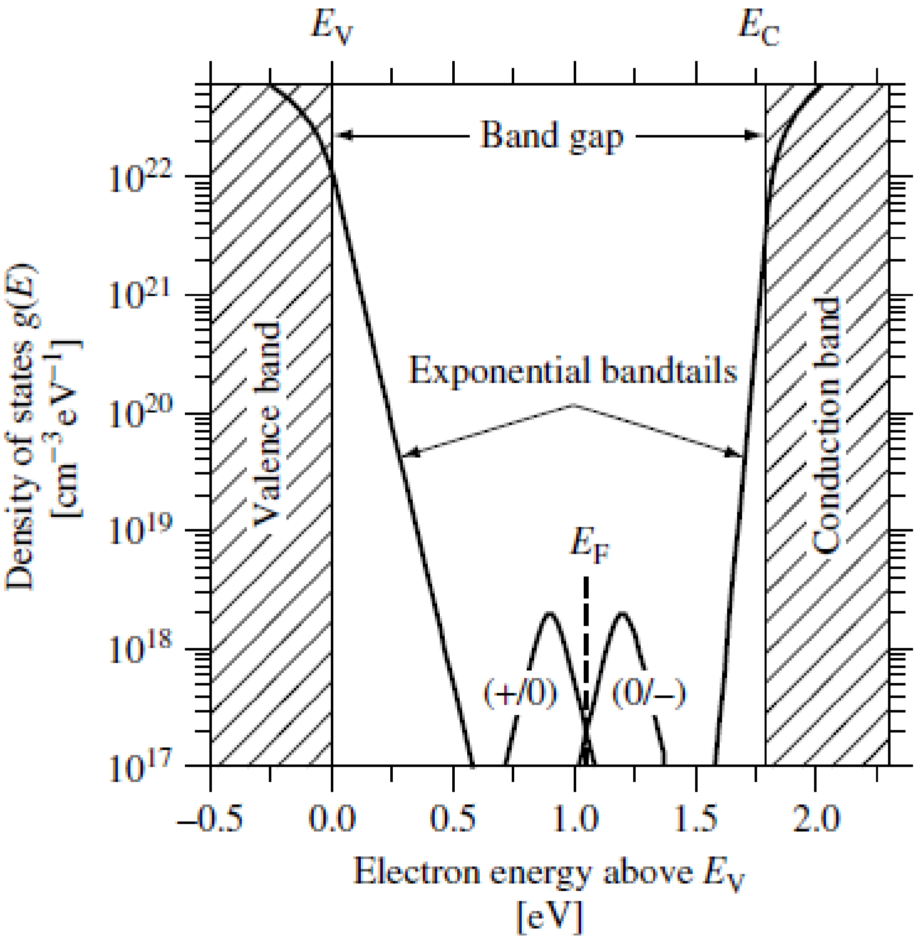

Figure 2.11 Density of electronic states g(E) in hydrogenated amorphous silicon. The shaded areas indicate delocalized states in the bands; these bands themselves have tails of localized states with an exponential distribution. Midway between the bands are levels belonging to gross defects such as dangling Si bonds indicated by the two peaked bands around EF

For the valence bandtail, we write $g(E) = g_V \exp[-(E - E_V)/\Delta E_V]$. The width ΔE_V of this exponential distribution is important in interpreting optical absorption experiments, in which it is usually identified with the exponential "Urbach" tail of the spectrum apparent in Figure 12.2. For a-Si:H, a typical value $\Delta E_V = 50 \times 10^{-3}$ eV. ΔE_V is also used to account for the very slow drift of holes in an electric field (i.e. the *hole drift mobility*) [24,25]. The conduction bandtail width ΔE_C is much narrower; for the best a-Si:H materials, it is about 22×10^{-3} eV, but increases markedly for amorphous silicon-germanium alloys [26]. Given the presence of exponential bandtails, the very existence of bandedge energy can reasonably be questioned. Remarkably, detailed analysis of drift-mobility measurements supports the concept of a well-defined bandedge [24, 27]. Most workers consider the bandedge to be the energy that separates electron orbitals that are localized (i.e. have well-defined locations in space) from orbitals that are delocalized. The bandedges are correspondingly termed the conduction and valence band *mobility edges* [28]. Unfortunately, for noncrystalline semiconductors there is no single, conclusively established procedure for locating the bandedges within the density-of-states. The band gap is thus difficult to determine without some ambiguity. Since amorphous silicon–based materials with varying band gaps are used in solar cells, it is nonetheless very important to establish conventional procedures for comparing band gaps. By far the most common approach is to analyze measurements of the optical absorption coefficient $\alpha(h\nu)$ similar to those in Figure 12.2; one typical analysis yields an "optical" or "Tauc" band gap E_T [29]

$$\alpha(h\nu) = (\mathrm{A}/\mathrm{h}\nu)(h\nu - E_T)^2 \tag{2.2}$$

The proportionality constant A incorporates several effects and is not usually studied separately. The band gap obtained using this procedure is typically about 1.75 eV in a-Si:H, but varies substantially with deposition conditions and alloying with germanium or carbon. A simpler procedure than that of Tauc is to define the band gap to be the photon energy corresponding to a particular optical absorption coefficient α; using $\alpha = 3 \times 10^3$/cm yields values (denoted as $E_{3.5}$) similar to the Tauc procedure. Finally, there is undoubtedly a difference between these optical estimates of the band gap and the true, "electrical" band gap $E_G = E_C - E_V$. Internal photoemission measurements [30] indicate that the electrical band gap is 50 to 100 meV larger than the Tauc band gap. Between the bandtails lie defect levels; in undoped a-Si:H, these levels appear to be due entirely to the dangling bonds ("*D*-centers") measured by electron spin resonance. For example, infrared absorption at photon energies around 1.2 eV is sensitive to the optical processes that detach an electron from a defect and promote it to the conduction band or that transfer an electron from the valence band to a defect. This infrared signal is visible in Figure 12.2; for samples of varying electronic properties, the infrared absorption coefficient is proportional to the D-center density over a range of at least a factor of 100 in the density [31]. The next issue to be resolved is the positions of the corresponding levels, as illustrated in Figure 12.9. The *D*-center is "amphoteric:" there are three charge states (with +e, 0, and −e charges), leading to two levels (transitions between the 0/+ and −/0 charge states). A rough guide to level positions estimated under near-dark conditions is the following. The (−/0) level is about 0.6 eV below E_C in low defect-density, undoped a-Si:H [48]. The (+/0) level lies about 0.3 eV below the (−/0) levels;

the difference between the 2 levels is usually termed the *correlation energy* of the *D*-center [33]. The actual level positions apparently vary between doped and intrinsic a-Si:H [6], between intrinsic samples with varying densities of *D*-centers [32], and possibly between dark and illuminated states [34].

2-2-4 Optical Properties

The structural and optical properties we have described can be varied substantially by changes in deposition conditions. For example, changing the substrate temperature or the dilution of silane by hydrogen (in plasma deposition) causes a change in the optical band gap for a-Si:H films over at least the range 1.6 to 1.8 eV [35]; these changes can be ascribed to changes in the hydrogen microstructure of the films. Even larger changes can be effected by alloying with additional elements such as Ge, C, O, and N; alloying is readily accomplished by mixing the silane (SiH_4) source gas with gases such as GeH_4, CH_4, O_2 or NO_2, and NH_3, respectively. The resulting alloys have very wide ranges of band gaps, as we illustrate for a-$Si_{1-x}Ge_x$:H in Figure 12.10. For simplicity, we shall usually refer to these alloys using the abbreviated notation: a-SiGe for a-$Si_{1-x}Ge_x$:H, and so on. Only some of these materials have proven useful in devices. In particular, a-SiGe alloys with optical gaps down to about 1.45 eV are employed as absorber layer in multijunction *pin* cells; the narrower band gap of a-SiGe compared to a-Si allows for increased absorption of photons with lower energies [36]. Figure 12.10(a) illustrates how the spectrum of the absorption coefficient $\alpha(h\nu)$ changes for a-SiGe alloys with different atomic percentages x; the different optical band gaps are indicated as labels.

Two features of these data should be noted. First, the Urbach slopes remain constant (at about 50 meV) over the entire range of band gaps. Second, the plateau in the absorption coefficient at the lowest photon energies increases steadily as the band gap diminishes, which is indicative of a corresponding increase in defect density.

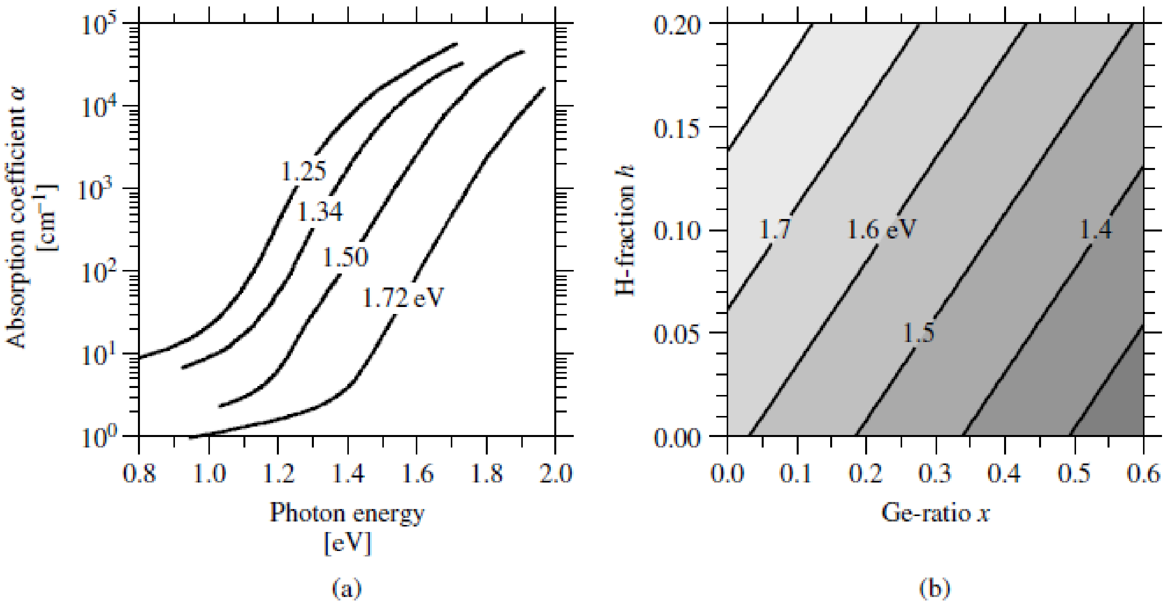

Figure 2.12 (a) Absorption coefficient spectra for a-SiGe alloys; the optical band gaps and corresponding Ge fractions x are 1.25 to 0.58, 1.34 to 0.48, 1.50 to 0.30, 1.72 to 0.0 [36]. (b) Typical optical band gaps for a-$Si_{1-x}Ge_x$:H alloys for varying Ge-ratio x and atomic fraction *h* of hydrogen

Figure 12.10(b) is a contour plot showing how the optical band gap of a-$Si_{1-x}Ge_x$:H varies with the Ge-ratio *x* and with atomic fraction *h* of hydrogen. The figure reflects experimental results for a-Si:H alloys of varying H-fraction [35] and for a-SiGe:H alloys for which both *x* and *h* were reported [37].5 Note that, for constant fraction *h*, the band gap decreases about 0.7 eV as the Ge ratio *x* increases from 0 to 1. The band gap increases with atomic fraction of hydrogen *h*. Figure 12.10(b) should be viewed as a useful approximation; in particular, the atomic fraction *h* is only one aspect of the hydrogen microstructures in a-SiGe alloys, and quantitative deviations from the contour plot are likely. Additionally, only some of the materials represented in the figure are useful as absorber layers. In particular, as the Ge ratio *x* rises to about 0.5, the optoelectronic properties become so poor that these alloys are no longer useful in solar cells [38]. Similarly, only limited ranges of the atomic fraction of hydrogen *h* yield useful absorber layers. It might be thought that a-SiC would be equally useful as a wider band gap absorber; despite some promising research [39], this material is not being used as an absorber layer by manufacturers. B-doped a-SiC is used extensively as a *p*-type, window layer [40]. a-SiO and a-SiN are used as insulators in thin-film transistors [41], but are not major components in solar cells.

2-3 General Principle of Amorphous Silicon Solar cells

A solar cell is a semiconductor device that produces electrical current (and then sends it through an external load) when exposed to light (photovoltaic effect).The operation of a solar cell consists of two main steps;

(1) Creation of electron-hole pairs, i.e. generation of free electrons and holes through the absorption of photons

(2) Separation of the free electrons and holes in order to actually produce electricity

The efficiency η of a solar cell is the ratio of the electrical output power to the incident light power. The performance of solar cells under illumination can be described using their current-voltage (*I*-*V*) characteristics. In fact, it is sufficient to characterize the current-voltage characteristics only with a few parameters. If considering a typical current-voltage curve of a p-n junction diode in the dark and under illumination, three parameters are defined to give a complete description of the electrical behavior; these are (i) open-circuit voltage (V_{oc}), (ii) short-circuit current (J_{sc}), and (iii) fill factor (*FF*). V_{oc} and J_{sc} are the values of voltage and current which are obtained under illumination when I = 0 and V = 0, respectively, while *FF* is defined by

$$FF = \frac{V_m I_m}{V_{oc} I_{sc}} \tag{2.3}$$

where V_m and I_m are output voltage and output current at the maximum operating point, respectively. The efficiency η is then defined by

$$\eta = \frac{V_m \times I_m}{P_{in}} = \frac{V_{oc} \times I_{sc} \times FF}{P_{in}} \tag{2.4}$$

where P_{in} is the input energy to the solar cells.

In a dark state (without illumination), the expression of the dark current (I_d) is the same as the current flowing in p-n junction diode

$$I_d = I_0\left\{exp\left(\frac{qV}{nkT}\right)-1\right\} \tag{2.5}$$

where I_0 is the reverse saturation current, q is the electron charge, V is the applied voltage, n is the diode factor representing deviation from idea diode characteristics, k is Boltzmann's constant and T is the absolute temperature. Under light illumination, a photocurrent (I_{ph}) is generated as diode reverse current, hence the current-voltage relationship becomes

$$I = -I_{ph} + I_0\left\{\left(\frac{qV}{nkT}\right)-1\right\} \tag{2.6}$$

I is the net current which also can be described as $I = I_d - I_{ph}$. From equations (2.5) and (2.6), the V_{oc} can be expressed as

$$V_{oc} = \frac{nkT}{q}ln\left(\frac{I_{ph}}{I_0}+1\right) \tag{2.7}$$

where the reverse saturation current I_0 can be expressed as

$$I_0 = A\left(\frac{qD_e n_i^2}{L_e N_A}+\frac{qD_h n_i^2}{L_h N_D}\right) \tag{2.8}$$

where A is the area, N_A and N_D are the acceptor and donor concentration, respectively, D_e and D_h are the diffusion coefficient for electron and hole, respectively, L_e and L_h are the minority carrier diffusion length for electron and hole, respectively. The intrinsic carrier concentration n_i in equation (2.8) can be expressed as

$$n_i^2 = N_c N_v e^{\left(-\frac{E_g}{kT}\right)} \tag{2.9}$$

where N_c and N_v are the effective density of state in the conduction and valence band, respectively.

From equation (2.7), we can clearly see that high V_{oc} can be obtained when I_0 is as small as possible. Moreover, from equations (2.8) and (2.9) we also can see that that small I_0 can be achieved by using wide band gap materials. This relationship reveals that the use of wide band gap materials will result in high V_{oc} solar cells.

2-3-1 Single Junction Structure solar cell

Typically a-Si:H-based solar cells have a p-i-n or n-i-p diode structure depending on the deposition sequence of doped and intrinsic layers. For both structures the light is entering through the p-layer which efficiently supports hole collection in the device. The reason for this is the smaller mobility of holes compared to electrons. A transparent conductive oxide (TCO) film contacts the a-Si:H diode from the front side and, in the most simplest case, a metal film serves both as rear contact and back reflector (see Figs. 1 and 2a). The very thin (10–30 nm) p- and n-doped layers build up

an electric field over the intrinsic (i) layer (typical thickness: 200–500 nm). Electrons and holes generated in doped layers do not (or only partly) contribute to the photo-current due to their short lifetime in highly doped a-Si:H. Therefore, wide-band-gap a-SiC:H [42] and a-SiO:H [43] alloys or microcrystalline Si films [44] are applied as p-doped window layers to reduce absorption losses. Electrons and holes generated in the i-layer are driven to the n- and p-layer, respectively, by the internal electric field. The material quality of the intrinsic layer and the strength and distribution of the electric field are responsible for the charge carrier collection and mainly determine the solar cell performance. Defects affect the charge carrier collection in two different ways. On the one hand they act as recombination centers, and on the other hand their charge state influences the electric field distribution in the i-layer. According to the energy position of the Fermi level, defect states in the front part of the i-layer adjacent to the p-layer are positively charged (DC states), whereas defects adjacent to the n-layer are negatively charged ($D-$). These charged defects enhance the electric field in the p/i and n/i-interface regions, whereas the field is reduced in the volume of the i-layer. The p=i-interface region turns out to play a crucial role for solar cell optimization. Experimental results show that very small changes of the p=i-interface design significantly affect initial solar cell performance and the stability upon light exposure. Intrinsic wide-band-gap p=i-interface layers improve the open-circuit voltage [45, 46, 47]. However, these layers often provoke additional degradation due to a redistribution of the electric field. Optimization schemes for the p/i-interface region which improve the stabilized cell performance performance are given in [48]. A second critical interface is the TCO/p-contact. The holes in the p-layer recombine at the TCO/p-interface with electrons from the degenerately n-doped TCO film. Depending on the TCO material a depletion of the amorphous p-layer causes a contact barrier at the TCO/p-interface [49, 50]. Microcrystalline Si p-layers provide a low ohmic TCO/p-interface in this case [49–51]. For a more detailed discussion of interfaces in a-Si:H solar cells see for example [52].

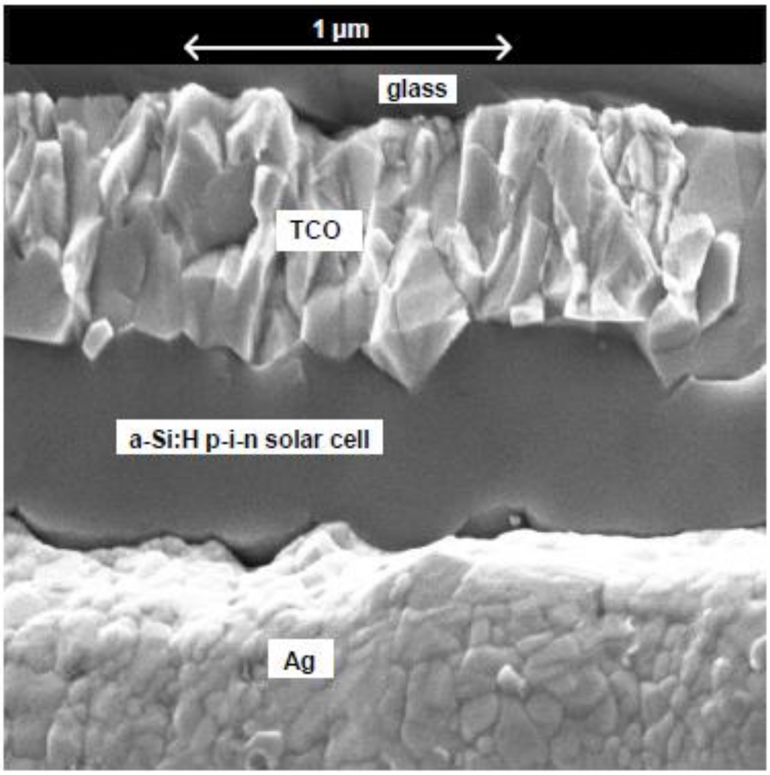

Figure 2.13 High Resolution Scanning Electron Microscopy (HRSEM) Cross section of an a-Si:H p-i-n single junction solar cell [53]

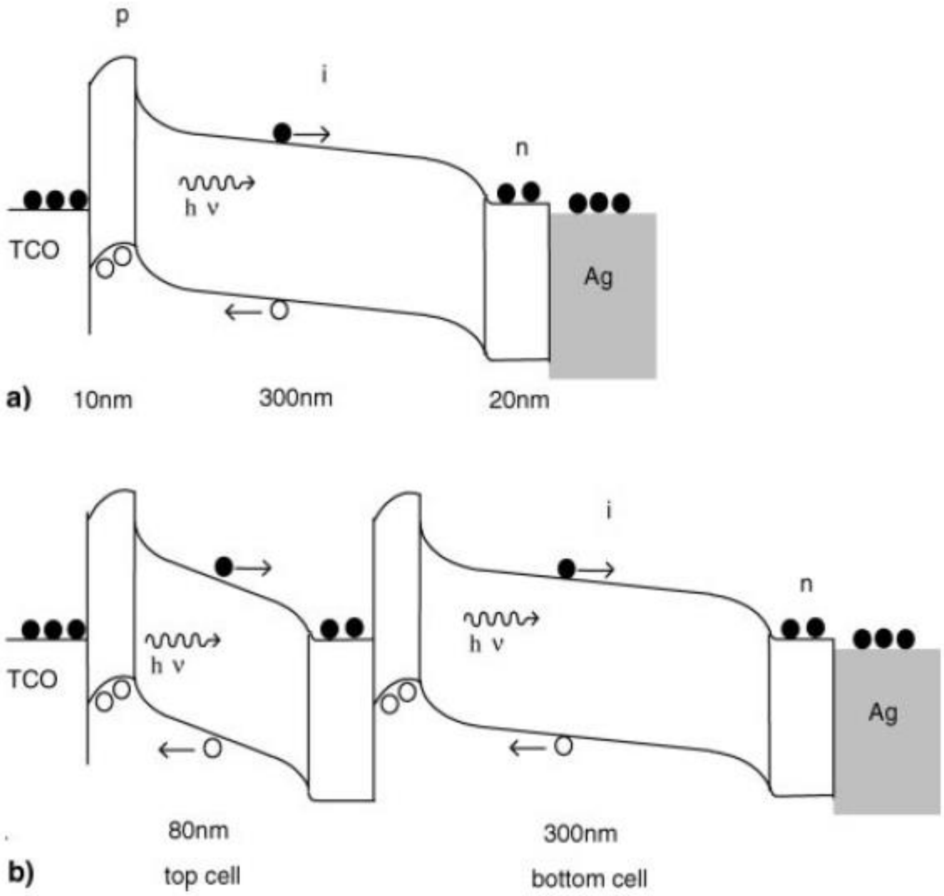

Figure 2.14a,b. Schematic sketch of the band diagramm of an a-Si:H p-i-n single junction (a), and an a-Si:H/a-Si:H p-i-n/p-i-n stacked junction solar cell (b)[53]

2-3-2 Multi-Junction Structure solar cell

The stacked-cell concept has emerged as a successful tool to improve the light stability of a-Si:H-based solar cells [54, 45]. A simple a-Si/a-Si stacked cell is schematically sketched in Fig. 2.14 b. The requirement of current matching results in top cells being much thinner than the bottom cell. Consequently, the built-in field in the top cell is distinctly higher, which strongly reduces the decrease of cell performance by light induced defect creation. The thicker bottom cell is more stable than a comparable single-junction cell because the intensity of the incident light is reduced due to the top cell acting as n-p junctions has been solved by the use of microcrystalline contact layers [54, 55–58]. In a state-of-the-art stacked cell, the stabilized fill factor is higher than in a single-junction cell with equal total i-layer thickness, the n-p junction provides low optical and electrical loss, and the open-circuit voltages of the component cells add to the stacked cell *V*oc. Thus, the optimization of a stacked cell is to a large extent reduced to the optimization of the component cells. Besides the higher stability, the stacked cell approach offers the possibility to use different band gaps for the component cells, which allows a more efficient utilization of the solar spectrum [59]. Wide-band-gap top cells convert the blue and green part of the sunlight at high voltages, while the red and infrared part light is transmitted and absorbed in the bottom cell

REFERENCE

[1] R.S. Muller, T.I. Kamins, Device Electronics for Integrated Circuits, John Wiley & Sons (2003) Third Edition

[2] R.E.I. Schropp, M.Zeman, Amorphous and Microcrystalline Silicon Solar Cells – Modeling, Materials and Device Technology, Kluwer Academic Publishers (1998)

[3] P.C.P. Bronsveld, J.K. Rath, R.E.I. Schropp, Temperature and H2-dilution dependence of silicon layers deposited at temperatures up to 1000C by VHF PECVD, Proceedings of the 20th European PVSEC, Barcelona (2005) 1675-1678

[4] F.-J. Haug, V. Terrazzoni-Daudrix, T. Söderström, X. Niquille, J. Baillat, C. Ballif, Flexible microcrystalline silicon solar cells on periodically textured plastic substrates, Proceedings of the 21st European PVSEC, Dresden (2006) 1651-1654

[5] B.H. Bransden, C.J. Joachain, Quantum Mechanics, Prentice Hall (2000) Second Edition

[6] A. Gordijn, Master Thesis, Universiteit Utrecht (2000)

[7] S.M. Sze, Physics of Semiconductor Devices, John Wiley & Sons (1981) Second Edition

[8] P. Kumar, D. Bhusari, D. Grunsky, M. Kupich, B. Schroeder, p-doped μc-Si:H window layers prepared by hot-wire CVD for amorphous solar cell application**,** Solar Energy Materials and Solar Cells, **90** (2006) 3345-3355

[9] J. Merten, C. Voz, A. Muñoz, J.M. Asensi, J. Andreu, The role of the buffer layer in the light of a new equivalent circuit for amorphous silicon solar cells, Solar Energy Materials and Solar Cells **57 (2)** (1999) 153-165

[10] M.K. van Veen, Ph.D. Thesis, Universiteit Utrecht (2003)

[11] W.G.J.H.M. van Sark, Private Communications (March 2007)

[12] D.L. Staebler, C.R. Wronski, Reversible conductivity changes in discharge produced amorphous Si, Applied Physics Letters, **31** (1977) 292-294

[13] S. Veprek, V. Marecek, The preparation of thin layers of Ge and Si by chemical hydrogen plasma transport, Solid State Electronics **11** (1968) 68

[14] Street R, *Hydrogenated Amorphous Silicon*, Cambridge University Press, Cambridge (1991).

[15] The assignment of the D-center observed in electron paramagnetic resonance measurements with a dangling bond has been challenged in favor of "floating bonds" (Stathis J, Pantelides S, *Phys. Rev. B* **37**, 6579–6582 (1988))

[16] Jackson W, Tsai C, Thompson R, *Phys. Rev. Lett.* **64**, 56 (1990).

[17] Zafar S, Schiff E, *Phys. Rev. Lett.* **66**, 1493 (1991).

[18] The review of Fritzsche H, *Annu. Rev. Mater. Res.* **31**, 47 (2001).

[19] Branz H, *Phys. Rev. B* **59**, 5498 (1999).

[20] Park H, Liu J, Wagner S, *Appl. Phys. Lett.* **55**, 2658 (1989).

[21] Ley L, J. Non-Cryst. Solids 114, 238 (1989).

[22] Jackson W, Kelso S, Tsai C, Allen J, Oh S, Phys. Rev. B 31, 5187 (1985).

[23] Cody G, Tiedje T, Abeles B, Brooks B, Goldstein Y, Phys. Rev. Lett. 47, 1480 (1981).

[24] Tiedje T, in Joannopoulos J, Lucovsky G, Eds, Hydrogenated Amorphous Silicon II , 261–300, Springer-Verlag, New York (1984).

[25] Gu Q, Wang Q, Schiff E, Li Y, Malone C, J. Appl. Phys. 76, 2310 (1994).

[26] Wang Q, Antoniadis H, Schiff E, Guha S, Phys. Rev. B 47, 9435 (1993).

[27] Gu Q, Schiff E, Chevrier J, Equer B, Phys. Rev. B 52, 5695 (1995).

[28] Mott N, Conduction in Non-Crystalline Solids, Oxford University Press, Oxford (1987).

[29] Tauc J, in Abeles F, Ed, Optical Properties of Solids, 277–313, North Holland, Amsterdam (1972).

[30] Chen I, Wronski C, J. Non-Cryst. Solids 190, 58 (1995).

[31] Jackson W, Amer N, Phys. Rev. B 25, 5559 (1982).

[32] Antoniadis H, Schiff E, Phys. Rev. B 46, 9482–9492 (1992).

[33] Lee J, Schiff E, Phys. Rev. Lett. 68, 2972 (1992).

[34] Han D, Melcher D, Schiff E, Silver M, Phys. Rev. B 48, 8658 (1993).

[35] Hama S, Okamoto H, Hamakawa Y, Matsubara T, J. Non-Cryst. Solids 59–60,333, 1983).

[36] Guha S, Payson J, Agarwal S, Ovshinsky S, J. Non-Cryst. Solids 97–98, 1455, (1987).

[37] Middya A, Ray S, Jones S, Williamson D, J. Appl. Phys. 78, 4966 (1995).

[38] Stutzmann M, Street R, Tsai C, Boyce J, Ready S, J. Appl. Phys. 66, 569 (1989).

[39] Li Y, Proc. Materials Research Society Symp., 297, 803–814 (1994).

[40] Arya R, Catalano A, Oswald R, Appl. Phys. Lett. 49, 1089 (1986).

[41] Tsukada T, in Street R, Ed, Technology and Applications of Amorphous Silicon, 7–93, Springer, Berlin, Germany (2000).

[42] Y. Tawada, M. Kondo, H. Okamoto, Y. Hamakawa: Solar Energy Mater. **6**, 299 (1982)

[43] S. Fujikake, H. Ohta, A. Asano, Y. Ichikawa, H. Sakai: Mater. Res. Soc. Symp. Proc. **258**, 875 (1992)

[44] S. Guha, J. Yang, P. Nath, M. Hack: Appl. Phys. Lett. **49**, 218 (1986)

[45] H. Sakai, Y. Ichikawa: J. Non-Cryst. Solids **137**=**138**, 1155 (1991)

[46] K.S. Lim, M. Konagai, K. Takahashi: J. Appl. Phys. **56**, 538 (1984)

[47] R.R. Arya, A. Catalano, R.S. Oswald: Appl. Phys. Lett. **49**, 1089 (1986)

[48] B. Rech, C. Beneking, H. Wagner: Solar Energy Mater. Solar Cells **41**=**42**, 475 (1996)

[49] M. Kubon, E. Böhmer, F. Siebke, B. Rech, C. Beneking, H. Wagner: Solar Energy Mater. Solar Cells **41**=**42**, 485 (1996)

[50] E. Böhmer, F. Siebke, B. Rech, C. Beneking, H. Wagner: Mater. Res. Soc. Symp. Proc. **426**, 519 (1996)

[51] B. Rech, S. Wieder, C. Beneking, A. Löffl, O. Kluth, W. Reetz, H. Wagner: In Proc. 26th IEEE Photovolt. Specialists Conf. (IEEE, Piscataway 1997) p. 619

[52] H. Stiebig, F. Siebke, W. Beyer, C. Beneking, B. Rech, H.Wagner: Solar Energy Mater. Solar Cells **48**, 351 (1997)

[53] B. Rech, H. Wagner ; Appl. Phys. A 69, 155–167 (1999)

[54] Y. Uchida: In Proc. 7th Europ. Photovolt. Solar Energy Conf., ed. By A. Goetzberger, W. Palz, G. Willeke (Reidel, Dordrecht 1986) p. 395

[55] L. Yang, L. Chen, S.Wiedemann, A. Catalano: Mater. Res. Soc. Symp Proc. 283, 463(1993)

[56] M. Kolter, C. Beneking, D. Pavlov, T. Eickhoff, P. Hapke, S. Frohnhoff, H. Münder, H.Wagner: In Proc. 23rd IEEE Photovolt. Specialists Conf. (IEEE, Piscataway 1993) p. 1031

[57] A. Banerjee, J. Yang, T. Glatfelter, K. Hoffman, S. Guha: Appl. Phys. Lett. 64, 1517 (1994)

[58] N. Pellaton Vaucher, B. Rech, D. Fischer, S. Dubail, M. Goetz, H. Keppner, N. Wyrsch, C. Beneking, O. Hadjadj, V. Shklover, A. Shah: Solar Energy Mater. Solar Cells 49, 27 (1997)

[59] G. Nakamura, K. Sato, Y. Yukimoto: In Proc. 16th IEEE Photovolt. Specialists Conf. (IEEE, New York 1982) p. 1331

Chapter 3

Theoretical Analysis of a-Si:H based Solar cell with Spectrum Splitting Technique

3-1 Introduction

In order to predict the experimental results, it is necessary to understand the behavior of the incorporate of several materials which consist of p, i and n layers [1-8]. In this chapter, in order to determine material parameter sets for both top and bottom cells, a numerical analysis was carried out using a one-dimensional device simulation program AMPS-1D (Analysis of Microelectronic and Photonic Structures) [9]. The electrical and optical parameters have taken from experimental results and some literatures [10-19].

3.2 AMPS-1D Device Simulation Program

3.2.1 Overview of AMPS-1D

AMPS-1D was developed by Prof. Stephen J. Fonash and his group from Pennsylvania State University under the support of the Electric Power Research Institute (EPRI). AMPS-1D is a one-dimensional computer program for simulating transport physics in solid-state devices. It uses the first-principles theory and the Poisson's equations approach to analyze the transport behavior of semiconductor electronic and optoelectronic device structures. These device structures can be composed of crystalline, polycrystalline or amorphous materials as well as combinations thereof. In the AMPS-1D simulation program, a maximum of 30 layers can be used as one single device with each layer having its own set of parameters such as optical bandgap, effective density of states, mobility, and other parameters. All parameters are independence of temperature. Moreover, each layer can be assigned a total of 50 deep donor and acceptor levels, resulting in possibility of creating almost any density of state distribution8). AMPS-1D device simulator uses the Newton-Raphson technique to numerically solve three governing semiconductor device equations, i.e., the Poisson equation, the electron and the hole continuity equations, without making any assumptions about the mechanism controlling transport in these devices.

3.2.2 Simulation Model of AMPS-1D

As previously mentioned, AMPS-1D solves three semiconductor equations, i.e., the Poisson equation, the electron and the hole continuity equations. In this sub-section, the simulation model used in AMPS-1D program including these three semiconductor equations, are explained in more detail.

First, the Poisson's equation is given as

$$-\frac{d}{dx}\left(\varepsilon(x)\frac{d\Psi}{dx}\right) = q[p(x) - n(x) + N_D^+(x) - N_A^-(x) + p_t(x) - n_t(x)] \tag{3.1}$$

Where the electronic potential ψ and the free electron n, free hole p, trapped electron n_t , and trapped hole p_t , as well as the ionized donor-like doping N_D^+ and ionized acceptor-like doping N_A^- concentrations are all functions of the position of coordinate x. Here, ε is the permittivity and q is the magnitude of the charge of an electron.

The free electron n and free hole p concentrations are given as the following

$$\mathrm{n} = N_c \cdot F\,{}^{1}\!/_{2}\ \exp\left(\frac{E_F - E_C}{kT}\right) \tag{3.2}$$

$$\mathrm{n} = N_c \cdot F\,{}^{1}\!/_{2}\ \exp\left(\frac{E_V - E_F}{kT}\right) \tag{3.3}$$

In these equations, N_C and N_V are the band effective densities of states for the conduction and valence bands, respectively. The Fermi integral of order one-half $F\,{}^{1}\!/_{2}$ in equation (3.2) and (3.3) is defined as

$$F\,{}^{1}\!/_{2}\ (\eta) = \frac{2}{\sqrt{\pi}} \int_0^{\infty} \frac{E^{1/2}\, dE}{1 + \exp(E - \eta)} \tag{3.4}$$

Where the Fermi integral argument η is expressed as

$$\eta_n = \left(\frac{E_F - E_C}{kT}\right) \tag{3.5}$$

for free electrons and for free holes.

$$\eta_p = \left(\frac{E_V - E_F}{kT}\right) \tag{3.6}$$

The total charge arising in localized doping levels which includes gap states can be represented by

$$N_D^+ = N_{dD}^+ + N_{bD}^+ \tag{3.7}$$

for the donor-dopant levels and

$$N_A^- = N_{dA}^- + N_{bA}^- \tag{3.8}$$

for the acceptor-dopant levels. It should be note that, hereN_D^+ and N_A^- which can be seen in Poisson's equation (equation 3.1), are the total charge arising from both the discrete and band dopant energy levels. In these equations, N_{dD}^+ and N_{bD}^+ resents the total charge originating from discrete donor and acceptor concentrations, respectively, whereas N_{dA}^- and N_{bA}^- represents the total charge developed by any banded donor and acceptor levels, respectively. The total charge arising in defect levels can be expressed as

$$p_t = p_{dt} + p_{bt} + p_{ct} \tag{3.9}$$

for the donor-like states and,

$$n_t = n_{dt} + n_{bt} + n_{ct} \tag{3.10}$$

for the acceptor-like state. Here, and which can be seen in Poisson's equation (equation 3.1) are the total charge arising from the discrete, banded, and continuous defect (structural or impurity) energy levels. In these equations, and represent the total charge originating respectively from discrete acceptor and donor concentrations, while and represent the total charge originating respectively from discrete acceptor and donor concentrations. Finally, and represent the total charge developed by any continuous, e.g. exponential, Gaussian, or constant, acceptor and donor concentrations, respectively. The formulas (Equations (3.1) to (3.10)) above express all the quantities contributing to the charge in Poisson's equation. A close inspection of these expressions shows that they all are ultimately defined in terms of the free carrier populations *n* and *p*. More information on *n* and *p* is required to determine how they change across a device and under different biases. The equations that keep track of the conduction band electrons and valence band holes are the continuity equations. In steady state, the time rate of change of free carrier concentrations is equal to zero. As a result, the continuity equation for the free electrons in the delocalized states of the conduction band has a form as

$$\frac{1}{q}\left(\frac{djn}{dx}\right) = -G_{op}(x) + R(x) \tag{3.11}$$

and the continuity equation for the free hole in the localized state of the valence band has a form as

$$\frac{1}{q}\left(\frac{djp}{dx}\right) = -G_{op}(x) + R(x) \tag{3.12}$$

J_n and J_p are the electron and hole current densities, respectively. The term *R(x)* is the net recombination rate resulting from band-to-band (direct) recombination and S-R-H (indirect) recombination traffic through gap states. The term $G_{op}(x)$ is the optical generation rate resulting from the externally imposed illumination. From equation 3.11 and 3.12, the electron current density J_n can be expressed as

$$J_n(x) = q\mu_n n\left(\frac{dEf_n}{dx}\right) \tag{3.13}$$

where μ_n is the electron mobility and n is defined in equation 5.2. Similarly, he hole current density J_p can be given by

$$J_p(x) = q\mu_p p\left(\frac{dEf_p}{dx}\right) \tag{3.14}$$

where μ_p is the electron mobility and p is defined in equation 3.14. Electron and hole may recombine with each other by two basic processes. In the first process, electrons in the conduction band make direct transitions to vacant state in the valence band. This process is call band-to-band or *''direct recombination''* R_D, which is also known as intrinsic recombination. In the second process, electron and holes recombine through intermediate gap states known as recombination centers. This process, originally investigated by Shockley, Read and Hall, is called *''indirect recombination''* R_I or R-S-H recombination, which is also known as extrinsic recombination. The net recombination term $R(x)$ in the continuity equations takes both of these processes into consideration such that

$$R(x) = R_D(x) + R_1(x) \quad (3.15)$$

The net direct recombination rate can be expressed as

$$R_D(x) = \beta(np - n_0p_0) = \beta(np - n_i^2) \quad (3.16)$$

Here, β is a proportionality constant which depends on the energy-band structure of the material under analysis, and n and p are the band carrier concentrations present when devices are subjected to a voltage bias, light bias or both, n_0 and p_0 factors are the carrier concentrations in thermodynamic equilibrium expressed.

The S-R-H net recombination can be expressed by

$$R_1(x) = \frac{np - n_{i2}}{\tau_{p0}(n+n_t)+\tau_{n0}(p+p_t)} \quad (3.17)$$

Here, $\tau p0$ and $\tau n0$ are the reciprocals of the thermal velocity-hole/electron capture cross section and N_t product. The quantities n_t and p_t depend exponentially on the position of the defects in the energy bandgap.

In this simulation program, it is assumed that a structure illuminated by a light source of frequency v_i with a photon flux of $\Phi_{oi}(v_i)$ (in units of photons per unit area per unit time) has photos obeying $hv \geq E_{opt}$. This photon flux $\Phi_{oi}(v_i)$ is impinging at $x = 0$. As the photon flux travels through the structure, the rate at which electron-hole pairs are generated is proportional to the rate at which the photo flux decreases. Therefore, the optical generation rate can be expressed as

$$G_{op}(\mathrm{x}) = -\frac{d}{dx}\sum_i \phi_i^{FOR}(v_i) + \frac{d}{dx}\sum_i \phi_i^{REV}\,(v_i) \qquad (3.18)$$

where $\phi_i^{FOR}(v_i)$ represents the photon flux of frequency v_i at some point x which is moving left to right (forward) and $\phi_i^{REV}(v_i)$ represents the photon flux of frequency v_i at some point x which is moving right to left (reverse). If a device has optical properties that do not vary across the structure, then at some general point x we have

$$\Phi_i^{FOR}(v_i) = \Phi_i^{FOR}(v_i)\cdot\left\{\exp[-\alpha(v_i)x] + R_F R_B[\exp(-\alpha(v_i)L]^2 \cdot \exp[-\alpha(v_i)x]\right\} \qquad (3.19)$$

Whereas

$$\Phi_i^{FOR}(v_i) =$$
$$R_B\phi_{oi}(v_i)\cdot\{\exp[-\alpha(v_i)L]\exp[-\alpha(v_i)\,(L-x)] + R_F R_B\ [\exp\,(-\alpha(v_i)(L-$$
$$x)3exp - avi(L-x) + \cdots \qquad (3.20)$$

In these expressions, R_F is the reflection coefficient for the internal surface at x = 0 and R_B is the reflection coefficient for the internal surface at x =L (the back surface). All of these reflect coefficients can functions of the frequency v_i. AMPS-1D also provided the possibility to consider Gaussian states that are either donor-line or acceptor like, located anywhere in the bandgap. The acceptor like g_A and the donor like g_D band tail states are respectively expressed as

$$g_A(\mathrm{E}) = g_{A0} \cdot exp\{-(E_c - E)/E_A\} \tag{3.21}$$

$$g_D(\mathrm{E}) = g_{D0} \cdot exp\{-(E - E_c)/E_A\} \tag{3.22}$$

The acceptor like and donor-like Gaussian dangling bond states are, respectively expressed as

$$g_{AG}(\mathrm{E}) = \left(\frac{N_{AG}}{\sqrt{2\pi\sigma_{AG}^2}}\right) \cdot exp\left(-\frac{(E-E_{AG})^2}{2\sigma_{AG}^2}\right) \tag{3.23}$$

$$g_{DG}(\mathrm{E}) = \left(\frac{N_{DG}}{\sqrt{2\pi\sigma_{DG}^2}}\right) \cdot exp\left(-\frac{(E-E_{DG})^2}{2\sigma_{DG}^2}\right) \tag{3.24}$$

Where σ_{AG} and σ_{AG} are the standard deviations if the acceptor-like and donor-like Gaussian dangling bond states, respectively.

3.3 Theoretical Analysis of Thin film solar cells

Before studying of spectrum splitting simulation, basic of a-Si:H and CIGS solar cells' performance are studied. In this simulation study, both of solar cells have thousands of variable parameters as well as the splitting structure simulation. Among them, main parameters are considered to be the splitting wavelength (I_{sp}), which is the exact number of wavelength that divides the solar spectrum into two parts or more, and bandgap and thickness of absorber materials. The model of the solar cell structure assumes a p-i-n superstrate structure which is the front electrode/ p-type hydrogenated amorphous silicon carbide (a-SiC:H)/ intrinsic a-Si:H/ n-type μc-SiO:H/ back electrode. The electrical and optical parameters were taken from experimental results and some literature [20-30] for each layer are listed I table 3.1. For this model, abovementioned continuous density of state was employed within the mobility gap. The Gaussian defect density of i-layer was assumed to be 2 x 10^{15} cm^{-3}. The thickness of the i-layer was 300nm and the doped layer were 15 nm as a standard model based on the experimental results. As optical parameters, we have used the optical constant of p-a-SiC:H, i-a-Si:H, and n-μc-SiO:H layers obtained from measurement results. In this calculation, light trapping effect was not considered. It was assumed that there is no reflection for light impinging on front surfaces and the back contact (Ag) has a reflection coefficient of 0.9.It was also assumed that the band gap discontinuity at the p-a-SiC:H/i-a-Si:H heterointerface was assigned in equal proportions to the valence and conduction badns. For CIGS bottom cell, the material parameters were referred to a literature [28]

Table 3.1 Simulation parameter of a-Si:H solar cell model

Parameter [unit]	**p-a-SiC:H**	**i-a-Si:H**	**n-a-Si:H**
Thickness [nm]	15	200~500	15
Mobility gap [eV]	1.7~2.2	1.5~2.0	1.5~2.0
Optical gap [eV]	1.7~2.2	1.5~2.0	1.5~2.0
Electron affinity [eV]	3.9	4	4
Relative permittivity	11.9	11.9	11.9
Mobility μ_n / μ_p [$cm^2/(Vs)$]	2/0.2	20/2	20/2
Acceptor Concentration [cm^{-3}]	5×10^{18}	0	0
Donor Concentration [cm^{-3}]	0	0	1×10^{19}
Effective DOS in Conduction band N_c [cm^{-3}]	1×10^{20}	1×10^{20}	1×10^{20}
Effective DOS in Valence band N_v[cm^{-3}]	1×10^{20}	1×10^{20}	1×10^{20}
D states parameter			
E_{DG}/E_{AG} [eV]	0.6/0.6	1.07~1.43/1.07~1.43	0.6/0.6
$_{DG}$ / $_{AG}$ [eV]	0.13/0.13	0.13/0.13	0.13/0.13
Donor-like dangling bond states			
Capture cross section for electron [cm^2]	1×10^{-14}	1×10^{-14}	1×10^{-14}
Capture cross section for hole [cm^2]	1×10^{-15}	1×10^{-15}	1×10^{-15}
Acceptor-like dangling bond states			
Capture cross section for electron [cm^2]	1×10^{-15}	1×10^{-15}	1×10^{-15}
Capture cross section for hole [cm^2]	1×10^{-14}	1×10^{-14}	1×10^{-14}
Valence band tail states			
Capture cross section for electron [cm^2]	1×10^{-15}	1×10^{-15}	1×10^{-15}
Capture cross section for hole [cm^2]	1×10^{-16}	1×10^{-16}	1×10^{-16}
Conduction band tail states			
Capture cross section for electron [cm^2]	1×10^{-16}	1×10^{-16}	1×10^{-16}
Capture cross section for hole [cm^2]	1×10^{-15}	1×10^{-15}	1×10^{-15}

Table 3.2 Simulation parameter of CIGS solar cell model

Parameter [unit]	**n-ZnO:B**	**i-ZnO**	**n-CdS**	**p-CIGS**
Thickness [nm]	1000	90	50	1000~3000
Mobility gap [eV]	3.3	3.3	2.4	1.0~1.4
Optical gap [eV]	3.3	3.3	2.4	1.0~1.4
Electron affinity [eV]	4.5	4.5	3.75	3.85~4.25
Relative permittivity	9	9	10	13.6
Mobility μ_n / μ_p [cm^2/(Vs)]	100/25	100/25	100/25	100/25
Acceptor Concentration [cm^{-3}]	0	0	0	2.01×10^{16}
Donor Concentration [cm^{-3}]	5.7×10^{18}	5×10^{16}	2.1×10^{18}	0
Effective DOS in Conduction band N_c [cm^{-3}]	2.22×10^{18}	2.22×10^{18}	2.22×10^{18}	2.22×10^{18}
Effective DOS in Valence band N_v[cm^{-3}]	1.78×10^{19}	1.78×10^{19}	1.78×10^{19}	1.78×10^{19}
Donor-like dangling bond states				
Capture cross section for electron [cm^2]	1.21×10^{-12}	1.2×10^{-12}	9.8×10^{-13}	5.3×10^{-13}
Capture cross section for hole [cm^2]	1×10^{-17}	1×10^{-17}	1×10^{-17}	1×10^{-18}
Acceptor-like dangling bond states				
Capture cross section for electron [cm^2]	1×10^{-17}	1×10^{-17}	1×10^{-17}	1×10^{-18}
Capture cross section for hole [cm^2]	1×10^{-12}	1×10^{-12}	9.8×10^{-13}	1×10^{-13}
Tail states parameter				
E_{DG}/E_{AG} [eV]	0.01/0.01	0.01/0.01	0.01/0.01	0.01/0.01
$_{DG}$ / $_{G}$ [eV]	2×10^{20}/ 2×10^{20}	2×10^{20}/ 2×10^{20}	2×10^{20}/ 2×10^{20}	1×10^{18}/ 1×10^{18}
Donor-like dangling bond states				
Capture cross section for electron [cm^2]	1×10^{-15}	1×10^{-15}	1×10^{-15}	1×10^{-15}
Capture cross section for hole [cm^2]	1×10^{-17}	1×10^{-17}	1×10^{-17}	1×10^{-17}
Acceptor-like dangling bond states				
Capture cross section for electron [cm^2]	1×10^{-17}	1×10^{-17}	1×10^{-17}	1×10^{-17}
Capture cross section for hole [cm^2]	1×10^{-15}	1×10^{-15}	1×10^{-15}	1×10^{-15}

Table 3.3 Parameters for electrode interface

Parameter [unit]	Top cell	Bottom cell
Front Contact		
$_{b0}=E_C-E_F$ at x=0 (Surface) [eV]	1.05~1.55	0.00
Surface Electron recombination at x=0 [cm/s]	1.00×10^7	1.00×10^7
Surface hole recombination at x=0 [cm/s]	1.00×10^7	1.00×10^7
Reflection coefficient	0	0.03
Back contact		
$_{bL}=E_C-E_F$ at x=L (Surface) [eV]	0.10	0.90
Surface Electron recombination at x=L [cm/s]	1.00×10^7	1.00×10^7
Surface hole recombination at x=L [cm/s]	1.00×10^7	1.00×10^7
Reflection coefficient	0.9	0.9

3.3.1 Dependence of Intrinsic-layer thickness and optical band gap for a-Si:H solar cell

Figure 3.1 shows the simulation results of a-Si:H solar cell performance as a function of intrinsic absorber layers' thickness and optical band gap. From the results, as increasing optical band gap, short-circuit current (J_{sc}) has decreased, open-circuit voltage (V_{oc}) and fill factor (*FF*) has increased. As increasing band gap, optical band gap, the number of excited photon has been increasing because it has transmitted not absorbed. Also in wider band gap, internal electrical field has been increasing so recombination rate is declined. So that reversed saturation current is lower, V_{oc} would be increasing. So, when band gap is become wider, V_{oc} is increasing. Then thickness dependence simulation results will be introduced. As seen in fig.3.1, short circuit current (J_{sc}) is increased. When the absorber layer thickness is thicker, light has been absorbed effectively. On the other hand, as increasing thickness of intrinsic layer, open circuit voltage (V_{oc}) slightly decreased and fill factor (*FF*) quite bigger drop. The reason of this drop tendency might be assumed that when intrinsic thickness is thicker while band gap maintained constantly, the internal electric field which insides in intrinsic layer are weak and the rate of recombination is increasing. So the intrinsic layer thickness will be deeply related quality of intrinsic layer.

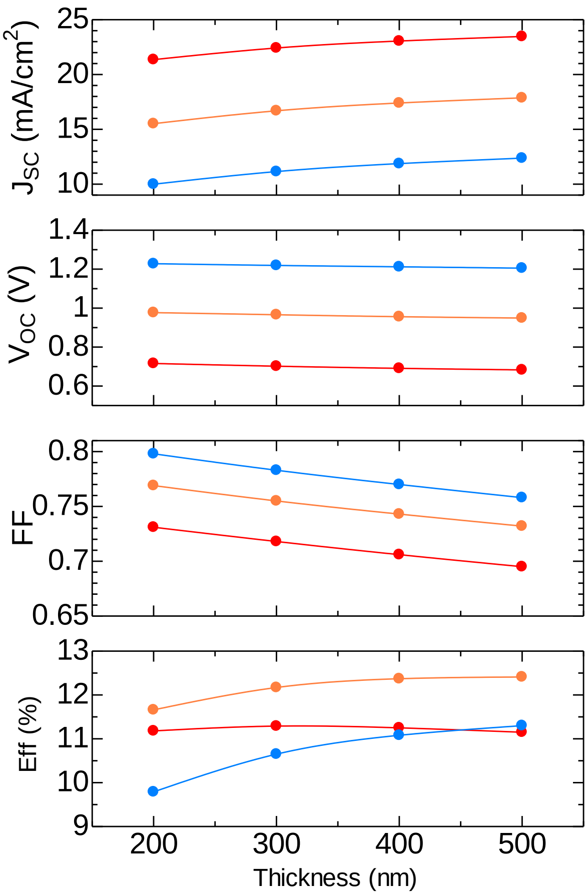

Figure 3.1 a-Si:H solar cell performance with various intrinsic absorber thickness (nm) and optical band gap (eV)

3.3.2 Dependence of Intrinsic-layer thickness and optical band gap for CIGS solar cell

Figure 3.2 shows CIGS solar cell performance with various band gap and absorber layer thickness. First, band gap dependence of solar cell performances is considering. Similar to a-Si:H solar cell performance, short-circuit current is decreased, otherwise open-circuit voltage and fill factor are increased as increasing band gap. However for fill factor, when band gap E_g = 1.4 eV calculated lower fill factor value when band gap E_g = 1.3 eV. Also increasing of absorber layer thickness, short-circuit current and open-circuit voltage are slightly increasing, but fill factor has been dropped. So as same as a-Si:H solar cell calculation, thickness of absorber layer is depended on quality of absorber layer. In figure 3.3, 3.4, and 3.5 shows band diagram, internal electric field, the rate of recombination/the rate of generation distribution when band gap E_g = 1.2 eV with different absorber layer thickness. In figure 3.3, band diagram do not change even though absorber layer thickness has changed. But, in figure.3.4 internal electric field became weaker while band gap has kept constantly. Further area from pn junction has generated photo excited electron-hole pair collection and it has affected. So that the reason of fill factor decreasing could be considered that electron-hole pair generation rate (soled line) has smaller than recombination rate (dot line) in figure 3.5

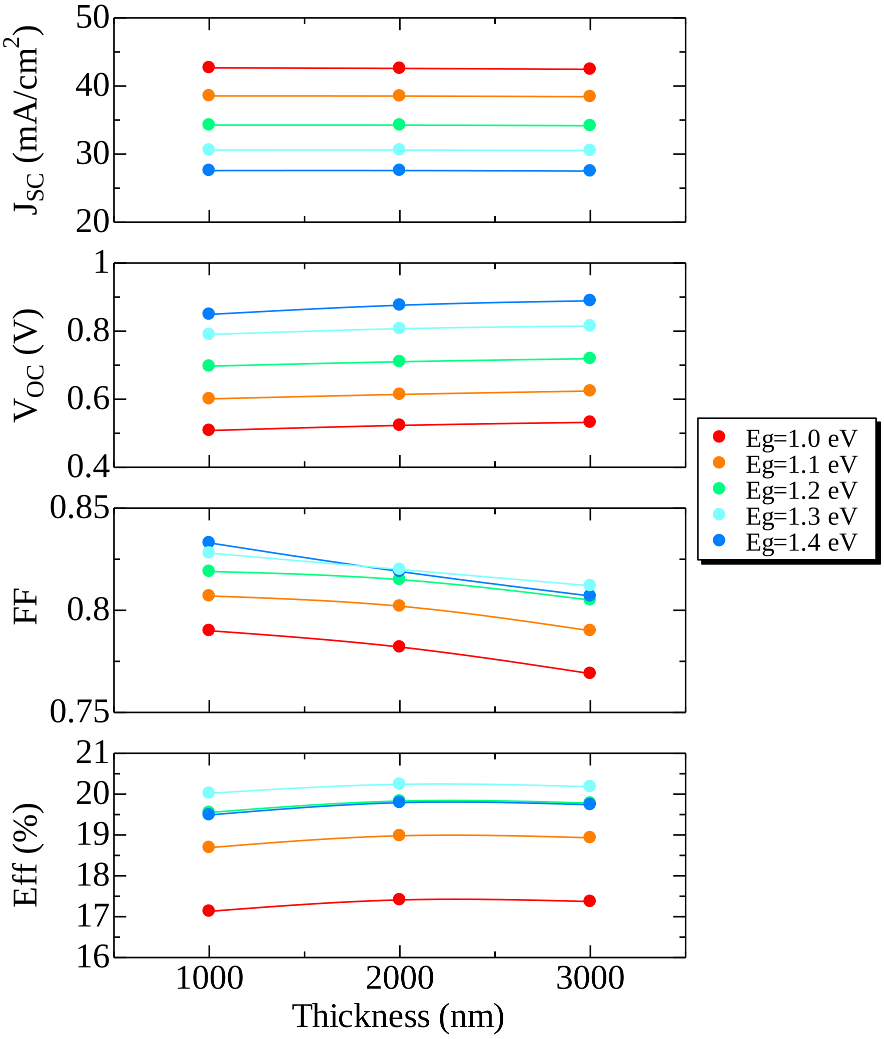

Figure 3.2 CIGS Solar cell performance with various intrinsic absorber thickness (nm) and optical band gap (eV)

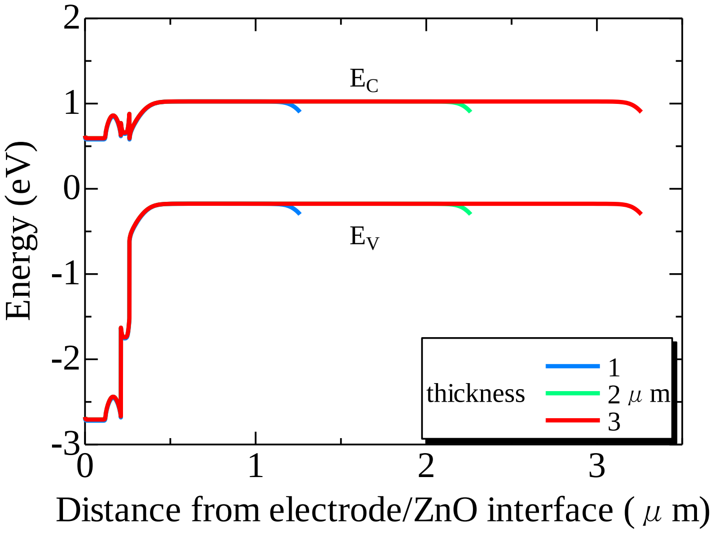

Figure 3.3 Band diagram dependence by absorber layer thickness

(Illuminated, Applied Voltage=V_{max})

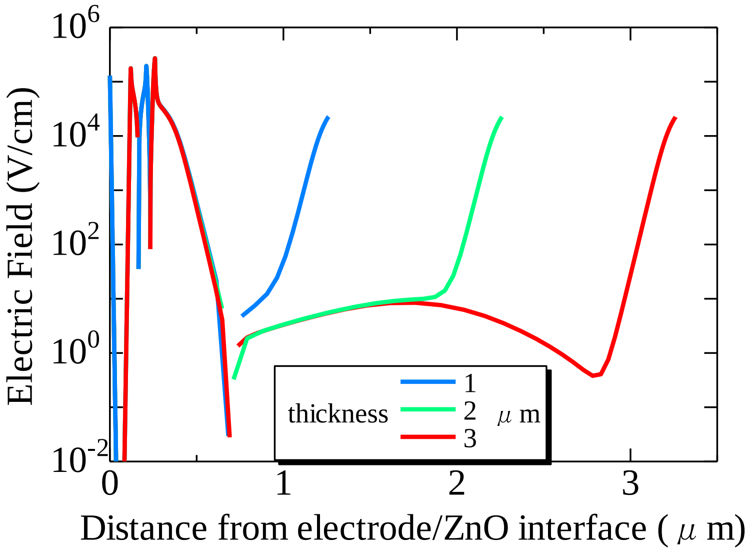

Figure 3.4 Internal electric filed diagram depended by absorber layer thickness

(Illuminated, Applied Voltage=V_{max})

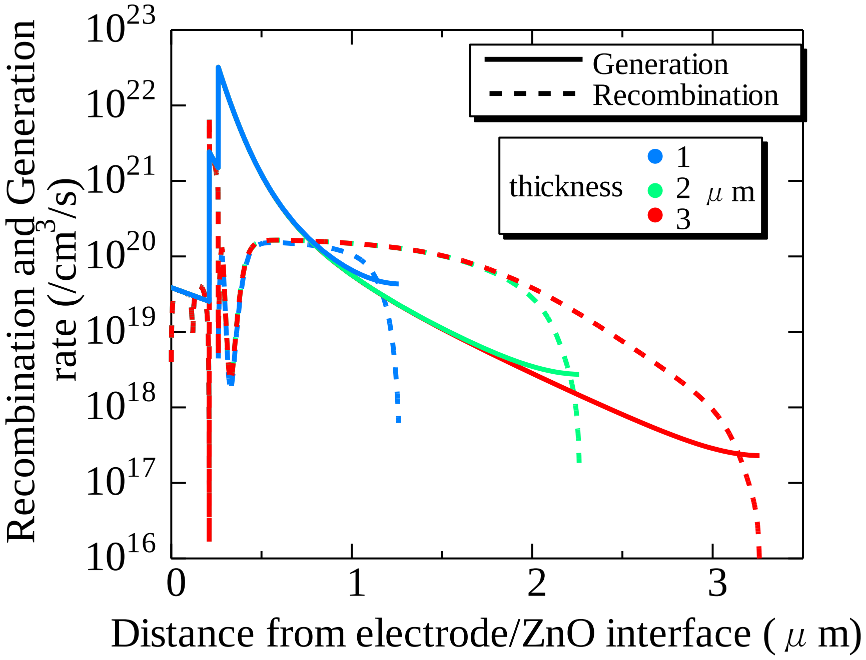

Figure. 3.5 Recombination/generation rate dependency by thickness of absorber layer

soled line indicated generation rate and dot line indicated recombination rate

(Illuminated, Applied Voltage=V_{max})

Table 3.4 The simulation solar cell performance for a-Si:H

E_g (eV)	**Thickness (nm)**	**J_{SC} (mA/cm^2)**	**V_{OC} (V)**	**FF**	**Eff (%)**
1.5	300	22.42	0.702	0.718	11.29
1.75	500	17.87	0.949	0.732	12.41
2.0	500	12.37	1.205	0.758	11.30

Table 3.5 The simulation solar cell performance for CIGS

E_g (eV)	**Thickness (nm)**	**J_{SC} (mA/cm^2)**	**V_{OC} (V)**	**FF**	**Eff (%)**
1.0	2000	42.58	0.523	0.782	17.41
1.1	2000	38.52	0.614	0.802	18.98
1.2	2000	34.25	0.710	0.815	19.83
1.3	2000	30.59	0.820	0.807	20.24
1.4	2000	27.58	0.876	0.819	19.79

In case of a-Si:H and CIGS solar cell, theoretical analysis solar cell performance shows table 3.4 and 3.5. In case of a-Si:H solar cell results shows that absorbed photons are increased when band gap is narrow, so thinner intrinsic absorber layer would be fine with a-Si:H solar cell. Also in case of CIGS sola cell results, the best thickness is 2000nm with all range of absorber layer band gap.

3.4 Theoretical Analysis of Thin film solar cells with Full spectrum splitting technique

Now we are ready to analysis about solar cell performance with spectrum splitting technique. Previous section, we calculated the best of both soar cell under various parameters. So now, the spectrum splitting solar cells performance was theoretically demonstrated. Therefore, in this study, the splitting wavelength was varied from 500 to 800 nm as a main parameter. For the calculation, the solar irradiance spectra were simply divided into two parts at I_{sp} in the photon flux input files, and those in the short wavelength regions were used for the calculation of a-Si:H top cell and the rest for CIGS bottom cell.

Table 3.6 Incident conversion wavelength range to top and bottom cell

Conversion wavelength (nm)	510	610	710	810
wavelength range to top cell	380~500	380~600	380~700	380~800
wavelength range to Bottom cell	520~1240	620~1240	720~1240	820~1240

First, incident wavelength property has been studied when the light has been split. From the simulation AMPS-1D is able to change photon flux of incident wavelength 380nm to 1240nm, so the range of incident wavelength has changed as presented in Table 3.6,

3.4.1 Simulation results of amorphous silicon solar cell by Spectrum splitting

Figure 3.6 shows the simulation results of top solar cell performance under various splitting wavelength and band gaps of active layers. As can be seen from these figures, the Jsc of both cells strongly depend on the splitting wavelength. Short-circuit current has increased when splitting wavelength goes to long wavelength region. But Jsc increased at splitting wavelength 600nm then above 600nm, short-circuit current kept constantly when band gap Eg=2.0eV. Also when band gap Eg=1.5eV, the short-circuit current kept increasing. This tendency related absorbed photon energy and intrinsic optical band gap. For detail, in case if wide band gap (Eg=2.0eV) shows constantly short-circuit current values above splitting wavelength 600nm because absorb range has around 600nm, so incident light wavelength region has increased to long wavelength. So the short-circuit current has kept constantly at certain range of wavelength. On the other hands, open-circuit voltage indicates almost same value at all splitting wavelength region.

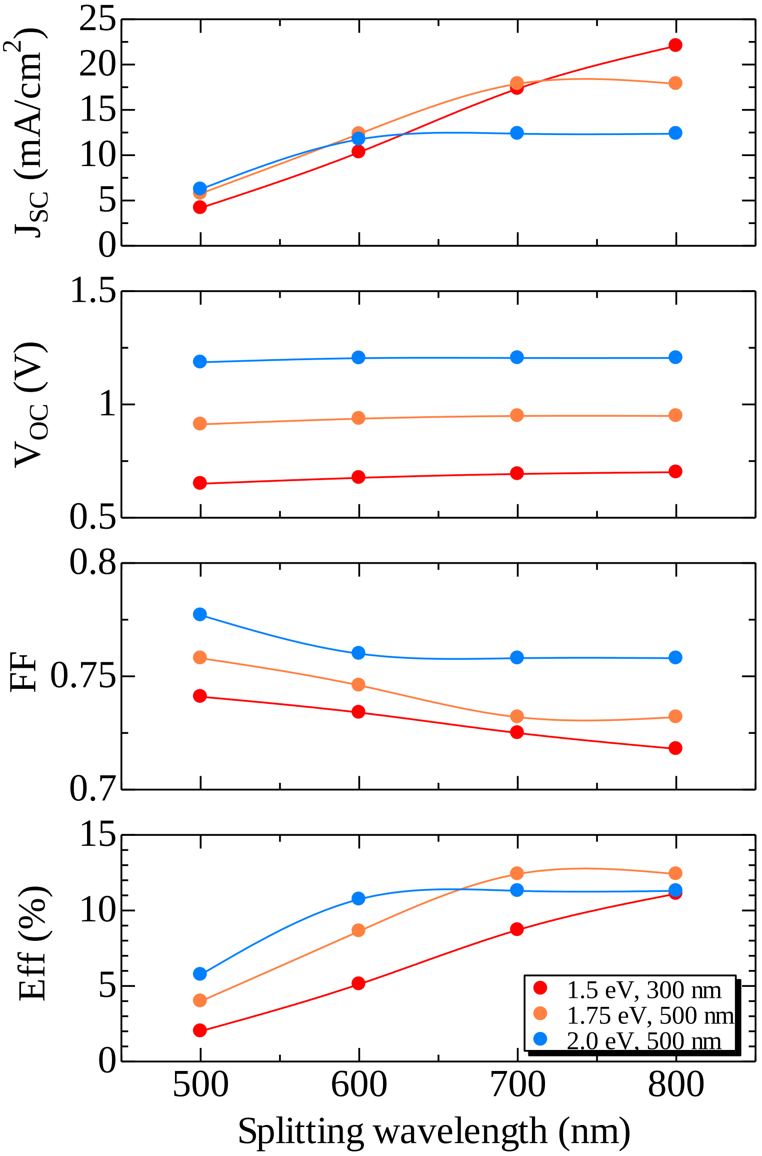

Figure 3.6 Simulation results of (a) a-Si:H top cells of spectrum splitting configuration as a function of bandgaps and splitting wavelengths.

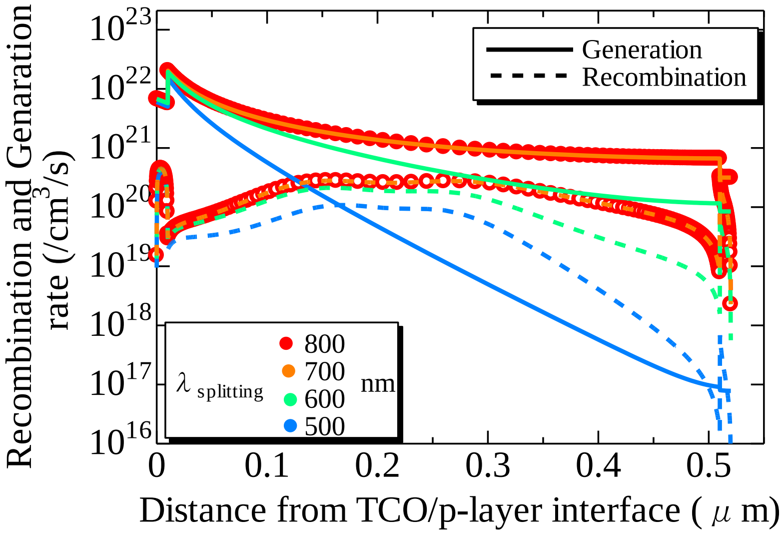

Figure 3.7 Recombination/generation rate dependency by various spectrum splitting wavelength soled line indicated generation rate and dot line indicated recombination rate

(Illuminated, Applied Voltage=V_{max})

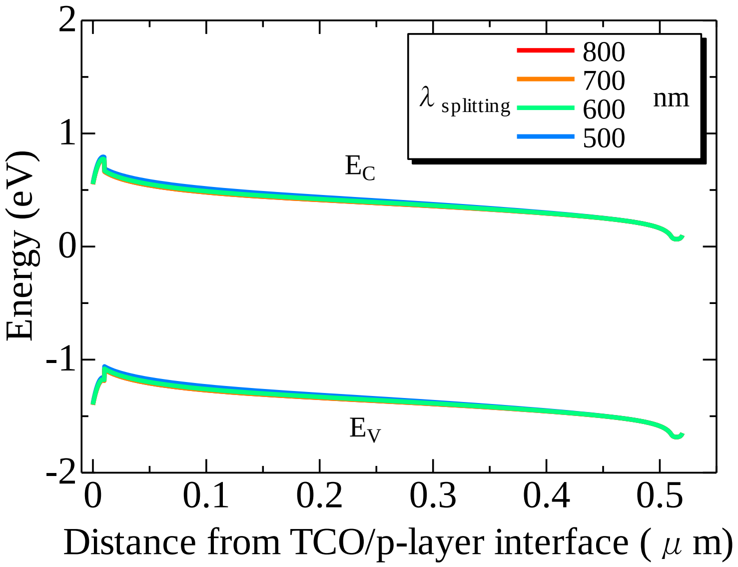

Figure 3.8 Band diagram dependence by various spectrum splitting wavelength

(Illuminated, Applied Voltage=V_{max})

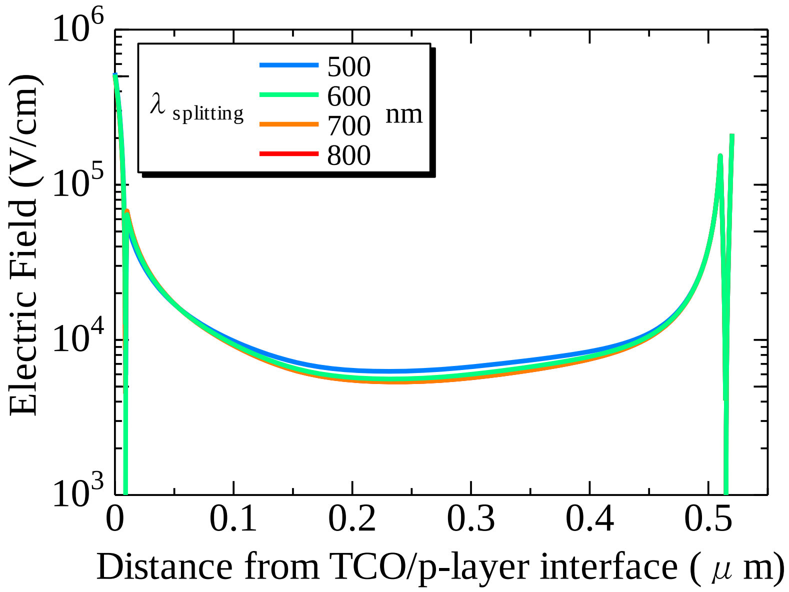

Figure 3.9 Internal electric filed diagram depended by various spectrum splitting wavelength

(Illuminated, Applied Voltage=V_{max})

For fill factor (FF) shows top and bottom revered formation by short-circuit current graph. In figure 3.7 represented recombination/generation rate in order to find the reason. When band gap Eg=1.75eV, and thickness 500nm, the recombination/generation rate and electrical field distribution depended by splitting wavelength has been studied in figure 3.8 and 3.9. At this point, the applied voltage has maximum point. Otherwise, the detailed band diagram and internal electric field depended by various spectrum splitting wavelength has been studied. From the figure 3.8, as longer splitting wavelength region, generated photon carrier has been increased. As like this, in intrinsic layer, the recombination rate also increased. However, absorber layer band gap is

E_g=1.75eV at 710nm, even though the splitting wavelength has been longer, other change has not confirmed. As change of splitting wavelength, the generated photons are increased, therefore as confirmed from band diagram and internal electric field figure, intrinsic layer electric field has been weaker so it might explain decrease of fill factor loss.

.

3.4.2 Simulation results of CIGS solar cell by Spectrum splitting

Figure 3.10 shows bottom solar cell performance under the various thickness and band gap. As placed longer splitting wavelength, the short-circuit current has been increased because of when the splitting wavelength increased, absorbed photons are increased as well. also the open circuit voltage has slightly increased and the fill factor has quite increased. As the wider band gap, fill factor also has increased. No matter the results of short circuit current and open circuit voltage and fill factor, the conversion efficiency has increased when the splitting wavelength has moved short wavelength region. In order to study of fill factor decreased, the generation/recombination rate inside has been studied. In figure 3.11, shows the relationship with recombination rate when the band gap Eg=1.1eV and the splitting wavelength. As same like top cell simulation results, the applied voltage has maximum point. Also figure 3.12 and 3.13 shows band diagram and electric filed. At splitting longer wavelength, numbers of absorbed photons are decreased then recombination rate also decreased by back side of electrode. There for, in figure 3.13 shows the back side of electrode shows weak internal electric field, so it could be considering that the reason why fill factor decreased is the generation and recombination rate has huge decreased. Also in case of CIGS solar cell, the incident light spectrum limited at longer wavelength, CdS layer has not absorbed sufficient photon, so ZnO / CdS (buffer) / CIGS interface band change has small, the barrier become high level by electron, so open circuit volatage and fill factor also decreased [31].

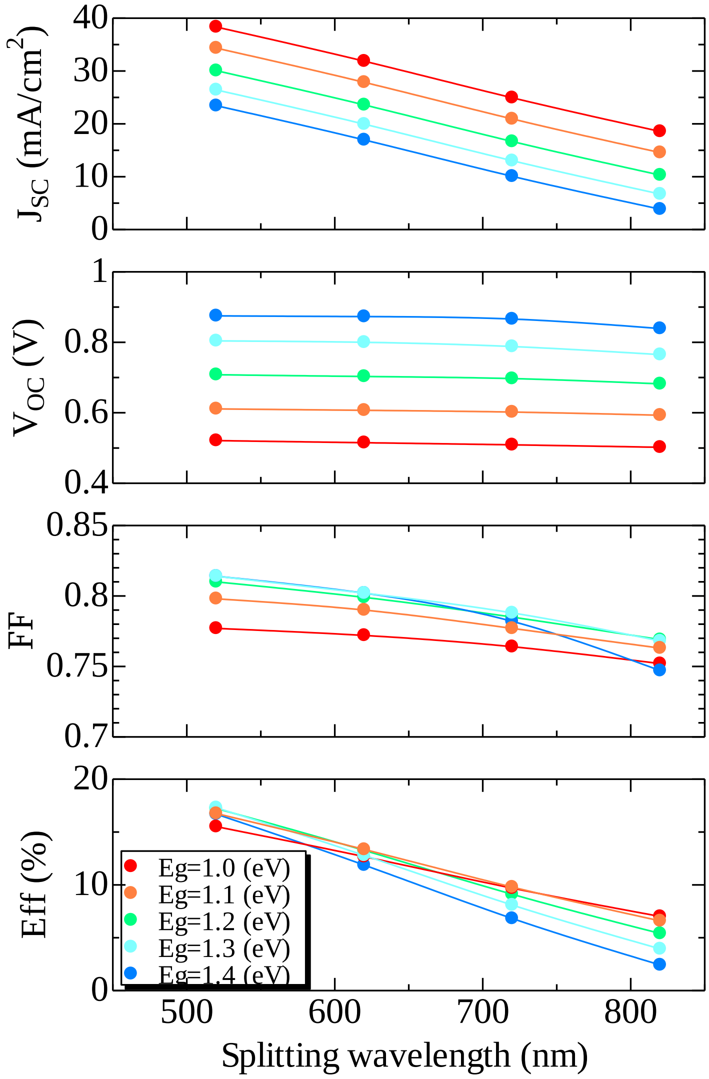

Figure 3.10 Simulation results of (a) a-Si:H top cells of spectrum splitting configuration as a function of bandgaps and splitting wavelengths.

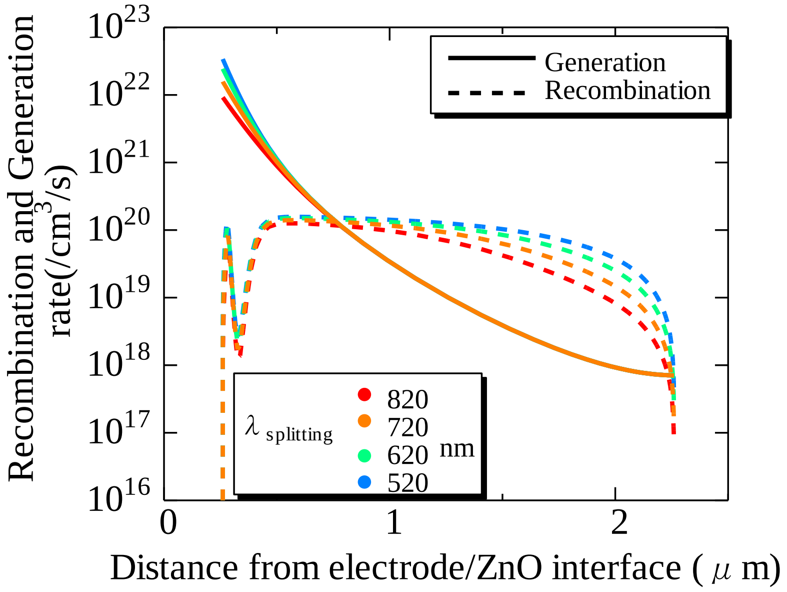

Figure 3.11 Recombination/generation rate dependency by various spectrum splitting wavelength soled line indicated generation rate and dot line indicated recombination rate

(Illuminated, Applied Voltage=V_{max})

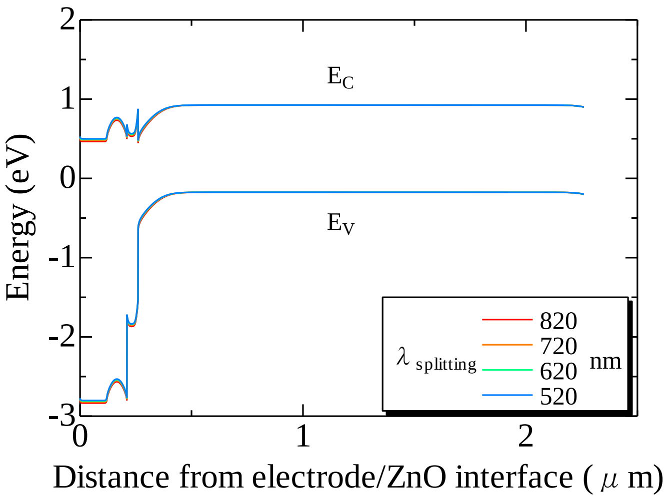

Figure 3.12 Band diagram dependence by various spectrum splitting wavelength

(Illuminated, Applied Voltage=V_{max})

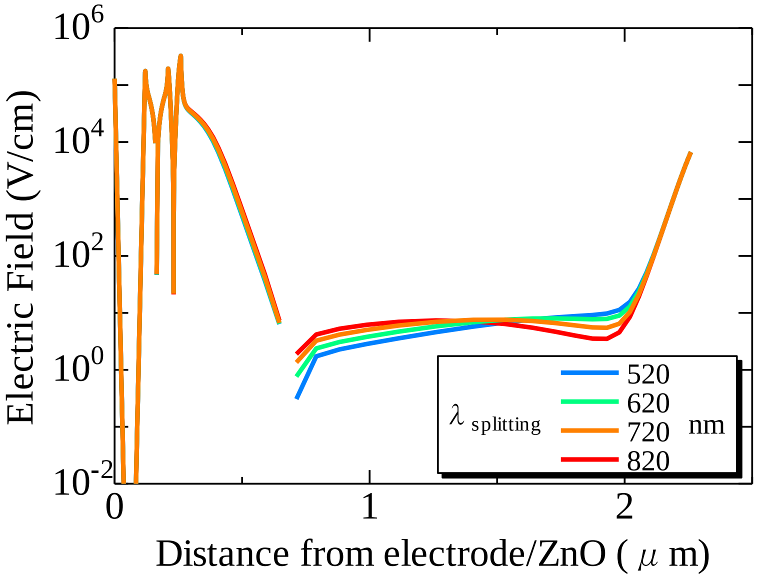

Figure 3.13 Internal electric filed diagram depended by various spectrum splitting wavelength

(Illuminated, Applied Voltage=V_{max})

Figure 3.14 shows the simulated total efficiency of the solar cell performance in figure 3.15. This is the case that E_g and thickness of a-Si:H was 2.0 eV and 500 nm, and E_g of CIGS was 1.1 eV. The total efficiency which combines top cell with wider band gap achieved higher total efficiency. It should be noted here that it is possible to obtain the total efficiency of as high as 24.1% at the splitting wavelength of 600 nm. The best photovoltaic parameters are listed in table.3.7 It was observed that the total J_{sc} of both cells are higher than that of stand-alone bottom cell. It means that splitting technique is much promising to use the spectrum efficiently.

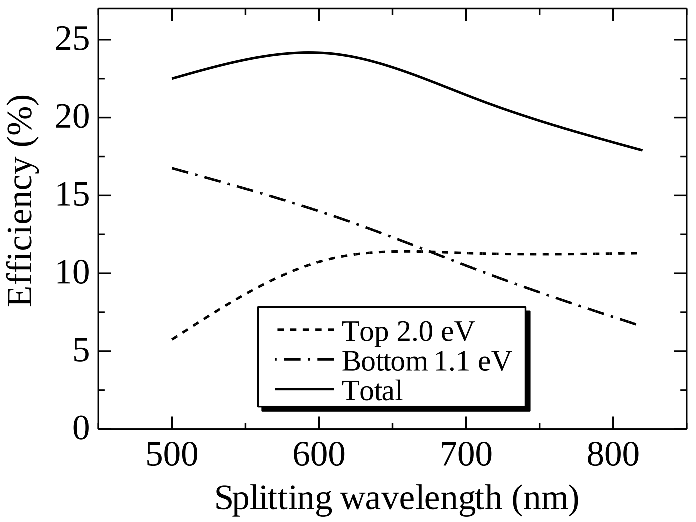

Figure3.14 Calculated total conversion efficiency of spectrum splitting solar cells as a function of splitting wavelength.

Table.3.7 Calculated photovoltaic parameters of spectrum splitting solar cells with a-Si:H top and CIGS bottom cells.

Cell	V_{oc} (V)	J_{sc} (mA/cm^2)	FF	Eff. (%)
Top	1.20	11.7	0.760	10.7
Bottom	0.607	27.9	0.790	13.4
Total	—	—	—	24.1
Stand-alone a-Si:H	1.21	12.4	0.758	11.30
Stand-alone CIGS	0.614	38.5	0.802	19.0

3.4 Summary

In this chapter, the theoretical analysis of a-Si:H and CIGS solar cells parameter in order to find best solar cell condition for spectrum splitting. Then we found for the a-Si:H solar cell when the band gap is Eg=1.75eV and the thickness 500nm, for CIGS solar cell when the band gap 1.3eV and the thickness 2000nm have best calculated solar cell performance (a-Si:H =12.41% and CIGS=20.29%). Then using this solar cell parameter, we studied about splitting wavelength dependence with various band gap for each cell. From these results, we finally got 24.1% simulation results when the splitting wavelength is 614nm.

REFERENCES

[1] F. Meillaud, A. Shah, C. Droz, E. V-Sauvain, and C. Miazza: Sol. Energy Mater. Sol.Cells 90 (2006) 2952.

[2] A.Marti and G. L. Araujo, Sol. Energy Mater. Sol. Cells 43 (1996) 203.

[3] H. Takakura: Jpn. J. Appl. Phys. 31 (1992) 2394.

[4] H. Zu, A. K. Kalkan, J. Hou, and S. J. Fonash: AIP Conf. Proc. 462 (1999) 309.

[5] A. V. Shah, M. Vanecek, J. Meir, F. Meillaud, Guillet, D. Fischer, C. Droz, X. Niquille, S. Fay, E. V-Sauvain, V. T-Daudrix, and J. Bailat: J. Non-Cryst. Sol. 338 (2004) 639.

[6] A. H. Pawlikiewicz and S. Guha: Proceeding in 20th IEEE Photovoltaic Specialists Conf. Las Vegas, NV, USA, (1988) 251.

[7] A. H. Pawlikiewicz and S. Guha: IEEE Trans, Electron Devices 37 (1990) 1758.

[8] M. Block, D. Bonnet, F. Zetzsche: Proceeding in 20th IEEE Photovoltaic Specialists Conf. Las Vegas, NV, USA, (1991) 1275.

[9] Pennsylvania State University, “AMPS” http://www.cneu.psu.edu/amps/about.html

[10] J. Arch, J. Hou, W. Howland, P. McElheny, A. Moquin, M. Rogosky, F. Rubinelli, T.Tran, H. Zhu, and J. Fonash, “A Manual for AMPS-1D for Windows ‘95/NT Beta Version 1.00”, The Pennsylvania State University (1997).

[11] M. Burgelman, J. Verschraegen, S. Degrave and P. Nollet : Progress in Photovoltaics 12 (2004) 143.

[12] H. Zhu, A. K. Kalkan, J. Hou, and S.J. Fonash: AIP Conf. Proc. 462 (1999) 309.

“Applications of AMPS-1D for solar cell simulation”

[13] K. Dairiki, A. Yamada, and M. Konagai: Jpn. J. Appl. Phys. 40 (2001) 486. “Numerical Analysis to Improve the Stabilized-Efficiency of Amorphous Silicon Solar Cells with New Device Structure”

[14] H. Tasaki, W. Y. Kim, M. Hallerdt, M. Konagai, and K. Takahashi: J. Appl. Phys. 63(1988) 550.“Computer simulation model of the effects of interface states on high- performance amorphous silicon solar cells”

[15] T. Tiedje, J. M. Cebulka, D. L. Morel, and B. Abeles: Phys. Rev. Lett. 46 (1981) 1425.

[16] H. Okamoto, K. Hattori and Y. Hamakawa: J. Non-Cryst. Solids 137&138 (1985) 627.

[17] C.R.Wronski : Sol. Energy Mater. 1 (1979) 287.

[18] K. Itoh, H. Matsumoto, T. Kobata, and A. Fujishima: Appl. Phys. Lett. 51 (1987) 1685.

[19] K. B. Sundaram and Ashamin Khan: J. Vac. Sci. Technol. A 15 (1997) 428. “Work function determination of zinc oxide films”

[20] K. Dairiki, A. Yamada, and M. Konagai: Jpn. J. Appl. Phys. 40 (2001) 486.

[21] H. Tasaki, W. Y. Kim, M. Hallerdt, M. Konagai, and K. Takahashi: J. Appl. Phys. 63 (1988) 550.

[22] T. Tiedje, J. M. Cebulka, D. L. Morel, and B. Abeles: Phys. Rev. Lett. 46 (1981) 1425.

[23] H. Okamoto, K. Hattori and Y. Hamakawa: J. Non-Cryst. Solids 137&138 (1985) 627.

[24] C. R. Wronski : Sol. Energy Mater. 1 (1979) 287.

[25] K. Itoh, H. Matsumoto, T. Kobata, and A. Fujishima: Appl. Phys. Lett. 51 (1987) 1685.

[26] K. B. Sundaram and A. Khan: J. Vac. Sci. Technol. A 15 (1997) 428.

[27] C. R. Wronski, B. Abeles, T. Tiedje and G. D. Cody: Solid State Commun. 44 (1982) 1423.

[28] R. A. Street, D. K. Biegelsen, and R. L. Weisfield: Phys. Rev. B 30 (1984) 5861.

[29] N. Beck, N. Wyrsch, Ch. Hof, and A. Shah: J. Appl. Phys. 79 (1996) 9361.

[30] G. Ganguly and A. Matsuda: Jpn. J. Appl. Phys. 31 (1992) L1269.

[31] A.O. Pudov, J.R. Sites, M.A. Contreras, T. Nakada, H.W. Schock:, Thin Solid films 480 (2005) 273.

Chapter 4

Fabrication of a-Si:H solar cell for Application of Spectrum Splitting Top cell

4-1 Introduction

In Chapter 3, the numerical analysis of amorphous silicon based solar cell and CIGS solar cell with spectrum splitting method to investigate the most preferred band gap and thickness combination were demonstrated splitting wavelength as well. From this theoretical study, it was found that a top cell with a band gap of 2.0 eV and bottom cell with a band gap 1.1eV are required to achieve an efficiency of over 24%. First, to make wide band gap of amorphous silicon based solar cell, low temperature and high hydrogen dilution method are promising candidates to fulfill this requirement. Several research groups have previously reported their studies on the properties of low temperature and high hydrogen dilution [1]. This wide band gap film has been widely used in p-i-n solar cell as: 1) a widegap intrinsic layer in multijunction solar cells, 2) a wide-gap p-type window layer for a-Si:H cells, and as 3) a compositionally graded interface buffer layer between the boron-doped p-type a-SiC:H layer and the i-layer in a-Si:H solar cells [1]. In this chapter, we are committed to the fabrication of wide-gap silicon films and solar cells without any source gases such as oxide and carbide. We have systematically investigated a dependence of optical, electrical and structural properties of silicon thin films and solar cells on hydrogen flow rate and substrate temperature.

4-2 Experimental Details

4-2-1 Fundamental Aspects of VHF-PECVD Technique

As briefly explained in chapter 2, PECVD technique is widely used for deposition of silicon based thin films, such as a:Si:H, c-Si:H, and their alloy materials This deposition method is also called “glow discharge deposition” because of the visible luminosity of the plasma region. The first preparations of a-Si:H using PECVD method were proposed by Chittick [2] as well as by Spear and LeComber in 1969 [3]. Figure 4.1 shows a schematic diagram of a typical PECVD chamber and its important parts. The PECVD consist of two electrode plates (cathode and anode) located in the parallel, a pumping system, heater, pressure controller and RF or VHF power supply. The substrate is attached to a ground and is heated by a heater. The air inside the chamber is evacuated by pumping system, which usually has a turbo molecular pump backed with a mechanical pump. The chamber pressure is controlled by a control value. In the PECVD process, a silicon source such as SiH_4 or a mixture of SiH_4+H_2 is introduced into the vacuum chamber. An RF or VHF power line is connected to one electrode plate (cathode) while the other plate connected to the ground (anode). By passing voltage between the two electrode plates with low chamber pressure in the range of 0.005 to 10 Torr, depending on the geometry of the vacuum chamber, then the plasma will occur. The plasma excites and decomposes the source gas and generates many radicals and ions, and then the radical diffuse to the substrate and silicon film is grown in the surface. The deposition process of RF-PECVD technique can be described as a four-step process [4]. (i) The first step is the primary reaction between electrons and SiH4, which results in the mixture of ions and free radicals. (ii) The second step is the transport of these species to the surface of substrate, which is accompanied by multiplicity of secondary reactions, e.g., ion-molecule, photon-molecule. (iii) The third step is the reactions of ions and free radicals with, or their adsorption onto, the surface of the substrate. (iv) The fourth step is the process by which these species or their reaction products are incorporated into the growing film or are re-emitted from the surface into the gas-phase. In the PECVD process, there are many deposition parameters that affect the film quality, such as the deposition pressure, RF power and frequency, substrate temperature, and others. A good uniformity can be obtained by a low deposition pressure, while a high deposition pressure is preferable for depositing c-Si:H materials In general, the typical deposition pressure of a-Si:H is around 0.5 to 1 Torr. If the RF power is lower, the deposition rate will drop and it is difficult to maintain plasma, however the higher RF power leads to the increase in deposition rate and also a silicon polyhydride powder. The typical RF power is set at around 10 to 100 mW/cm2 [5]. Moreover, the substrate temperature is also an important factor for the quality of a-Si:H films. Normally the substrate temperature is kept around 150 to 350 ^{o}C. In case of Si-based films that are fabricated under lower substrate temperature, more H is incorporated in the films and leads to the increase of optical band gap (E_{opt}). If the substrate temperature is low (<150 ^{o}C), the silicon polyhydride will be formed unless a high H_2 dilution is used. In contrast, with a high substrate temperature (>350 ^{o}C), Eopt is reduced because of less H incorporation. The silicon films that are deposited at high temperatures show a high degradation of material quality due to the small amount of hydrogen passivation dangling bonds. The electrode spacing (distance between anode-cathode) gap is usually set at around 1 to 5 cm for a-Si:H deposition. A small gap is needed for a uniform deposition, while a wide gap is easier to maintain plasma. Since the conventional RF-

PECVD technique has a low deposition rate, the VHF-PECVD technique was first developed by a group at Neuchatel in order to improve the deposition rate of a-Si:H films [6-2]. In this technique, the plasma excitation frequency is increased from the conventional RF (13.56 MHz) to the VHF range (30-200 MHz). It has been reported that the deposition rate increased linearly with an increase of frequency [9]. A higher deposition rate (5-10 times) is achieved for a-Si:H which are deposited under the same plasma power as conventional RF-PECVD [6, 9-11]. In addition, the VHF-PECVD shows a higher deposition rate of more than 1 nm/s without making polyhydride which is found when deposition rates are increased by increasing the RF power at a low frequency. A higher deposition rate is needed to obtain a lower production cost of a-Si:H based solar cells. The reasons for the higher deposition rate and powder-free for a-Si:H materials deposited by VHF-PECVD technique are not clear yet. At present, it is assumed that the advantageous effect is due to an enhancement in the high energy tails of the electron energy distribution function of plasma [9,11-12]. It has been reported that the a-Si:H single junction solar cells with the i-layer fabricated by VHF-PECVD with a high deposition rate (1 to 2.5 nm/s) showed less degradation, around 10 to 20% [13]. Moreover, a-Si:H solar cells fabricated under high VHF power condition, which means a high deposition rate, show superior performance and stability than solar cells with intrinsic layers deposited in the same deposition condition at a high deposition rate using a conventional RF plasma [13]. In addition to the high deposition rate, a low ion bombardment is another attractive feature of the VHF-PECVD technique. Chatham et al. have found that the mean ion energy (ion bombardment) decreases with increasing the plasma excitation frequency [14]. Besides, an excitation frequency larger than 50 MHz prevents the occurrence of Si ions energies, as shown in Fig. 4.2 [15].

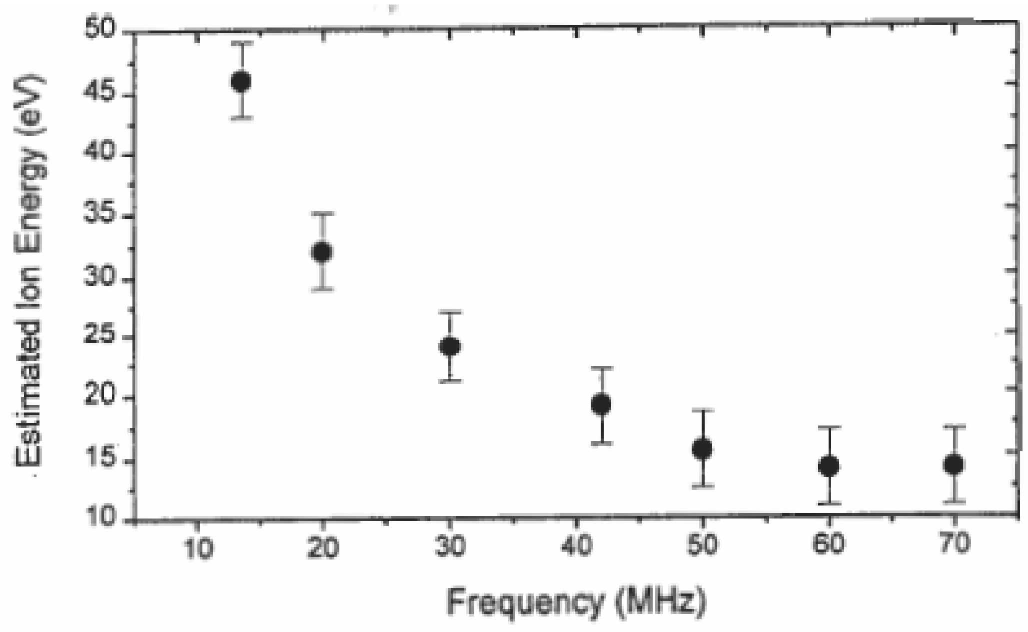

Figure 4.1 Estimated peak Si-ion energies for SiH4 plasma as a function of excitation frequency [15]

The disadvantage of VHF-PECVD technique that suppresses applications in the manufacture of large-scale area solar modules for both a-Si:H and c-Si:H is the un-uniformity of films. This reason is attributed to the standing waves which may be formed on the electrode. In general, if the RF electrode has a single feed point on one side, a standing wave may occur if the electrode has a length of /4 or smaller (= wavelength). For example, at 13.56 MHz RF-PECVD, the wavelength is 22.0 m, which does not limit the size of the area to be coated. However, if the frequency is higher than 60 MHz, the effect of standing waves becomes dominant in large area (~1.0 m2) deposition. Therefore, the multipoint feeding of the VHF power with equal amplitude and phase improves the homogeneity of the VHF potential [11]. By using this new concept for the electrode, i.e. ladder shape or antenna, the problem of uniformity has been solved and large area solar modules have been fabricated [16,17]. From the above explanation, it is clear that the VHF-PECVD technique is beneficial for a-Si:H deposition. The same results, i.e. a better film quality compared to the conventional RF technique, also can be expected in a-Si:H alloys deposition, including a-SiC:H film deposition covered in this study.

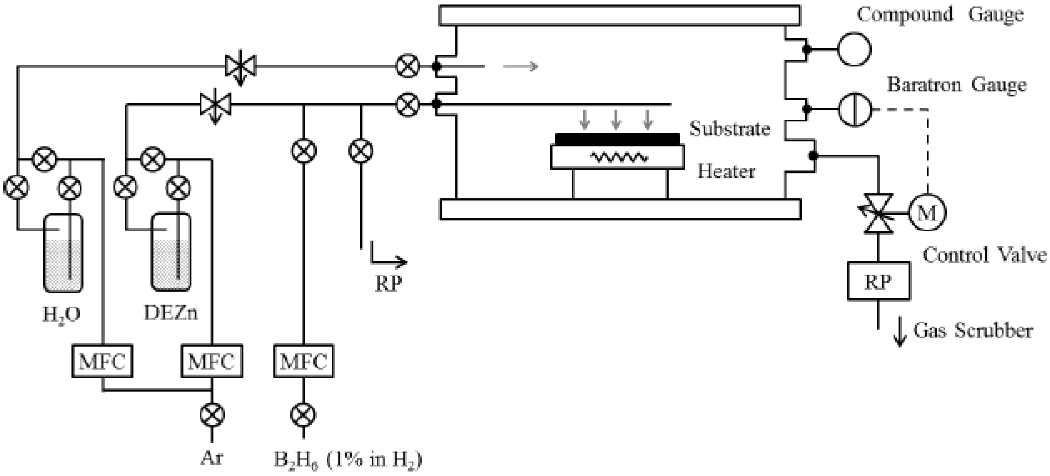

Figure 4.2 Schematic diagrams of scattering effect on textured glass.

4-2-2 Experimental setup

Silicon films were prepared with very high frequency plasma enhanced chemical vapor deposition (VHF-PECVD, 60MHz) has been used in this experiment. Gas mixture of silence (SiH_4) and hydrogen (H_2) were used. Two types of substrates have been prepared. For the Transparent conductive oxide (TCO) films, the glass substrate covered with fluorine-doped thin oxide (SnO_2:F) which is called Asahi VU type glass, and boron-doped znic-xoide (ZnO:B) deposited by metal organic CVD (MOCVD) technique were maianly used in this study. The main feature of these TCO films is that they have naturally textured surface after film deposition, which works for light scattering effect in figure 4.2. Figure 4.3 shows a schematic diagram of the MOCVD system used in this study. ZnO films were carried out with the diethylzinc (DEZ) and H2O as reactant gases. They are contained in bubbles and kept in temperature-controlled baths. These reactant gases were bubbled with purified Ar gas. To obtained high conductivity, B2H6 gas was also attemted as a n-tyype dopant resource. ZnO films were deposited on corning 7059 glass substrate. They an attractive feature of VHF-PECVD is the 5~10 times higher deposition rate than that of RF-PECVD for silicon films and high film quality owing to weakened ion bombardment, which is commonly thought to contribute to lower production cost of a-Si:H based thin film solar cells [18]. The maximum achievable deposition rate is system dependent, where proper impedance matching of rf power to the glow discharge crucial. Figure 4.4 illustrate the photograph of VHF-PECVD system.

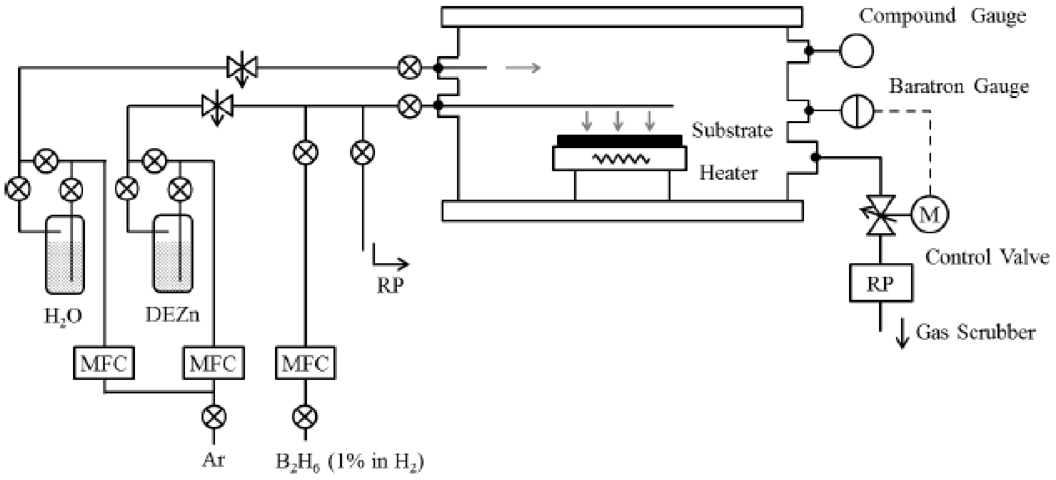

Figure 4.3 Schematic diagrams of the MOCVD apparatus

The system has 5 separate chambers, which are load lock chamber, p-chamber, i-chamber for amorphous silicon films, n-chamber, and i2-chamber for microcrystalline silicon film deposition. The back pressure is as low as 10^{-6} pa. The deposition pressure in the chamber can be controlled in the range of 0~1000 Pa. during deposition, hydrogen flow rate, and substrate temperature and deposition pressure were systematically varied while VHF power density and distance between substrate and electrode were kept constant at 65 mW/cm2 and 2 cm, respectively.

The absorption coefficient and thickness of the films were obtained by spectroscopic ellipsometry (SE). For the measurement, electromagnetic radiation is emitted by light source and linearly polarized by a polarizer. When light is reflected or transmitted by samples, the p-polarized (parallel to the plane of incident) and s-polarized (perpendicular to the plane of incident) light waves depending on the oscillatory direction of its electric filed and shows different behavior. In this study, the angle of incidence is changed from 50 °to 70 °by 10 °and then the complex reflectance ratio, ρ (complex quantity) is measured.

$$\rho = \frac{r_p}{r_s} = \tan(\Psi)e^{i\Delta} \tag{4.1}$$

Where r_p is the amplitude of the p-polarized light, r_s is the amplitude of the s-polarized light, Ψ is the amplitude component and Δ is the phase difference between incident and reflected light. The resulting phase difference is relevant to the electric dipole oscillation in a dielectric and its thickness. Therefore, dielectric function (ε) , extinction coefficient (κ), thickness (d), of samples is attained. With the result obtained optical bandgap (E_{opt}) of films was calculated by the method established by Tauc. et el[8]. For silicon thin films (~ hundreds of nanometer), absorption coefficient at longer wavelengths, which is relevant to defect absorption, is around 1 cm^{-1}, leading to an absorbance value of 0.1 to 0.2 %, i.e., only about 10^{-4} of the incoming light absorbed by the thin silicon layers. Thus, it is not possible to measure such low absorbance values with the usually and conventional type of photospectrometer, which are based on transmission and reflection measurement. Such a low value of absorbed light will be totally marsked by measurement errors [19]. Then raman spectroscopy is a spectroscopic technique used to study vibrational, rotational, and other low frequency modes in a system. Raman scattering is inelastic scattering of phonon. The laser light interacts with molecular vibrations, phonons or other excitations in the system, resulting in the energy of the laser photons being shifted up or down. Raman shifts are, therefore, affected by vibration of the electronic polarization for constituents in the films which depend on the bonding structure of a sample can be examined by using the technique. A 532-nm Ar-laser was used as an excitation source for raman measurements.

The dark and photo conductivities of the films were characterized by *J-V* measurement using Al coplanar electrodes. The photo conductivity of films and photo *J-V* characteristic of solar cells were measured under standard 1-sun illumination (AM 1.5, 100mW/cm^2). The p-i-n structures solar cells with an area of 0.086cm^2 were fabricated on Eagle XG glass substrates. The solar cell has structure of glass/ZnO:B/p-a-SiC:H/i-a-Si:H/n-μc-SiO:H/Ag/Al, as shown in figure 4.5. Each of p, i and n layers are prepared in the separated chambers to avoid contamination. After the deposition of Ag/Al electrodes with and area 0.086cm^{-2} , the sample was moved to reactive ion etching (RIE) system to remove the rest part of Si layers outside of the Ag/Al electrodes under Ar plasma until transparent conductive oxide was exposed to clearly define the area of solar cells.

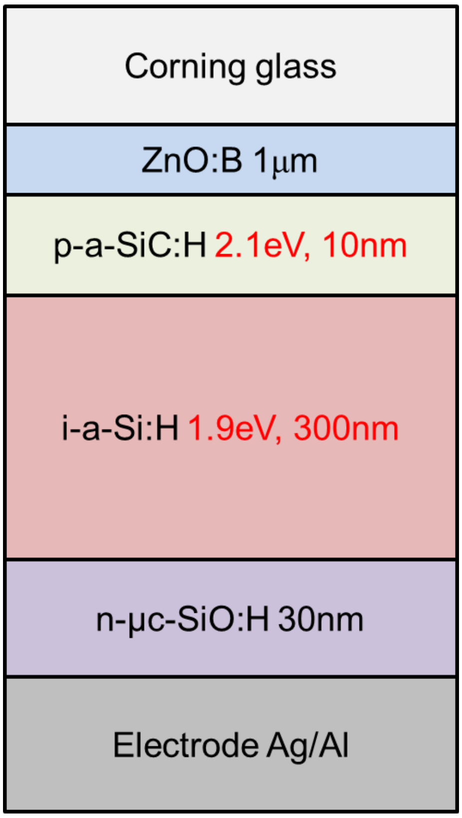

Figure 4.5 The solar cell has structure of glass/ZnO:B/p-a-SiC:H/i-a-Si:H/n-μc-SiO:H/Ag/Al,

Thus, an overestimate of current density of solar cells under illumination, which is contributed by current generated outside the define area of solar cells, is prevented. The quantum efficiency (QE) measurement was also carried out to examine the spectral response of the solar cells. also, the QE measurement was explored under bias voltages in order to diagnose solar cell performance. For the figures having point data, guide lines obtained by liniear/ parabolic least squares fitting methods. [14,15] are included to find the best fitting curve to given set of points by minimizing the sum of the squares of the vertical offsets of the point from the curves and, thereby, to provide an error estimate. The vertical least squares fitting proceeds by finding the sum of the squares of the vertical derivation R^2 of a set of n data point from a function *f(x)*.

$$R^2 = \sum_{i=1}^{n} \left\{ y_i - f\left(x_i, a_{1,} a_{2,\ldots\ldots,} a_n\right) \right\}^2$$

Where, x_i, and y_i demotes data points.

For a linear fit,

$$\mathrm{f}(a_1, a_2) = a_1 + a_2 x_i$$

For a parabolic fit,

$$\mathrm{f}\left(a_1, a_{2,} a_{3,\ldots\ldots} a_n\right) = a_1 + a_2 x_i + a_3 x_i^2 + \cdots \ldots \ldots \ldots \ldots a_n x_i^{n-1}$$

The condition for R^2 to be a minimum is that,

$$\frac{\partial(R^2)}{\partial a_i} = 0$$

In this thesis, n=3 is chosen for a parabolic fit.

4-3 Deposition of a-Si:H thin film using VHF-PECVD

4-3-1 Effect of substrate temperature

As remarked above, it is necessary to investigate the effect of T_s of i-layers on soar cell performance more systemically. In figure,4.4 , E_{opt} of the a-Si:H films are shown with different substrate temperature. The a-Si:H film fabricated under substrate temperature 250C is the i-layer used for the solar cell fabrication. From the figure, it is clearly seen that Eopt of the sample increases with decreasing substrate temperature. One of the reasons for this behavior is reduced hydrogen effusion at low substrate temperature (low hydrogen content), which is due to the decrease in kinetic energy of the species on the film surface during the growth [20-23].

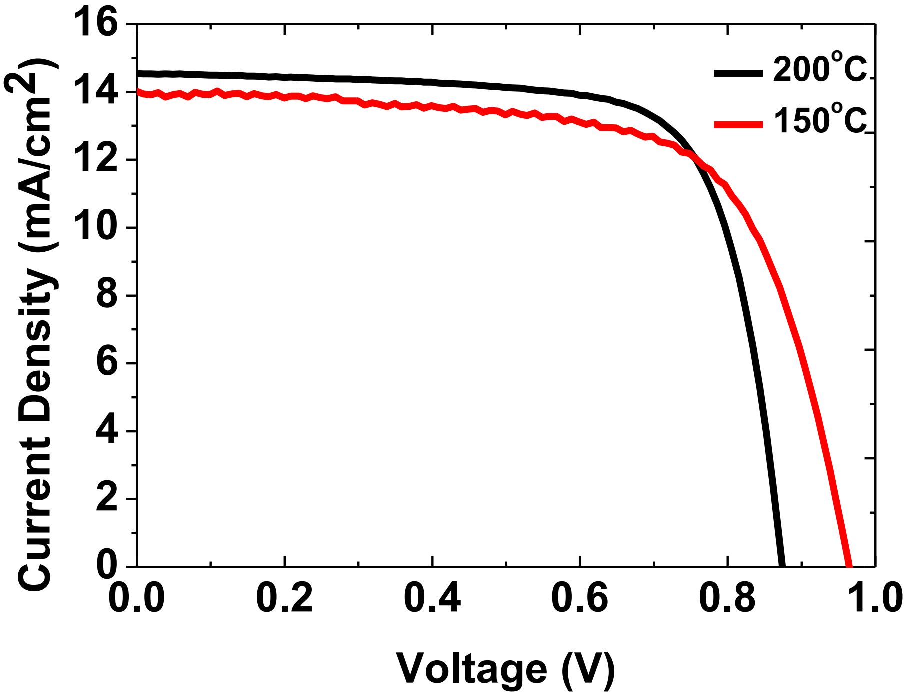

Figure 4.6 *J-V* curves for different substrate temperature for solar cell

Table 4.1 Solar cell performance by different of substrate temperature

	J_{SC} (mA/cm^2)	V_{OC} (V)	FF	Eff (%)
200℃, (1.75eV)	14.86	0.874	0.733	9.52
150℃, (1.9 eV)	14.3	0.982	0.71	10.04

4-3-2 Effect of hydrogen dilution.

The use of strong dilution of silane by hydrogen has attracted special attention for the fabrication of a-Si:H solar cells, because such cells show a reduced lightinduced degradation. Increasing the dilution of the silane by hydrogen even further leads to a morphological transition of the material into hydrogenated microcrystalline silicon ~μc-Si:H. The latter material has also recently acquired a considerable interest as a photovoltaically active material. In this experiment, we set 4 different SiH_4/H_2 ratio and each solar cell performance presented in table 4.2. and these electrical and optical properties presented in figure 4.7 and 4.8.

Table 4.2 Solar cell performance by different of SiH_4/H_2 ratio

SiH_4/H_2 ratio	**Voc(V)**	**Jsc(mA/cm2)**	**FF**	**Eff.(%)**
R= 6.25	0.95	14.44	0.72	9.98
7.5	0.98	14.24	0.67	9.28
8.75	0.98	14.16	0.69	9.52
10	0.97	13.75	0.59	7.91

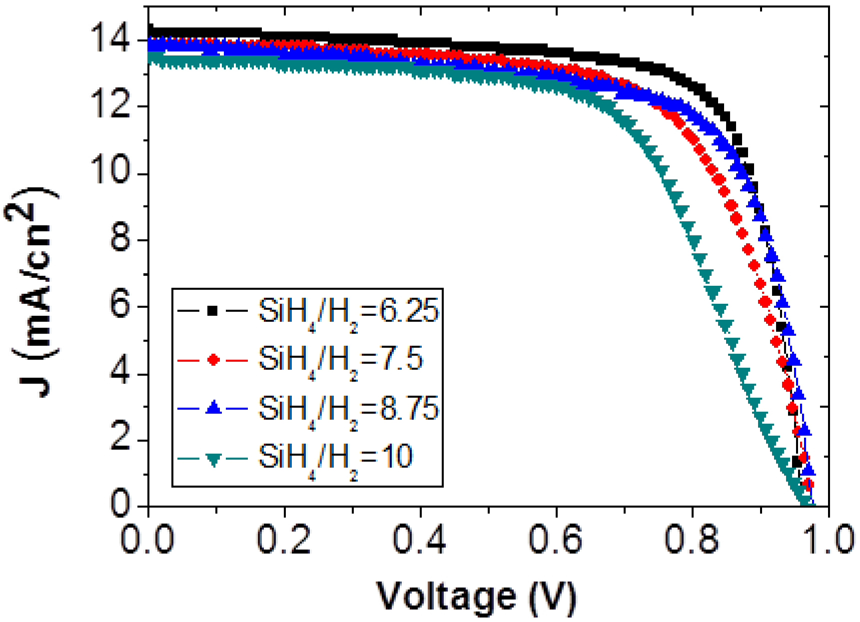

Figure 4.*7* *J*-*V* curves for by various SiH_4/H_2 ratio for solar cell

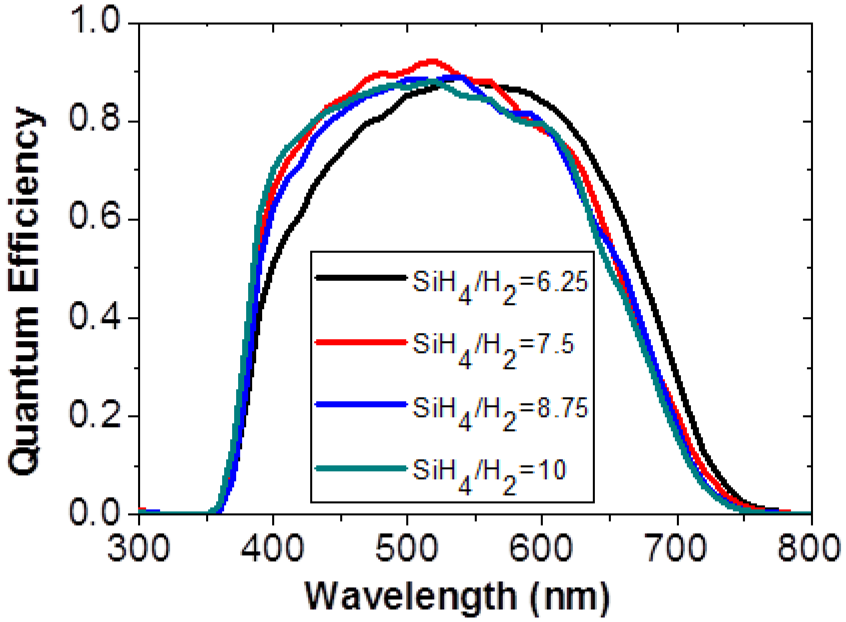

Figure 4.*8* Quantum efficiency by various SiH_4/H_2 ratio

Our measurements indicate that electrical properties shows in figure4.7 and the lowest SiH_4/H_2 ratio has best solar cell performance (Voc=0.95V, Jsc=14.44mA/cm^2.FF=0.72 and Eff. =9.98%) but otherwise from the quantum efficiency, the lowest SiH_4/H_2 ratio has poor response at 400~550nm region. But for highest SiH_4/H_2 ratio has good photo response at short wavelength but it has poor electrical properties. For highest SiH_4/H_2 ratio of absorber layer has transition for microcrystalline so it has good quantum efficiency and poor electrical properties. So it is very important to find proportionality constant between the integrated absorption strength of the rocking fully amorphous layers deposited at moderate dilution and is additionally applicable to the microcrystalline layers deposited at high dilution

4-3-3 Dependence of TCO substrates

The important TCO semiconductors are impurity-doped ZnO, In_2O_3, SnO_2 and CdO, as well as multi-component oxides consisting of combinations of ZnO, and SnO_2. F doped SnO_2 TCO thin films are the preferable materials for most present applications. At present, ZnO and SnO_2 are using as thin-film transparent electrode applications. The best candidates are ZnO:B thin films, which the resistivity could be as low as 10^{-4} cm, and their extinction coefficient *k* in the optical visible range (VIS) could be lower than 0.0001, owing to their wide optical band gap (E_g) that could be greater than 3 eV.

So most common material for TCO substrate for solar cells are SnO_2 and ZnO. In figure 4.9 the solar cell quantum efficiency has compared by different TCO substrate. so far, ZnO:B adopted as TCO material for this research solar cell, however since ZnO has lower band gap (3.3eV) than SnO_2 (3.7eV), this difference is very critical issue especially for application top cell which is required good response at short wavelength . so instead of ZnO, SnO_2 substrate has been prepared which was sold Asahi glass company named Asahi-VU types. It has very specific texture on surface to helps effective light scattering.

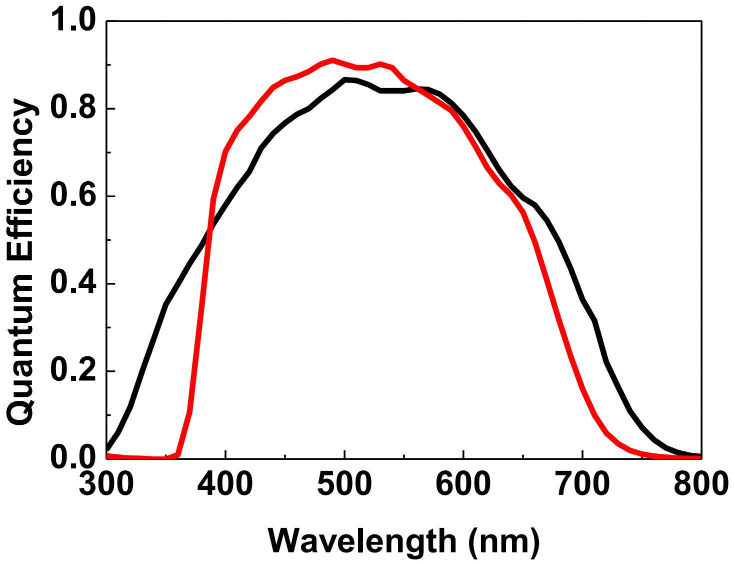

Figure 4.9 Quantum efficiency by different type of TCO substrate a-Si:H solar cell red is ZnO, black is SnO_2 (absorber layer thickness both 300nm)

- Effect of etched SnO_2:F TCO substrate

To further increase the performance of this spectrum splitting type solar cell, the top cell (a-Si:H) with high open circuit voltage (V_{oc}) and good response at the short-wavelength has to be developed. To achieve better response at the short-wavelength, transparent and conductive oxide (TCO) with wider band gap [25] such as tin oxide (SnO_2, 3.6 eV) has been considered instead of zinc oxide (ZnO, 3.3 eV). In figure 1, comparison of external quantum efficiency (EQE) data for ZnO and SnO_2 as the front electrode has shown. As can be seen, solar cell with SnO_2 front TCO has higher photo response at the short-wavelength [26, 27]. Asahi VU glass (SnO_2:F, 700nm) substrates have been used. These Asahi VU glass has certain texture on surface. In order to flatten Asahi VU substrates, these textured SnO_2 substrates were etched by a standard reactive Ion Etching (RIE) in Ar environment. The details of RIE etching condition are as follows: Ar flow rate 10 sccm, radio frequency (rf) power supply with an operation power of 100W, chamber pressure was held constant at 4 Pa and etching time was varied from 10 and 20 min. Using these etched substrate, p-i-n type a-Si:H solar cells with a 1.9 eV absorber layer and area of 0.086 cm^2 have been fabricated. The solar cell structure of glass/SnO_2:F/hydrogenated amorphous silicon carbide for p layer (p-a-SiC:H, 2.1eV, 30nm)/buffer/hydrogenated amorphous silicon for intrinsic layer (i-a-Si:H, 1.9eV, 300nm)/hydrogenated microcrystalline silicon oxide for n layer (n-μc-SiO:H, 30nm)/ Ag/Al was used. In order to get wider band gap solar cell, low temperature 150℃ and high H_2 dilution (SiH_4/H_2= 8.5) conditions have been employed to get absorber layer while the inter-electrode distance, very high frequency (VHF) power density and chamber pressure were kept constant at 2 cm, 1 mW/cm^2 and 50 Pa, respectively

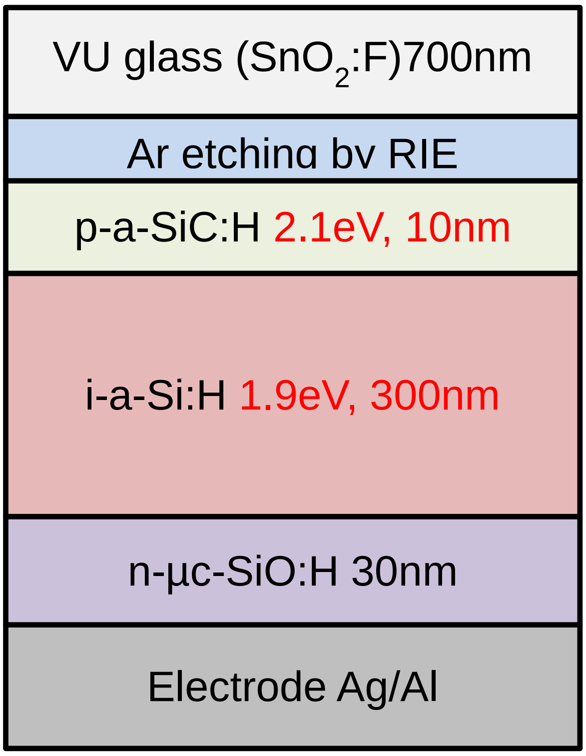

Figure 4.10 The solar cell has structure of glass/SnO_2:F/p-a-SiC:H/i-a-Si:H/n-µc-SiO:H/Ag/Al,

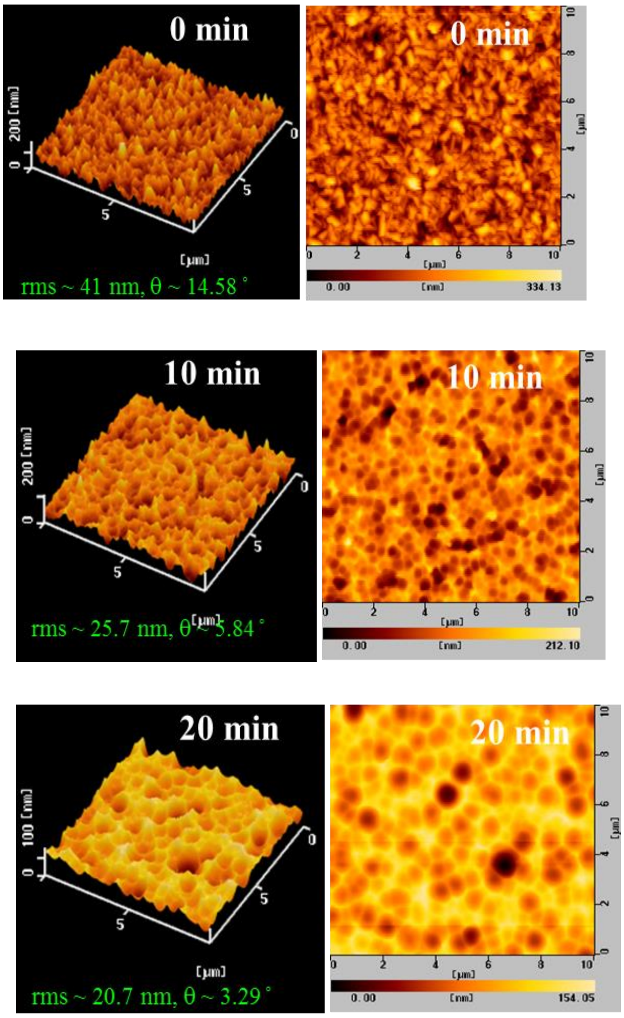

Figure 4.11 the surface morphology image by AFM as increasing Ar etching time on Asahi VU (SnO_2:F) TCO substrate

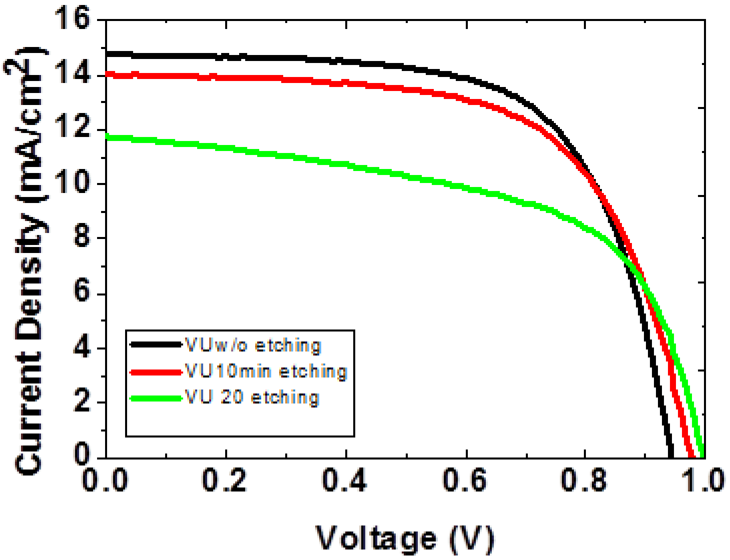

Figure 4.12 *J-V* curves for by various Ar etching time on Asahi VU (SnO_2:F)substrate

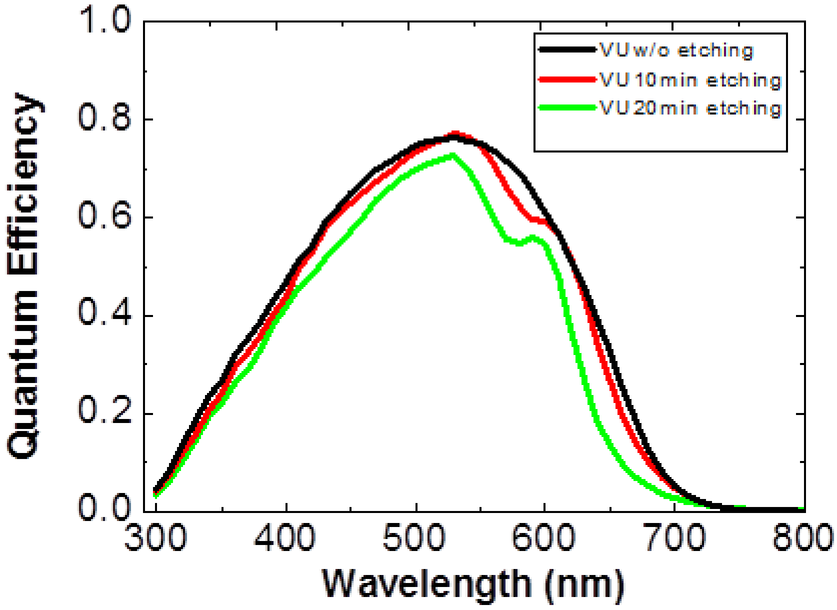

Figure 4.13 Quantum Efficiency by various Ar etching time on Asahi VU

(SnO_2:F)substrate

First, surface morphology with different etching time on VU glass substrate was observed by atomic force microscopy (AFM) as shown in Fig.4.11. The root mean square (RMS) of etched VU glass became lower from 41 nm, down to 25nm and 20 nm when Ar etching time 20 min. The tip of the texture on etched glass became round shape as well. Then using these etched glasses, amorphous solar cells have been fabricated. The performance of Solar cells is presented in Table 4.3. As increasing etching time on VU glass substrate increased, V_{oc} increased. However FF and short circuit current (J_{sc}) decreased as shown in figure 4.12 and its quantum efficiency presented in figure.4.13. For longer Ar etching effected electrical property especially its short-circuit current because the texture has been smooth and effect of light scattering became weaker. So photons are decreased in absorber layer. Otherwise as we expected the open circuit-voltage increased as increasing of etching time.

Table 4.3 Solar cell performance by different Ar etching time on Asahi VU substrate

etching time	**Jsc (mA/cm^2)**	**Voc (V)**	**FF**	**Eff (%)**
0min	14.759	0.943	0.65	9.11
10min	14.024	0.978	0.63	8.68
20min	11.763	0.998	0.58	6.76

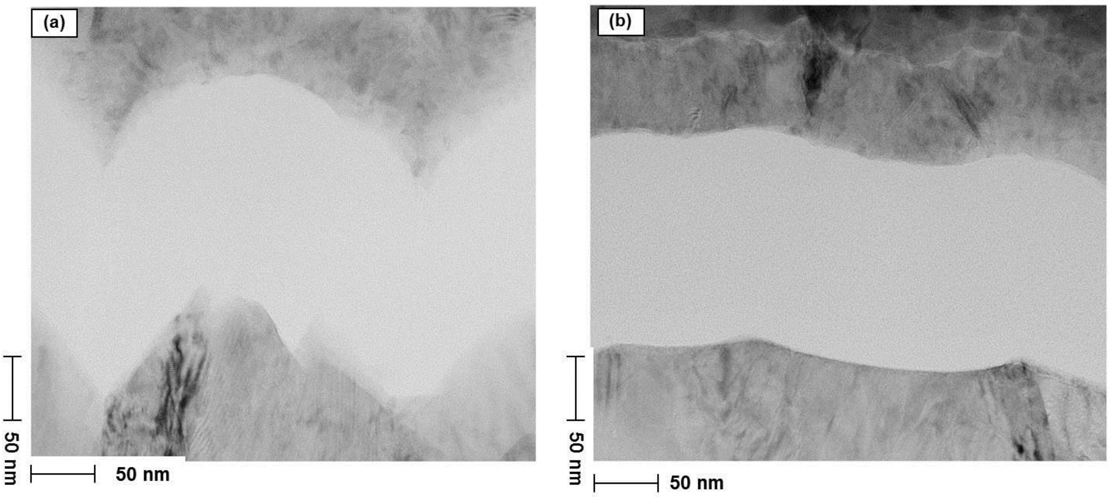

Figure 4.14 Cross section image for the p-i-n solar structure (glass/SnO_2:F/ p-a-SiC:H/i-a-Si:H/n-µc-SiO:H/Ag/Al on Asahi VU (SnO_2:F) substrate (a) is no Ar treatment SnO_2:F substrate and (b) is 10 min Ar etching treatment SnO_2:F substrate

- Effect of bi-layer of SnO_2:F/ZnO:B TCO substrate

However, since SnO_2 can be easily damaged by hydrogen plasma [28], we have also studied the application of multilayer SnO_2/ZnO substrate. Furthermore, it is generally known that the haze of TCO film affects the cell Voc substantially because when the surface is rough, effective p-layer thickness is thinner and it led lower Voc [29]. So in this study we consider how to smoothen the TCO surface by Ar plasma treatment in order to obtain higher Voc. Flatter TCO can lower the collection efficiency at the longer-wavelength, but this will not affect the performance of the top cell so much since it is focused to use the light at the short-wavelength. Then for multilayer (SnO_2/ZnO) substrate, ZnO films were deposited onto the etched Asahi VU glass by metal organic chemical vapor deposition (MOCVD) technique. Thickness of the ZnO films was about 100 nm. Using these etched substrate, p-i-n type a-Si:H solar cells with a 1.9 eV absorber layer and area of 0.086 cm^2 have been fabricated. The solar cell structure of glass/SnO_2:F/ZnO/hydrogenated amorphous silicon carbide for p layer (p-a-SiC:H, 2.1eV, 30nm)/buffer/hydrogenated amorphous silicon for intrinsic layer (i-a-Si:H, 1.9eV, 300nm)/hydrogenated microcrystalline silicon oxide for n layer (n-μc-SiO:H, 30nm)/ Ag/Al was used. In order to get wider band gap solar cell, low temperature 150℃ and high H_2 dilution (SiH_4/H_2= 8) conditions have been employed to get absorber layer while the inter-electrode distance, very high frequency (VHF) power density and chamber pressure were kept constant at 2 cm, 1 mW/cm^2 and 50 Pa, respectively

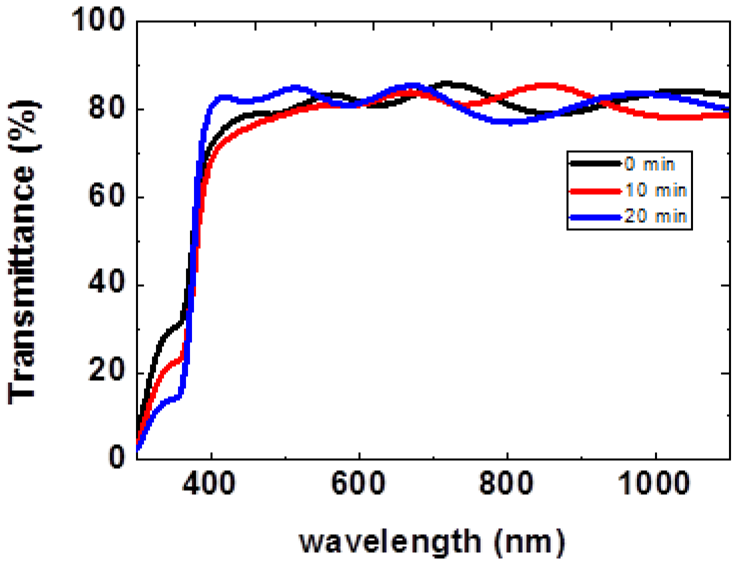

Figure 4.14 the surface textured image by SEM as increasing Ar etching time on Asahi VU (SnO_2:F)/ZnO:B bilayer of TCO substrate

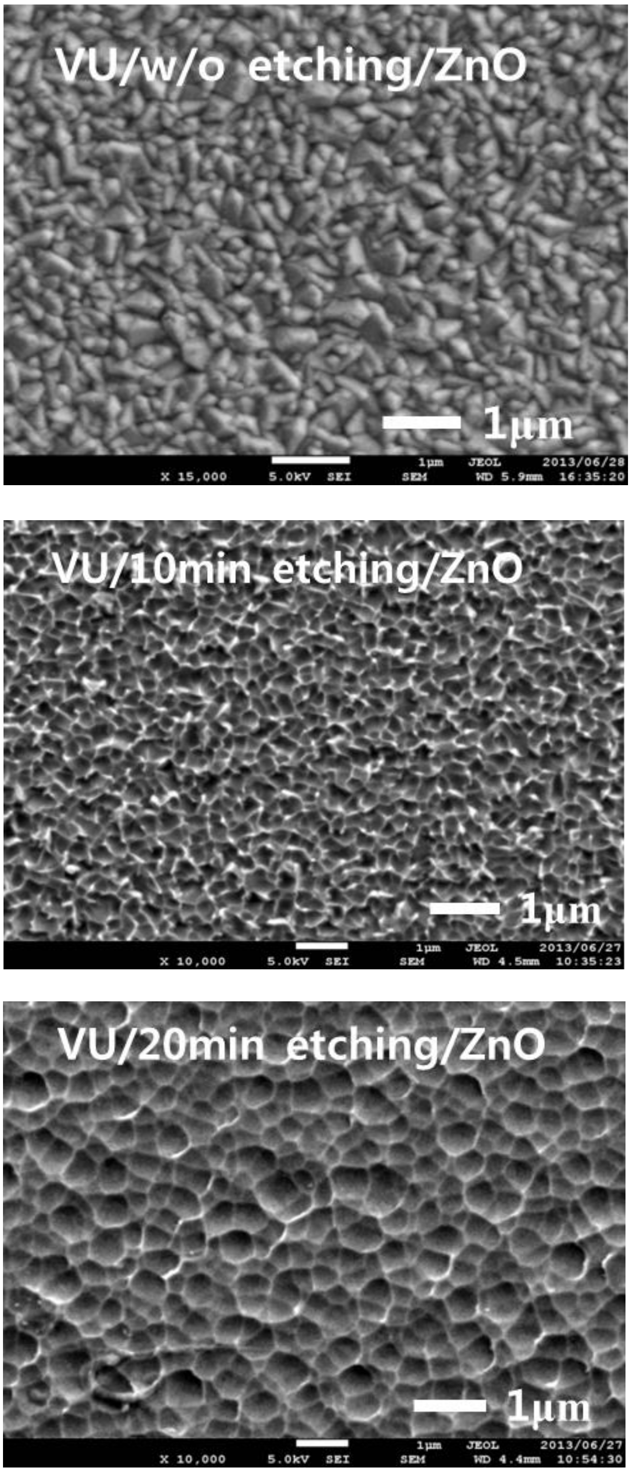

Figure 4.15 the surface textured image by SEM as increasing Ar etching time on Asahi VU (SnO_2:F)/ZnO:B bilayer of TCO substrate

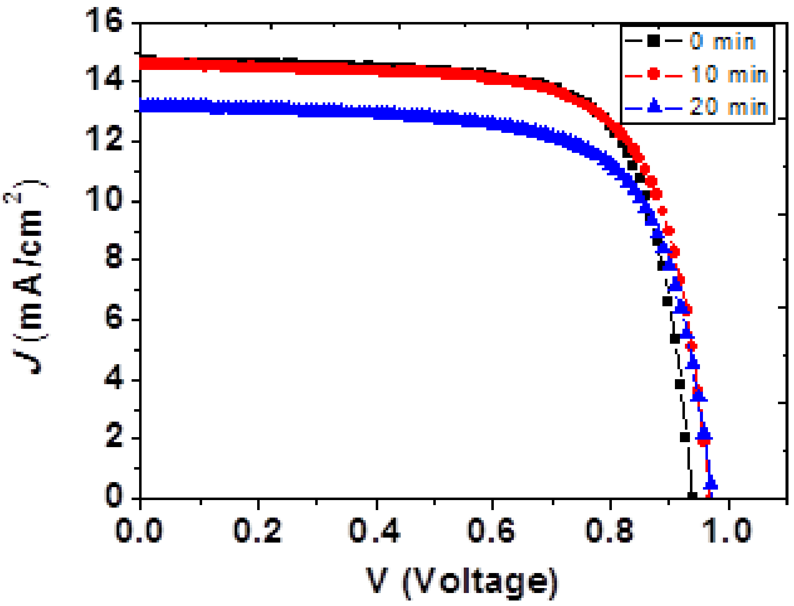

Figure 4.16 *J-V* curves for by various Ar etching time on Asahi VU VU (SnO_2:F)/ZnO:B bilayer of TCO substrate

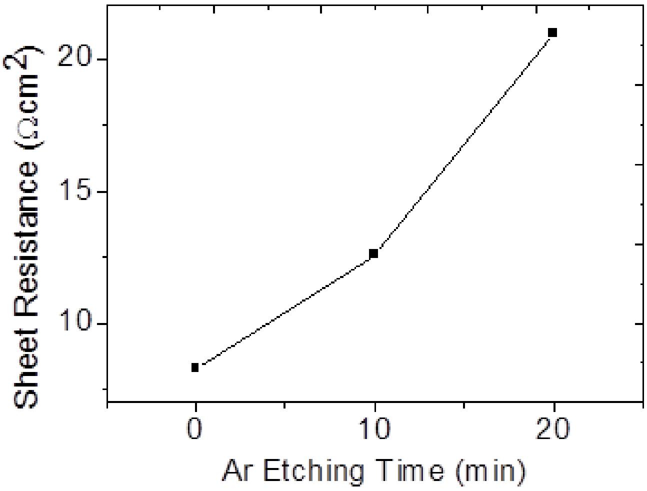

Figure 4.17 sheet resistance of bi-layer of TCO substrate by various Ar etching time on Asahi VU VU (SnO_2:F)/ZnO:B bilayer of TCO substrate

Table 4.3 Solar cell performance and series resistance by different Ar etching time on Asahi VU substrate

Etching time	**Voc(V)**	**Jsc(mA/cm^2)**	**FF**	**Eff.(%)**	**Rs(Ω·cm^2)**
0min	0.940	14.661	0.73	10.09	9.7719E-01
10min	0.969	14.602	0.712	10.08	1.2120E+00
20min	0.975	13.742	0.699	8.99	2.7174E+00

Using etched conventional VU glass, thin layer of ZnO has been deposited and the thickness is 100nm. Surface image checked by SEM by different etching time, as increasing Ar etching time in figure 4.15Then optical and electrical properties of these multilayers are measured. Transmittance of multilayers is shown in fig.4.14 and around 350nm wavelength, ZnO checked. Then sheet resistance (R_{sh}) measured in Figure 4.17. Then structures of amorphous silicon solar cells are fabricated on multilayer substrate. Solar cell's performances are presented in Table 2. And *J*-V figure 4.16. As similar to the results of etched VU glass, V_{oc} increased, but FF and J_{sc} decreased. This may come from the fact that the surface of multilayer SnO_2/ZnO was flat with longer etching time. So that effective p-layer thickness became thicker and this increased the V_{oc}. This may come from the fact that the surface of multilayer TCO was flat with longer etching time so that effective p-layer thickness became thicker and this increased the V_{oc}. On the other hand in Fig. 4 17 presented sheet resistance (R_{sh}) of TCO. As can be seen from that figure, R_{sh} was increasing as increasing of etching time. This can increase the series resistance (R_s) in table 2 of solar cells and these series resistance makes lower FF. even though solar cell performance decreased as increasing of etching time. However, overall performances of solar cells were better with multilayer of SnO_2/ZnO glass comparing to the one fabricated on conventional VU glass substrate.

4.4 Summary

To further increase the performance of this spectrum splitting type solar cell, the top cell (a-Si:H) with high V_{oc} and good response at the short wavelength has been studied. To achieve better response at the short wavelength, SnO_2 with wider band gap has been considered instead of ZnO. However it is found that it is better to cover SnO_2 with ZnO in order to achieve higher performance. Furthermore, it is also found that high V_{oc} with the same efficiency can be obtained by flattening the SnO_2 surface with Ar plasma (10min). These results show that multilayer SnO_2/ZnO substrate which its surface is flatten by Ar plasma is suitable as front TCO for the top cell of spectrum splitting type solar cell.

REFERENCE

[1] K. Baedeker, Ann. Phys. (Leipzig), **22**, 749 (1907).

[2] G. Haacke, Ann. Rev. Mater. Sci. **7**, 73 (1977).

[3] M. Hiramatsu, K. Imaeda, N. Horio, and M.Nawata, J. Vac. Sci. Technol., A 16 p. 669 (1998).

[4] B.G. Lewis and D. C. Paine, Materials Research Society Bulletin, **25**, August 2000, pp. 22-27.

[5] G.J. Exarhos and X.D. Zhou, Thin Solid Films, **515**, 7025 (2007).

[6] E. Fortunato, D. Ginley, H. Hosono, and D.C. Paine, MRS BULLETIN, **32**, March 2007, pp. 242-247.

[7] P. P. Edwards, A. Porch, M. O. Jones, D. V. Morgan, and R. M. Perks, Dalton Trans. **19**, 2995 (2004).

[8] H. Mizoguchi and P.M. Woodward, Chem. Mater., **16**, 5233 (2004).

[9] D.C. Look, B. Claflin, in: G.J. Brown, M.O. Manasreh, C. Gmachl, R.M. Biefeld, K. Unterrainer (Eds.), Progress in Compound Semiconductor Materials IV-Electronic and Optoelectronic Applications, Boston , U.S.A., 2004, Materials Research Society Symposium Proceedings, vol. 829, 2005, p. B8.6.1.

[10] C.G. Van de Walle, Phys. Rev. Lett., **85,** 1012 (2000).

[11] C. Kiliçand A. Zunger, Phys. Rev. Lett., **88**, 095501-1 (2002).

[12] K. Ellmer, J. Phys., D, Appl. Phys., **33**, R17 (2000).

[13] K. Ellmer, J. Phys., D, Appl. Phys., **34**, 3097 (2001).

[14] G. Frank, H. Köstlin, Appl. Phys., A **27**, 197 (1982).

[15] G. Masetti, M. Severi, S. Solmi, IEEE Trans. Electron Devices, ED**30,** 764 (1983).

[16] D. Chattopadhyay, H.J. Queisser, Rev. Mod. Phys., **53**, 745 (1981).

[17] P. Ebert, Z. Zhang, F. Kluge, M. Simon, Z. Zhang, K. Urban, Phys. Rev.Lett., **83,** 757 (1999).

[18] T. Pisarkiewicz, K. Zakrzewska, E. Leja, Thin Solid Films, **174**, 217 (1989).

[19] Jorge I. Cisneros, Applied Optics, **37** (1998) 5262.

[20] J.I. Cisneros, Applied Optics, **37**, 5262 (1998).

[21] T. Minami, Semicond. Sci. Technol. **20,** S35 (2005).

[22] J.R. Bellingham, W.A. Phillips, and C.J. Adkins, J. Phys. Matter, **2**, 6207 (1992).

[23] T. Minami, H. Sato, H. Nanto, and S. Takata, Jpn. J. Appl. Phys., Part 2: Lett. **25,** L776 (1986)..

[24] J.W. Bae, S.W. Lee, and G.Y. Yeom,, J. Electrochem. Soc. **154,** D34–D37 (2007).

[25] J. Müller, B. Rech, J. Springer, M. Banecek. Solar Energy. Vol.77 (2004), 917–930 “TCO and light trapping in silicon thin film solar cells”

[26] S. Lany, A. Zunger: Phys. Rev. Lett. 98, 045501 (2007) “Dopability, Intrinsic Conductivity, and Nonstoichiometry of Transparent Conducting Oxides”

[27] V. Srikant, D. R. Clarke: J. Appl. Phys. 83, 5447 (1998). “On the optical band gap of zinc oxide”

[28] A. Nagata, O. Bierwagen, M. E. White, M. Tsai, J. S. Speck: Journal of Applied Physics 107 (2010) 033707. “Study of the Au Schottky contact formation on oxygen plasma treated n-type SnO2 (101) thin films”

[29] M. Taguchi, A. Terakawa, E. Maruyama M. Tanaka: Progress in Photovoltaics: 13(2005)481–488 “Obtaining a higher Voc in HIT cells”

Chapter 5

Optimization of a-Si:H Based Solar Cell for Spectrum Splitting Technique

5-1 Introduction

As introduced in Chapter 1, our final target is to develop the thin-film full spectrum solar cells with low-concentration ratios. The main characteristics of these solar cells are the multi-junction structure with thin-film materials, the four-terminal structure, and low-concentration of sunlight. In this chapter, the four-terminal structure among them is developed. Amorphous silicon and chalcopyrite materials are used as absorber layers of top and bottom cells, respectively. Based on the simulation and experimental studies, the results and the future potential are discussed.

5-2 Concept of Mechanically Stacked tandem structure

5-2-1 Two terminal and four terminal configurations

The thin-film full spectrum solar cells proposed in Chapter 2 are based on the multi-junction structure with more than five absorber layers. The advantage of multi-junction structure is to utilize the solar radiation spectrum effectively. In general, the incident photon energy is much higher than the absorber's band gap energy, the energy related to the difference between two energies are released as heat losses. For the case of multi-junction solar cells, the each component subcell absorbs photons whose energy is corresponds to the band gap of each absorber. Then the thermal energy losses can be much suppressed as increasing the numbers of junction of solar cells. There have been many studies about various kind of multi-junction structure and the very-high efficiencies of over 30% have ever been achieved with III-V compound semiconductor materials [1-7]. On the other hand, multi-junction solar cells have a disadvantage on the current match. In a tandem structure each component subcell of multi-junction cells is connected in series, and then the operating voltage is added up and the photocurrent is limited to the smallest one of the component subcells. Once the photocurrent from each component subcell does not balance, the limited J_{sc} lowers the solar cells performance. Therefore it is important to solve the problem of current mismatch and the solar cells structure should be carefully determined.

We simply assumed above without preamble that the multi-junction solar cells consist of two-terminal tandem structure. However, there are several imaginable tandem structures of two-, three-, and four-terminal types [8] for multi-junction solar cells. For the case of two-terminal type, the top and bottom cells are stacked and electrically connected in series, and thus their photocurrents must be equal to obtain the optimum output, even though they can achieve very-high efficiency as described above [1-7]. For the case of three-terminal type, such a current match is not need to be achieved between two main subcells because they are stacked but separately connected. Some reports have shown the potential for high efficiency with this type [9-11]. However, an application of three-terminal type cells to solar modules with high voltage operation is considered to be hopeless because the connection scheme is complex due to extra subcell. The extra subcells are needed to be connected in parallel to each three-terminal cell so that the output voltage can be matched between the subcell 1 and 2 and furthermore the photocurrent of the extra subcell must be same as that of subcell 2

(a) Two-terminal

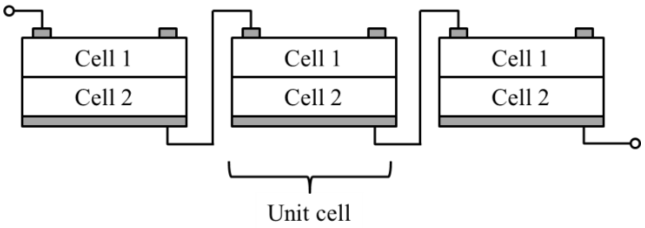

(b) Three-terminal

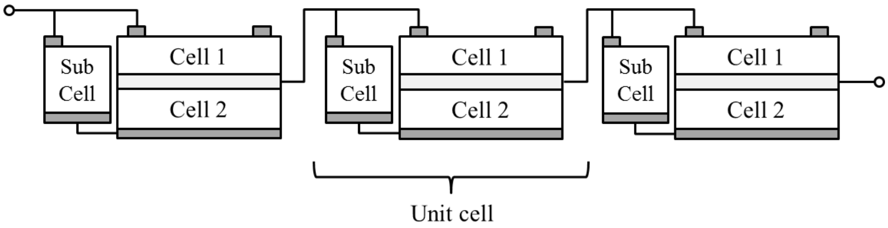

(c) Four-terminal

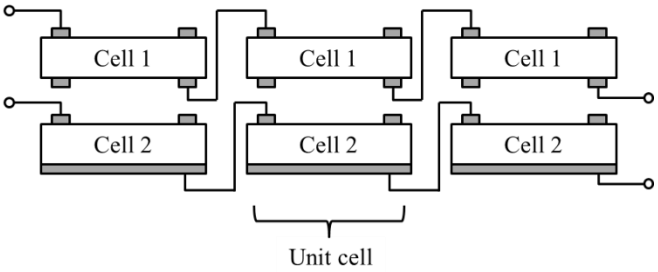

Figure 5.1 Schematic diagrams of electrical connections of (a) two-, (b) three-, and (c) four-terminal type solar cells for the case of series connected tandem cells.

Meanwhile, for the case of four-terminal type, there is no need to get such precise current and voltage matches. This requirement makes the range of optimum band gap combinations for the two cells much larger. As an example, figure 5.2 shows the comparison of calculated conversion efficiency of two- and four-terminal types by using a-Si top cells and polycrystalline Si (poly-Si) bottom cells [12]. From these results, one can see that achievable theoretical maximum efficiency of the a-Si/poly-Si two-terminal tandem solar cells can be higher than that of a-Si//poly-Si four-terminal type. This is because the results in (b) include the optical losses of 10% and 20% for the top and bottom cells, respectively. Except for the optical losses, the four-terminal types get predominance over the two-terminal ones as shown in figure 5.1**Figure 5.1**. Additionally, by the reason that it is possible for four-terminal type cells to fabricate each component cell independently, the combinations of the component cells become various without the restriction of deposition techniques and temperature etc. There are some theoretical and experimental reports that the candidates for the bottom cells of the four-terminal type would be not only c-Si or poly-Si cells but also $CuInSe_2$ (CIS) or CdTe cells [9, 12-17]. In case of an application of four-terminal tandem solar cells to solar modules, the top and bottom cells are separately connected in series as shown in figure.5.1 (c). However, there are a few reports about the applications probably because there is a problem related to the solar modules output whose voltages or photocurrents are limited by not component cells but modules. It could be solved by using a boost chopper circuit which adjusts the output voltages used in photovoltaic module system. The other one is to design the voltage-matched electric circuit by the precise combination of series- and parallel-connections as some literatures [18,19]. If there problems can be overcome, the chance of the four-terminal solar modules applications could become much larger.

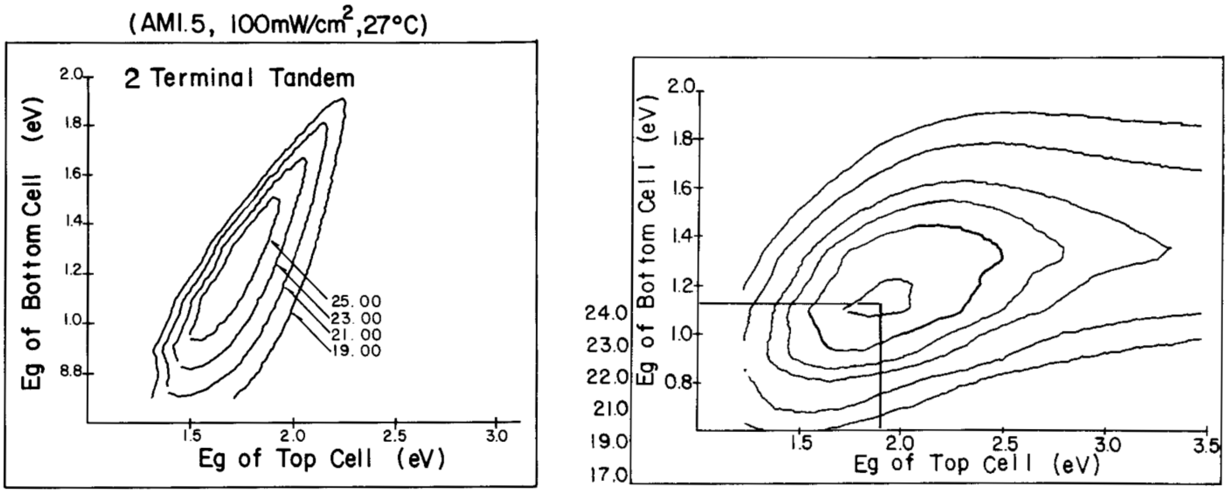

Figure 5.2 Contour map of calculated conversion efficiency of (a) two- and (b) four-terminal tandem cells as a function of bandgap energy of top and bottom cells. The top and bottom cells are based on a-Si and poly-Si, respectively. [12]

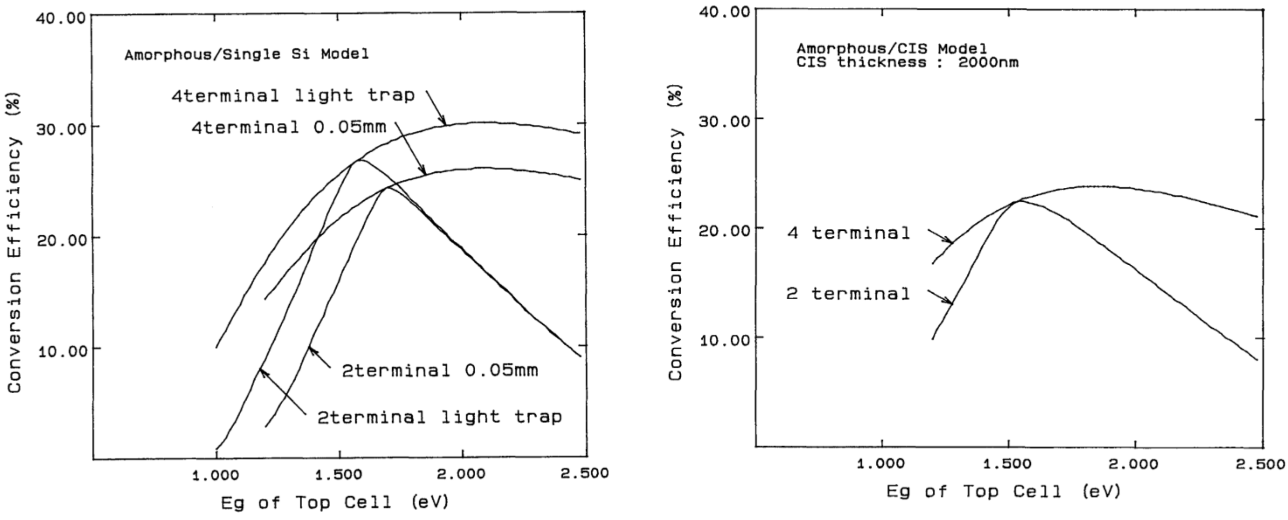

Figure 5.1 Calculated conversion efficiency of tandem solar cells as a function of band gap energy of a-Si top cells with (a) c-Si and (b) CIS bottom cells. [13]

5-2-2 experimental result of four terminals mechanically stacked solar cell

The four-terminal solar cells have ever mostly been studied with mechanically-stacked structure [9, 12-19]. Top cell which is semi-transparent with transparent back electrode consists of superstrate configuration, and bottom cell consist of superstrate or substrate one. The high potential of the mechanically-stacked four-terminal solar cells was explained theoretically as described above, and has been proved. The total conversion efficiency of the four-terminal cells is obtained by the sum of that of the semi-transparent top cell and bottom cell. The total efficiency can and must be higher than that of stand-alone bottom cell. The two cells are stacked with an optical coupler which optically connect and electrically insulate the component cells. The optical coupler is optically transparent liquids [14], silicone oil [15], or polymer [16], etc. It has an important role on optical losses of the four-terminal solar cells as W. Ma et al. [14] have reported the effects of refractive indices of the optical coupler on the solar cells performance. Figure 5.2 shows the photovoltaic performance of four-terminal solar cells as a function of refractive index of an optical coupler. One can see that the photocurrent of bottom cell is strongly depends on the refractive index of an optical coupler. This is because the reflectance and transmittance at the interface between the undermost layer of top cell and the optical coupler layer is defined as a combination of the refractive indices of the two materials.

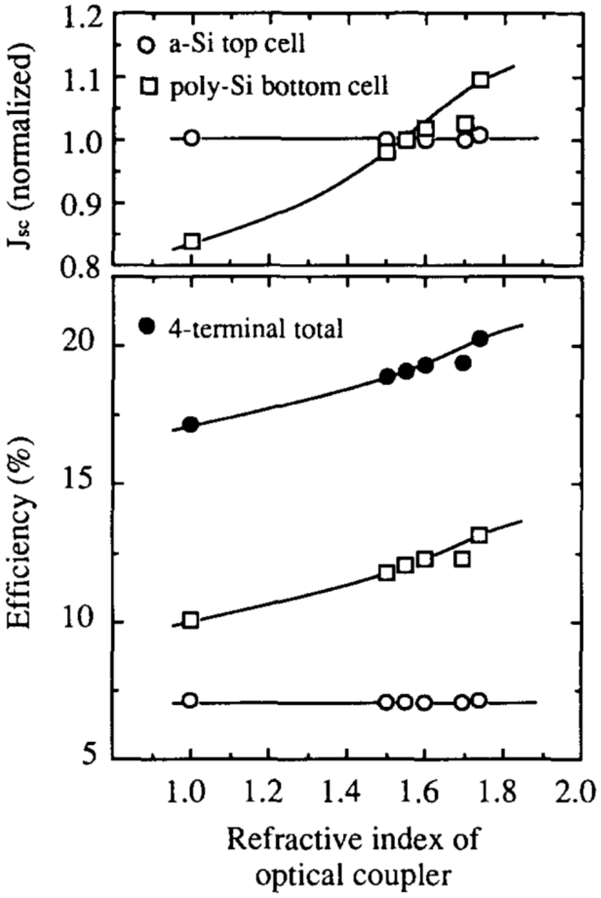

Figure 5.2 Photovoltaic performance of four-terminal a-Si//poly-Si solar cells as a function of refractive index of optical coupling material. [14]

Table 5.1 Photovoltaic performance of mechanically-stacked four-terminal solar cells.

Cell	V_{oc} (V)	J_{sc} (mA/cm^2)	FF	Eff. (%)
a-Si:H//poly-Si [14] (E_g = 1.75/1.12 eV, Area = 0.16 cm^2, AM1, 100mW/cm^2)				
Top	0.917	10.4	0.760	7.25
Bottom	0.575	30.2	0.792	13.75
Total	—	—	—	21.0
Stand-alone poly-Si	0.578	37.2	0.800	17.2
a-Si:H//CIS [16] (E_g = 1.7/1.0 eV, Area = 4 cm^2, AM1.5G, 100mW/cm^2)				
Top	0.871	16.4	0.72	10.3
Bottom	0.432	17.9	0.68	5.3
Total	—	—	—	15.6
Stand-alone CIS	0.455	12.4	0.66	12.4
GaAs//GaSb [18] (E_g = 1.42/0.72 eV, AM1.5D, 100mW/cm^2 × 100 suns)				
Top	1.10	30.9	0.85	28.9
Bottom	0.466	24.5	0.71	8.17
Total	—	—	—	37.0

5-3 Characteristic of Splitter filters

5-3-1 CVI splitter filters

Table 5.2 Detailed properties of CVI filters

Clear aperture	90％
Parallelism	3min
Optical material	BK7
Transmitted wave front error	3 ~ 5λ（effective diameter20 mm）
Cut-off Tolerance	±10 nm
Incident angle	0 °
Transmittance	85％(average from the cut-off wavelength）
Rejection	≥ 99％（from cut-off wavelength）
Coating	Reflection coating one side、antireflection coating other side
Dimensions	50.0×50.0
Thickness	4.0 mm
Surface quality	80-50scratch&dig

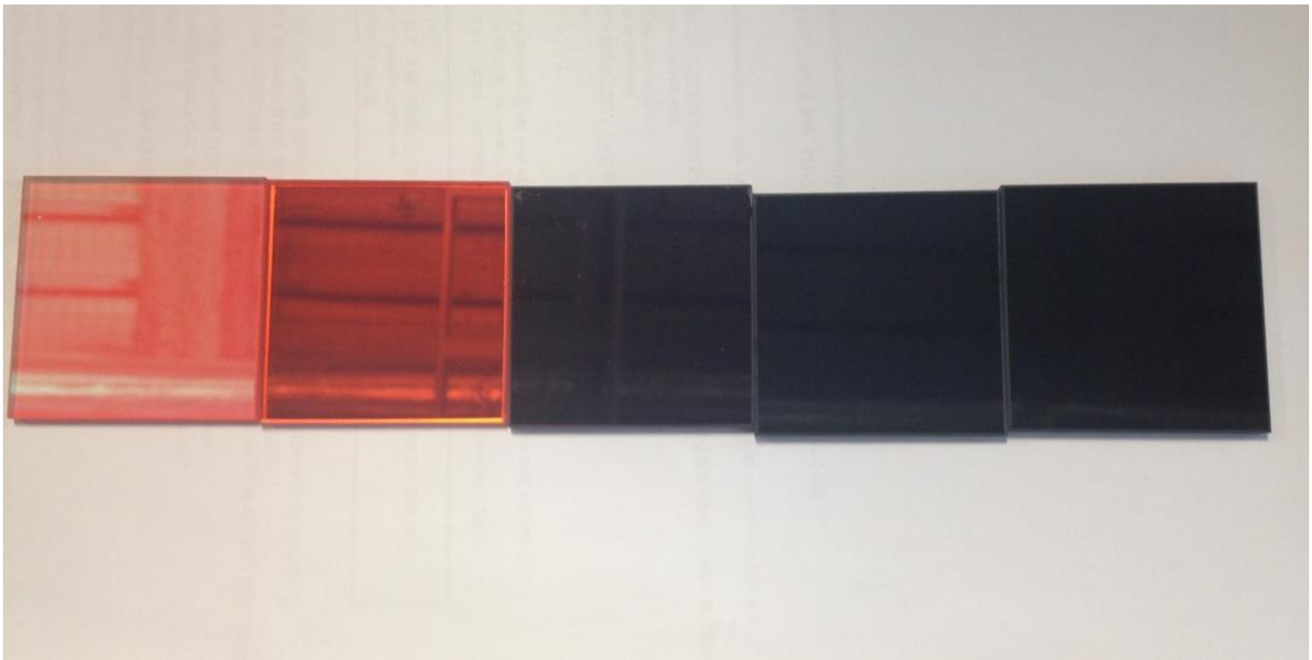

Figure 5.4 CVI optical filters images (from left splitting wavelength 600,650,700,750 and 800nm)

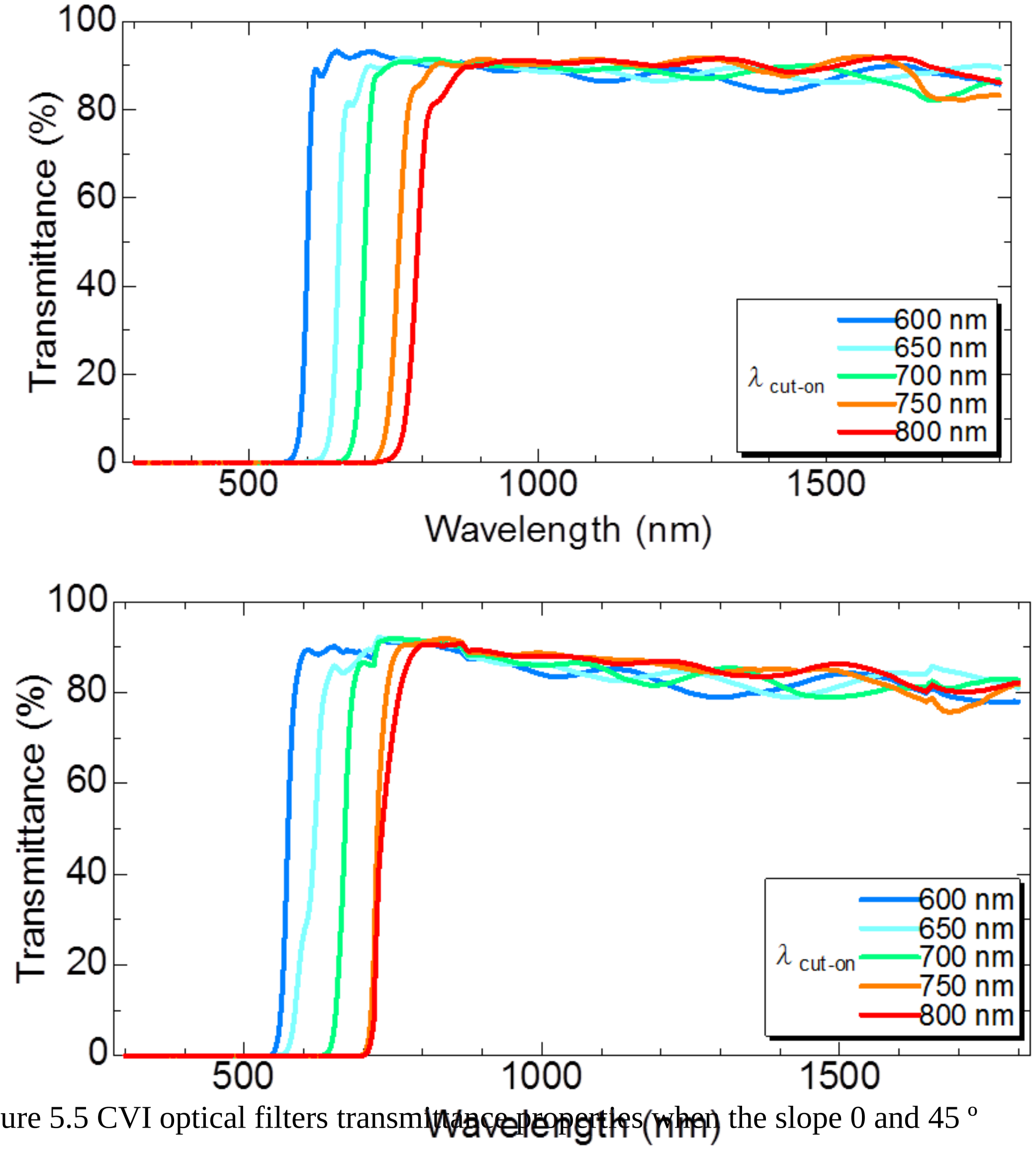

Figure 5.5 CVI optical filters transmittance properties when the slope 0 and 45 º

Figure 5.7 and 5.8 shows the measured photovoltaic parameters of splitting solar cells. From these figures, the tendency of each parameter was similar to the simulation results.

There were large drops in Jsc of a-Si:H cells with splitting filters because as can be seen in Figure 5.5 these filters had large absorption losses especially in the short wavelength regions. Thus, it is important to suppress the optical loss in filters for maximizing the absorbers performance. Table 5.5 shows the photovoltaic parameters at a maximum performance of which was achieved at the splitting wavelength of 614 nm. The high conversion efficiency of 16.8% (top = 6.26%, bottom = 12.38%) was achieved with splitting solar cells structure. Comparing this results with the stand-alone a-Si:H and CIGS cells performance, it was experimentally verified that the spectrum splitting four-terminal structure had feasible advantage.

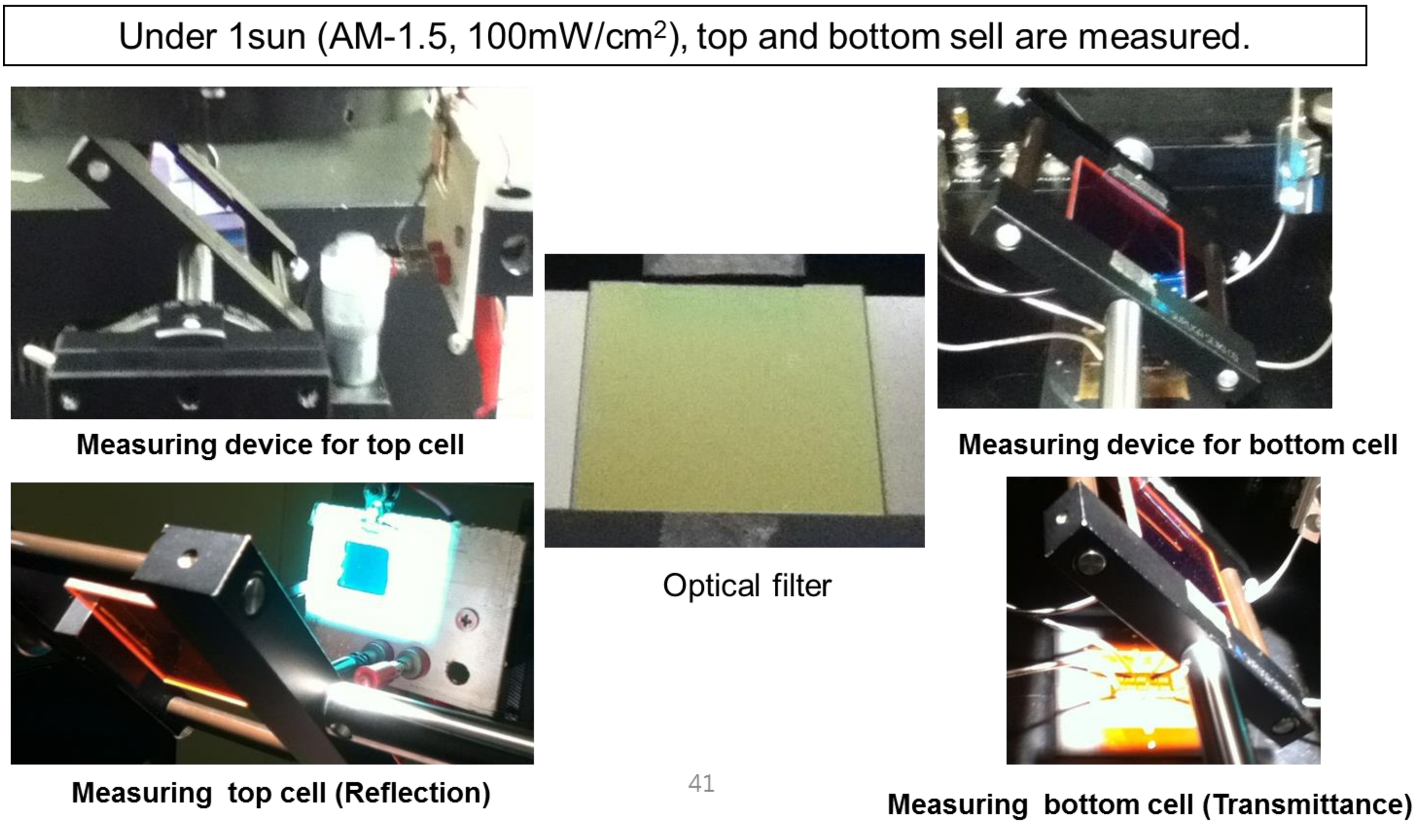

Under 1sun (AM-1.5, 100mW/cm^2), top and bottom sell are measured.

Measuring device for top cell

Optical filter

Measuring device for bottom cell

Measuring top cell (Reflection)

Measuring bottom cell (Transmittance)

Figure 5.6 Spectrum splitting measurement process image for top and bottom cell

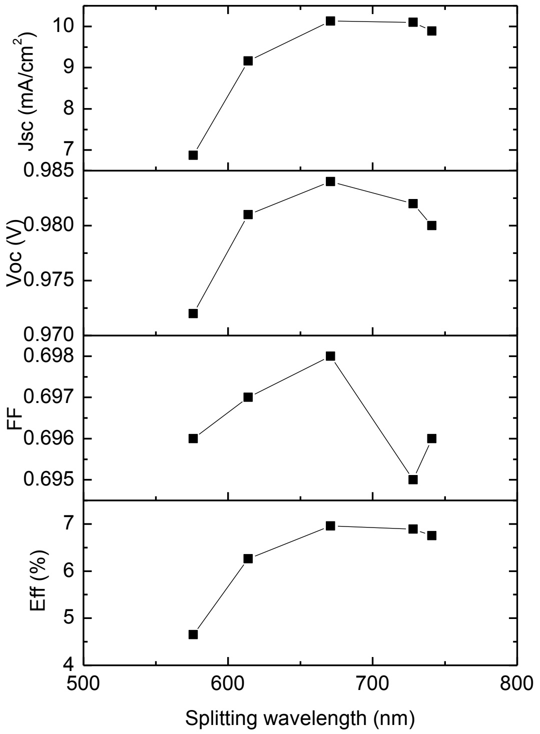

Figure 5.7 a-Si:H solar cell performance using 5 splitting wavelength CVI filters

Table 5.3 a-Si:H solar cell performance using 5 splitting wavelength CVI filters

Cell	**l_{SP} (nm)**	**J_{SC} (mA/cm^2)**	**V_{OC} (V)**	**FF**	**Eff (%)**
Top cell (a-Si:H)	576	6.872	0.972	0.696	4.65
	614	9.163	0.981	0.697	6.26
	671	10.13	0.984	0.698	6.96
	728	10.10	0.982	0.695	6.89
	741	9.889	0.980	0.696	6.75
	w/o (1sun)	13.56	0.990	0.702	9.41

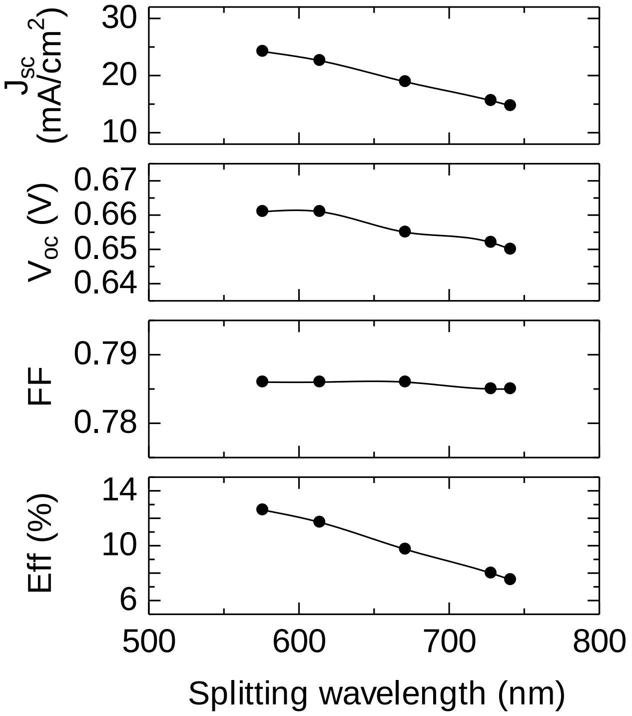

Figure 5.8 CIGS solar cell performance using 5 splitting wavelength CVI filters

Table 5.4 CIGS solar cell performance using 5 splitting wavelength CVI filters

Cell	**l_{SP} (nm)**	**J_{SC} (mA/cm^2)**	**V_{OC} (V)**	**FF**	**Eff (%)**
Bottom cell (CIGS)	614	23.49	0.676	0.780	12.38
	671	19.97	0.673	0.779	10.46
	728	16.44	0.666	0.780	8.54
	741	15.57	0.664	0.781	8.08
	w/o (1sun)	33.64	0.686	0.779	17.97

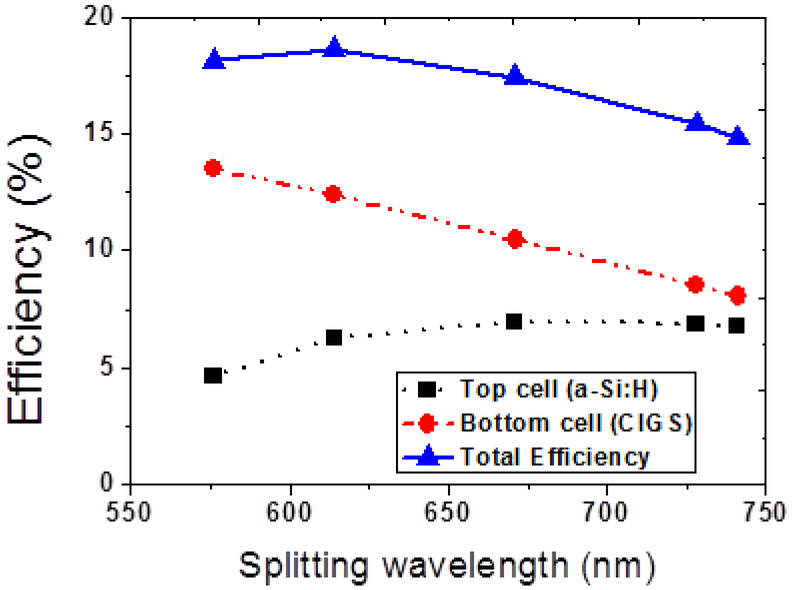

Figure 5.9 Comparison with solar cell efficiency for both of top and bottom cell under 5 different splitting wavelength

Table 5.4 The best solar cell performance by spectrum splitting method when splitting wavelength 614nm

Cell	J_{sc} (mA/cm^2)	V_{oc} (V)	FF	Eff (%)
a-Si:H	9.88	0.854	0.734	6.26
CIGS	22.6	0.661	0.786	12.38
Total	—	—	—	**18.64**

5-3-2 optimized splitter filter

However, as mentioned before, these set of splitting filters have some optical losses. The absorption, which is described as *1-R-T*, of the filter is not zero not only in the short-wavelength region but in long-wavelength region. So as the effect of optical characteristics of splitting filter can be suppressed as much as possible, the splitting filter whose *I*sp was 620 nm was newly developed in collaboration with Kaneka Corporation. Figure 5.10 shows optical filter and 5, 11 shows the spectral characteristics of the splitting filter at an angle of 45 degree. This filter has much less absorption losses than those ones.

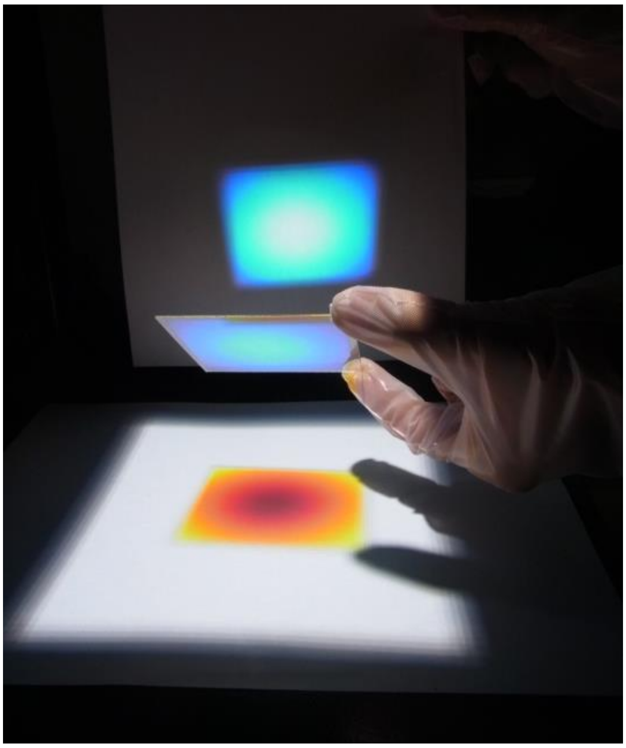

Figure 5.10 Optimized optical filters image

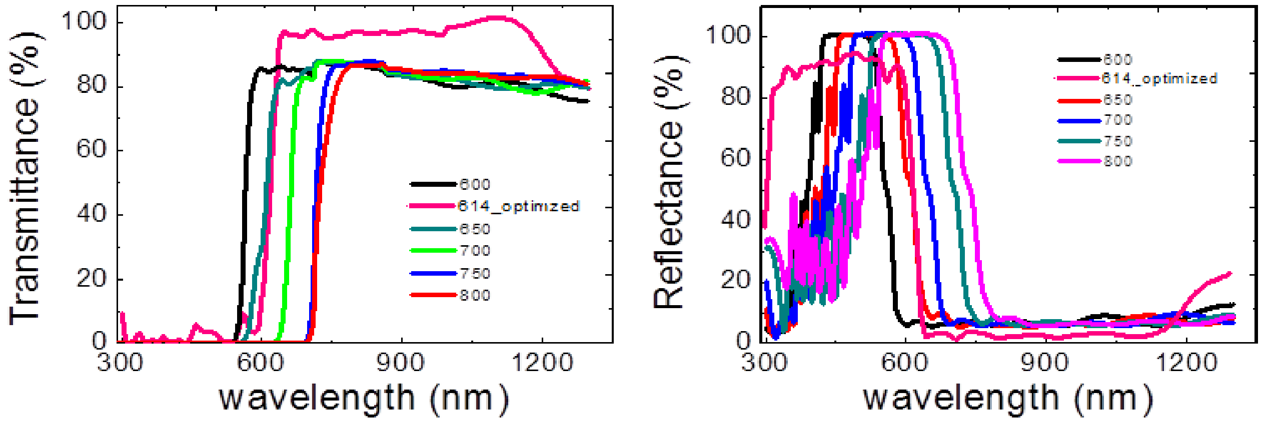

Figure 5.11 Optimized optical filters transmittance and reflectance compare with CVI filters when the slope 45 °

The structure of CIGS bottom cells consisted of Al grid/ ZnO:B/ ZnO/ CdS/ CIGS/ Mo/ soda-lime glass in figure 5.12. CIGS absorber layer was fabricated by a three-stage method using a molecular beam epitaxy (MBE) apparatus, which was equipped with elemental Cu, In, Ga, and Se Knudsen cells. The growth temperature at the first stage was about 300 ℃, and those at the second and third stages were about 530 ℃. The CdS buffer layer was deposited by a chemical bath deposition process and the non-depoed ZnO/ZnO:B window layers were prepared by MOCVD method. In this study, CIGS solar cell performance was evaluated by active area.

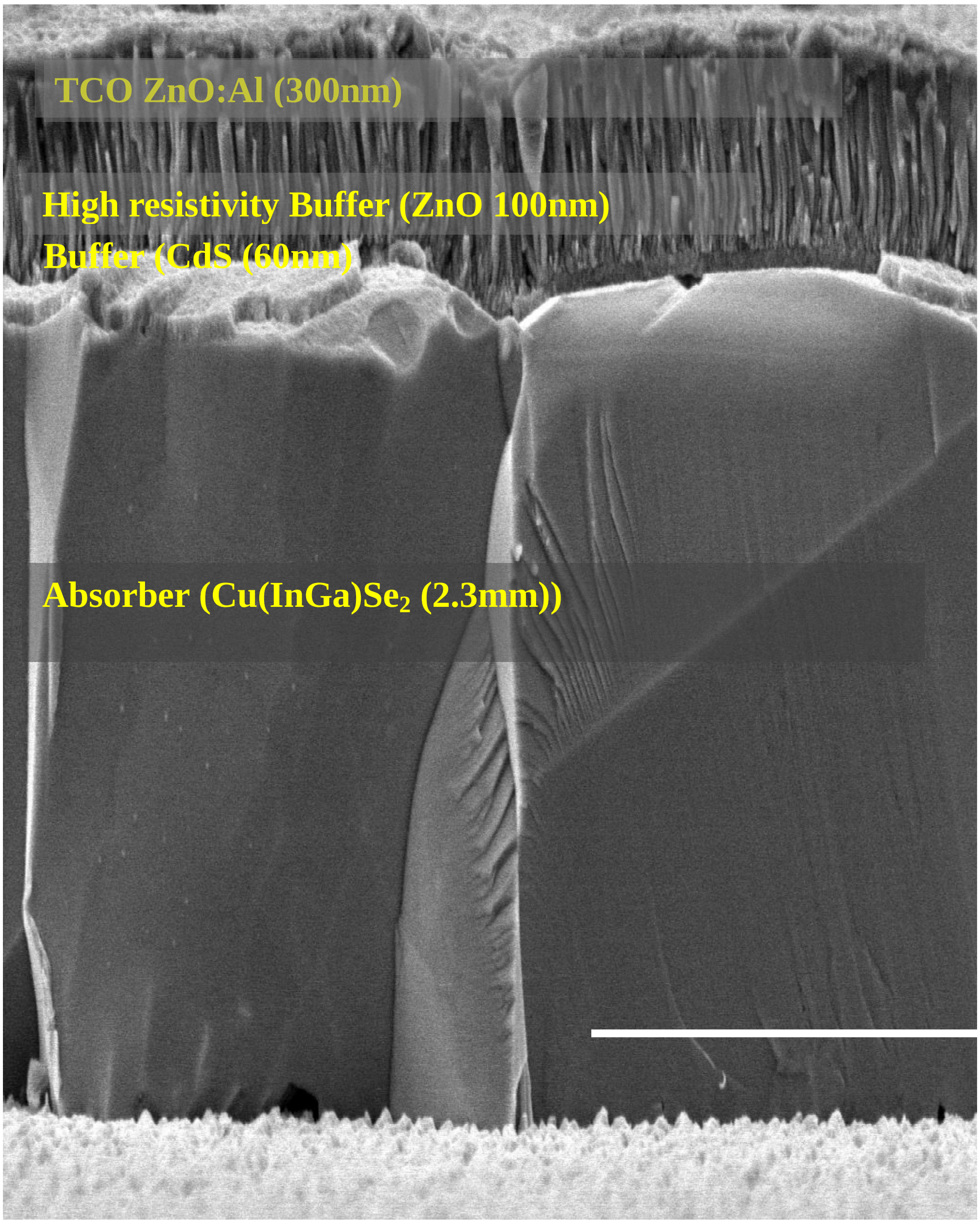

Figure 5.12 Cross-section image of CIGS (bottom cell) image and CIGS solar cell structure

Then, we measured splitting solar cells with these filter and CIGS cells. Finally, we could successfully achieve very high efficiency of over 20%, whose detail parameters are in Table 5.5.

Table 5.5 The solar cell performance by spectrum splitting method using optimized optical filter when splitting wavelength 614nm

Cell	I_{SP} (nm)	V_{oc} (V)	J_{sc} (mA/cm^2)	FF (%)	Eff(%)
Top cell (a-Si:H)	614 nm	0.99	12.9	71.0	9.2
Bottom cell (CIGS)		0.63	28.5	72.5	13.1
Total	-	-	-	-	22.25
Total intrinsic efficiency after correction of light intensity					22.9

5-4 Summary

In this chapter, to achieve our final target of the thin-film full spectrum solar cells with low-concentration ratios, four-terminal solar cells structure was studied as one of the key technologies. As introduced in the beginning part of this chapter, four-terminal structure gives not only a high performance but also a lot of options for component cells material and device architecture. This study focused on two different types of four-terminal structure. One was the mechanically-stacked tandem structure, and the other was the spectrum splitting structure. Amorphous silicon and $Cu(In,Ga)Se_2$ were used as absorber of top and bottom cells, respectively. The photovoltaic performance was investigated by theoretical and experimental procedures in both cases. From theoretical analysis, it was found that the total conversion efficiency of both top and bottom cells exceeded the efficiency of each cell and could achieve 20% or more. Furthermore, it can reach for 25% with low-concentration technique. For the case of combination of a-Si:H with CIGS, they can complement the some poor part of the spectral response each other. It indicates that the four-terminal structure can utilize the advantages of each component cell efficiently. From experimental results, the mechanically-stacked double-junction a-Si:H//CIGS solar cell was successfully fabricated. Both of the solar cells achieved high conversion efficiency of 14.9% at 1 sun, even though it was lower than that of stand-alone bottom cell. Thus, if those problems on optical losses were solved, the total efficiency can be improved more. For the case of spectrum splitting solar cells, the splitting wavelength was varied and the total efficiency of 18.64 % was achieved at 614 nm. The performance was higher than the stand-alone a-Si:H and CIGS cells performance, therefore it was experimentally verified that the spectrum splitting four-terminal structure had feasible advantage to high efficiency thin-film solar cells. By reducing the absorption loss of the splitting filter, the efficiency was successfully improved up to 22.9% at 1 sun. It is desired that the performance could be further improved in combination with low-concentration technique.

REFERENCES

[1] M. A. Green, K. Emery, Y. Hishikawa, W. Warta and E. D. Dunlop: *Prog. Photovoltaics Res. Appl.* **20** (2012) 606.

[2] M. Wiemer, V. Sabnis, H. Yuen: *Proc. SPIE* **8108** (2011) 810804-1.

[3] D. J. Friedman: *Curr. Opin. Solid State Mater. Sci.* **14** (2010) 131.

[4] R. R. King, D. C. Law, K. M. Edmondson, C. M. Fetzer, G. S. Kinsey, H. Yoon, D. D. Krut, J. H. Ermer, R. A. Sherif, and N. H. Karam: *Adv. OptoElectronics* 2007 (2007) No. 29523, 1.

[5] R. R. King, R. A. Sherif, G. S. Kinsey, S. Kurtz1, C. M. Fetzer, K. M. Edmondson, D. C. Law, H. L. Cotal, D. D. Krut, J. H. Ermer, and N. H. Karam: Proc. Int. Conf. on Solar Concentrators for the Generation of Electricity or Hydrogen, 2005.

[6] M. Yamaguchi, T. Takamoto, A. Khan, M. Imaizumi, S. Matsuda and N. J. Ekins-Daukes: *Prog. Photovoltaics Res. Appl.* **13** (2005) 125.

[7] M. W. Wanlass, T. I. Coutts, 1. S. Ward, K. A. Emery, T. A. Gessert, and C. R. Osterwald: Proc. 21st IEEE Photovoltaic Specialists Conf., 1990, p. 38.

[8] J. C. C. FAN and B. J. Palm: *Solar Cells* **10** (1983) 81.

[9] A. Madan: U.S. Patent 0150542 A1 (2005).

[10] T. Nagashima, K. Okumura, K. Murata and Y. Kimura: Proc. 28th IEEE Photovoltaic Specialists Conf., 2000, p. 1193.

[11] L. Wang, Y. Wang, A. Gerger, A. Lochtefeld, K. Shreve, A. Barnett: Proc. 37th IEEE Photovoltaic Specialists Conf., 2011, p. 000286.

[12] Y. Matsumoto, K. Miyagi, H. Takakura, H. Okamoto, and Y. Hamakawa: Proc. 21st IEEE Photovoltaic Specialists Conf., 1990, p. 1420.

[13] H. Takakura: *Jpn. J. Appl. Phys.* **31** (1992) 2394.

[14] W. Ma, T. Horinouchi, C. C. Lim, H. Okamoto, Y. Hamakawa: *Sol. Energy Mater. Sol. Cells* **32** (1994) 351.

[15] Y. Matsumoto, G. Hirata, H. Takakura, H. Okamoto, and Y. Hamakawa: *J. Appl. Phys.* **67** (1990) 6538.

[16] D. L. Morel: *Solar Cells* **24** (1988) 157.

Chapter 6

General Conclusion and future prospects

6.1 General Conclusion

This thesis describes the results of research on the numerical analysis and elemental technology for full spectrum splitting thin-film solar cell to improve conversion efficiency. The first theoretical analyses of amorphous silicon solar cell are studied. The model of the solar cell structure assumes a p-i-n superstrate structure. For electrical and optical parameters were taken from experimental results and refered literature. Each layer using spectroscopic ellipsometry (SE) analysis results by using Tauc-Lorentz model. In order to investigate that how the devices structure influences the solar cell performance of a-Si:H solar cells under various parameter such as band gap, thickness. Then best performance solar cell parameter has been calculated and based on these parameter, spectrum splitting structure simulation has been studied. a-Si:H and CIGS cells are having thousands of variable parameters in the splitting structure. Among them, main parameters are considered to be the splitting wavelength, which is the exact number of wavelength that divided the solar spectrum into two parts or more, and band gap and thickness of absorber materials. the total efficiency under the different range of splitting wavelength. The total efficiency for the combination of the top cell with wider band gap and the bottom cell with narrow band gap shows higher total efficiency. In this simulation, when splitting wavelength is 600nm, we can obtain the best total simulated splitting efficiency of 24.1% (Eg = 2.0 eV, Jsc = 11.7 mA/cm2, Voc = 1200 mV, FF = 70 %, Eff. = 10.7 % for the top cell and Eg = 1.1 eV, Jsc = 27.9 mA/cm2, Voc = 607 mV, FF = 79 %, Eff. = 13.4 % for the bottom cell). It was found from the simulation that the total efficiency of nearly 25% can be obtained at the splitting wavelength of 600 nm with top cell using higher band gap material. The experiment has been carried out to verify the simulation results. The a-Si:H solar cells with i-layers having its band gap of 1.9 eV have been fabricated by 60 MHz VHF-PECVD with solar cell area of 0.086 cm2 . The cell structure basically is glass /TCO(ZnO:B, SnO_2:F) / p-a-SiC:H / buffer / i-a-Si:H (1.9 eV, 300 nm) / n-μc-SiO:H / Ag / Al. In order to get wider band gap for a-Si:H solar cell, low temperature and high H_2 dilution (ratio of $SiH_4/H_2=8$) have been employed while substrate temperature , inter-electrode distance, VHF power density and chamber pressure were kept constant at 150℃, 2 cm, 1 mW/cm2 and 50 Pa, respectively. Then this solar cell has been measured by spectrum splitting technique. As a result, the total efficiency of 22.9% has been developed as been guided by the simulation.

6.2 Future prospects

In this study the thin film solar cells were developed by utilizing the various kinds of techniques of spectrum splitting technique and four terminal structures. For the case of four-terminal devices both stacked solar cell and spectrum splitting solar cells are in early phase of development, therefore it seems that there is much room for the improvement of the performance. So low-concentration technique could be enhanced the solar cells performance over 25%. Also the combination of these various novel technique such as double optical splitter for middle gap cell, with a further improvement also can be applied to the 5 to 6- junction thin film full spectrum solar cells with low concentration ratios which was introduced in the introduction of this thesis, to achieve a conversion efficiency of more than 40% expected.

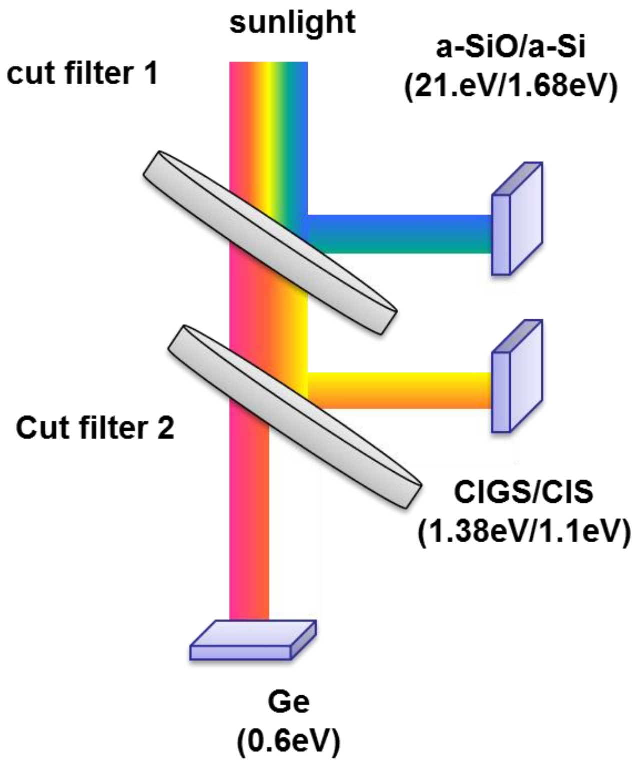

Figure 6.1 double splitter configuration for spectrum splitting technique

Table 6.1 simulation results of double optical splitter technique for top, middle and bottom cell

l_{sp} (nm)	**Wavelength range(nm)**	**Material**	**V_{oc} (V)**	**J_{sc} (mA/cm^2)**	**FF**	**Efficiency (%)**
645	300-640	InGaP	1.42	13.0	0.835	15.4
	650-870	GaAs	1.01	14.0	0.783	11.0
875						
	880-2000	CIGS	0.641	8.90	0.735	4.19
Total				35.90		**30.7**

List of publications

Journal Papers

1. **Sinae Kim**, Shunsuke Kasashima, Porponth Sichanugrist, Taizo Kobayashi, Tokio Nakada and Makoto Konagai

〞Development of Thin-Film Solar Cells Using Solar Spectrum Splitting Technique”

Solar Energy Materials and Solar Cells (2013)214–218

2. **Sinae Kim**, Porponth Sichanugrist and Makoto Konagai

〞Amorphous Solar Cell on Multilayer of SnO_2/ZnO TCO Substrate for Full Spectrum Splitting Solar Cell Application”

Canadian Journal of Physics, Published on the web 3 June 2014, 10.1139/cjp-2013-06203.

3.**Sinae Kim**, Masanobu Isshiki, Porponth Sichanugrist, Takuji Oyama , Hidefumi Odaka 2and Makoto Konagai

〞Application of Amorphous Thin-film Silicon solar cell Using High Transmitted SnO2:F Substrate for Full Spectrum Splitting Technique” (Submit Expected)

International Conferences

1. Sinae Kim*, Junnichi Hanna,

〞Fabrication of Si thin films using rf-PECVD with SiH4 and F2”

24th International Conference on Amorphous and Nanocrystalline Semiconductors, Nara, Japan, August 21-26, 2011 (oral presentation)

2. Wei.Zhang*, Sinae Kim, Junnichi Hanna,

"Layered Structure in As-Deposited SiGe Thin films by rf-PECVD with SiH4 and GeF4 and Their Enhanced Solid-State Scrystallization at Low-Temperatures"

24th International Conference on Amorphous and Nanocrystalline Semiconductors, Nara, Japan, August 21-26, 2011 (oral presentation)

3. Sinae Kim* , Shunsuke Kasashima , Porponth Sichanugrist , Makoto Konagai

"Development of Thin-Film Solar Cells Using Solar Spectrum Splitting Technique"

38th IEEE Photovoltaic Specialists Conference, Austin, USA, June 3-8, 2012 (poster presentation)

4. Sinae Kim, Shunsuke Kasashima , Porponth Sichanugrist , Taizo Kobayashi , Tokio Nakada , Makoto Konagai

"Study of Thin-film Solar cells Using Solar Spectrum Splitting Technique"

27th European Photovoltaic Solar Energy Conference, Frankfurt, Germany, Sep 24-28.2012 (poster presentation)

5. Sinae Kim, Shunsuke Kasashima , Porponth Sichanugrist , Taizo Kobayashi , Tokio Nakada , Makoto Konagai

"Study of Thin-Film Solar Cells with Solar Spectrum Splitting Technique"

22nd Photovoltaic Solar Energy Conference, Hangzou, China, Nov 4-7, 2012 (invited presentation)

6. Shunsuke Kasashima, Yuki Moriya, Banch Janthong, Sinae Kim, Porponth

Sichanugrist , Makoto Konagai

"Development of High Efficient Si Thin Film Solar Module Based on Triple Junction Cell Technology”

22nd Photovoltaic Solar Energy Conference, Hangzou, China, Nov 4-7, 2012 (Oral presentation)

7. Sinae Kim, Shunsuke Kasashima , Porponth Sichanugrist , Taizo Kobayashi , Tokio Nakada , Makoto Konagai

"Study of Thin-Film Solar Cells with Solar Spectrum Splitting Technique”

4th Global Photovoltaic Conference, Busan, Korea,Nov 19-21, 2012 (poster presentation)

8. Sinae Kim, Shunsuke Kasashima, Porponth Sichanugrist , Makoto Konagai

"Application of SnO2 Substrate to Top Cell for Spectrum Splitting Type Solar Cell”

39th IEEE Photovoltaic Specialists Conference, Tampa, USA, June 16-21, 2013 (porter presentation)

9. Makoto Konagai, Sinae Kim, Yuki Takiguchi, Porponth Sichanugrist, Taizo Kobayashi, Tokio Nakada

"Development of High-performance Solar Cells Using Spectrum Splitting Technique”

39th IEEE Photovoltaic Specialists Conference, Tampa, USA, June 16-21, 2013 (invited presentation)

10 Sinae Kim , Porponth Sichanugrist , Makoto Konagai

"High Performance Solar Cell Fabricated on Flattened SnO_2/ZnO Substrate for Full Spectrum Splitting Solar Cell Application"

25th International Conference on Amorphous and Nano-crystalline Semiconductors (ICANS), Toronto, Canada , Aug. 18-23 2013 (oral presentation)

11. Dongwon Kang, Sinae Kim , Porponth Sichanugrist , Makoto Konagai

"A-Si:H n-i-p Solar Cells Fabricated at 100 ℃for High Voc Top Cell of Spectrum Splitting Solar Cells "

25th International Conference on Amorphous and Nano-crystalline Semiconductors (ICANS), Toronto, Canada , Aug. 18-23 2013 (poster presentation)

International Forums, Workshops

1. Sinae Kim, S. Kasashima , P. Sichanugrist , T Kobayashi , T. Nakada , M. Konagai, "Development of Thin-Film Solar Cells Using Solar Spectrum Splitting Technique" Korea-Japan Top University League Workshop on Photovoltaic 2012, Korea Univiersity, Seoul, Korea, August 1-4, 2012

2. Sinae Kim, S. Kasashima , P. Sichanugrist , T Kobayashi , T. Nakada , M. Konagai, "Study of Thin-Film Solar Cells Using Solar Spectrum Splitting Technique" 6th International Forum on Multidisciplinary Education and Research for Energy Science, Hawaii, USA, December 14-18, 2012

Domestic Conferences, Symposiums, Forums, Workshops

1. 橋 史哲，笠嶋 俊介，金 信愛，平井 義晃, Porponth Sichanugrist, 山田 明, 小長井 誠 第59回 応用物理学関係連合講演会,2012